

博士論文

Cooling Efficiency of Thermal Power Plant and Thermal Pollution on
Global Rivers in Warmer Climates
(地球温暖化が火力発電所の冷却効率と全球河川の熱汚染に及
ぼす影響)

オタ ケダル
(Otta Kedar)

Acknowledgments

I am grateful to the almighty lord and my parents for giving me a life that to do something worthy. I'm thankful to JICA (especially Ando San and Chikako San) and the University of Tokyo to fund and host my study in Japan. I want to thank my supervisor Prof. Dr. Taikan Oki, co-supervisor Assoc. Prof. Dr. Hyungjun Kim and my mentor Asst. Prof. Dr. Daisuke Tokuda for their constant guidance and support, without which it would not have been possible to achieve this feat. I'm also thankful to my Ph.D. committee members Prof. Dr. Hironori Kato, Assoc. Prof. Dr. Takeyoshi Chibana, and Dr. Naota Hanasaki, for their valuable inputs to significantly improve my research.

I'm grateful to all the faculty members in my lab, Assoc. Prof. Yamazaki, Prof. Yoshimura, Prof., Asst. Prof. Kenshi Hibino, Asst. Prof. Dr. Xudong Zhou, and Prof. Dr. Kazo Oki for their guidance throughout the journey. I'm also grateful to my friends Dr. Sobhan Afraz and Dr. Mustajab Ali, who helped me throughout my Ph.D. program. I'd also like to thank Isabel, Tanaka San, Kamiya San, Ikeuchi San, Shoizawa San, Tozawa San, and Fujimori San for helping me settle down and start my research. I'd also like to thank my lab mates Prakat, Debanjali, Yizhou, and every other lab member for their support. I'm also thankful to the secretaries in my lab, Tsukda San, Yokoyama San, Saito San, and Takeuchi San, for their assistance in smoothening my Ph.D. journey. I'm also grateful to FSO members, especially Tonegawa San and Abeki San, who helped in smooth onboarding, and Aoyama San, who helped me process the requirements for completing my Ph.D. in the Civil Engineering department.

I want to thank Assoc. Prof. Dr. Basudev Biswal, my master thesis supervisor, for inspiring me to pursue research as a career. I'd also like to extend my gratitude to Assoc. Prof. Dr. Riddhi Singh for supporting me in pursuing my Ph.D. I'd also like to thank all my teachers at the University of Tokyo, IIT Hyderabad, CET Bhubaneswar, and DPS Damanjodi, whose efforts built the pedestal of success I stand on.

I'm thankful to my friends from U-Tokyo (Dr. Shivani, Isha, VCK, Dr. Debasmita, Robuil, Lilangi, Bhanu, and Varshini), my friends from IIT Hyderabad (Krutika, Yogeshwari, Aniket, Ankur, Husen, Ishan, Arvind, Pritanjali, Tarun, Smita, Dr. Anita, Durga, and Laxmipriya), my CET Bhubaneswar friends (Ashish, Ashish, Nirmal, Rajesh, Asmita, Vamshi, Avinash, Manisha, Lipi, and Baisakhi), and my classmates from DPS Damanjodi (Judhistira, Dr. Ranjita, Sancy, Rakesh, Prajoth, and Priya) among many others. They motivated me and stood by me during rough patches of life. Finally, I'd like to thank my lovely little sister, Ankita Otta, for giving me a reason to laugh every day and cheer me up throughout my journey.

I dedicate my Ph.D. to my late grandmother, who loved me and encouraged me consistently to study hard, my hero, my father, who inspire me to aim higher and work for it, and my mother who's love and affection keeps me going through the struggles.

Table of Content

Acknowledgments.....	3
List of Figures	9
List of Tables	14
Abstract.....	16
Chapter 1: Introduction	21
1.1 Climate Change in a nutshell.....	21
1.2 Impacts of Climate Change on Terrestrial Water Cycle	21
1.3 Impacts of Climate Change on Water Temperature	21
1.4 Impacts of Climate Change on Thermal Power plants.....	22
1.5 Impacts of Climate Change on Thermal Effluents.....	22
1.6 Climate models and experiments in CMIP6.....	22
1.7 Rationale, Significance, and Novelty of the Research Work/ Philosophy Behind the Doctorate and Novelty of the Research Work.....	25
1.8 Thesis Outline.....	27
Chapter 2: Changes in the Terrestrial Water Cycle: climate change impacts on water availability	30
2.1 Introduction	30
2.1.1 The Terrestrial Water Cycle and its budget	30
2.1.2 Hydrological cycle under Climate Change.....	31
2.2 Gaps in Previous Research and Scope of this Study	32
2.3 Data and Methodology	33
2.3.1 Hydroclimatic Data.....	33
2.3.2 Computation of Discharge	33
2.3.3 Event-wise analysis	34
2.3.4 Calculation of Asymmetry.....	35
2.3.5 Producing new ensembles from existing model ensembles.....	36
2.3.6 Symmetric Attribution of Risk.....	36

2.3.7	Considering multi-model mean	38
2.4	Results.....	38
2.4.1	Validation	38
2.4.2	Global changes in discharge.....	40
2.4.3	Global changes in hydroclimatic background	41
2.4.4	Changes in Discharge Attributes: Magnitude and Duration	45
2.4.5	Special case for Nile and Niger.....	48
2.4.6	Asymmetry in dry-wet shifts	48
2.4.7	Heterogeneity in magnitude-duration shifts	51
2.4.8	Explanation of the mechanism of changes in discharge.....	53
2.4.9	Symmetric Attribution of Extreme Event Risk to human-induced warming	55
2.5	Discussion.....	56
2.6	Conclusions	58

Chapter 3: Changes in River Water Temperature

60

3.1	Introduction	60
3.1.1	Importance of water temperature.....	60
3.1.2	Factors influencing water temperature.	60
3.1.3	Water temperature model: HEAT-LINK	61
3.1.4	Gaps in Previous research and scope of the study	61
3.1.5	Research Questions.....	62
3.2	Data.....	62
3.3	Methods.....	63
3.3.1	Adjustment of spatial and temporal resolution.....	63
3.3.2	Water temperature simulation and validation	63
3.3.3	Seasonal changes in temperature change	63
3.3.4	Sensitivity of temperature change.....	63
3.3.5	Attribution of extreme temperature to human-induced warming	64
3.3.6	Change in warm days, dry days, and the confluence of warm and dry days.....	64
3.4	Results.....	64
3.4.1	Validation	64
3.4.2	Water temperature rise in natural and anthropogenic scenarios.....	67
3.4.3	Seasonal changes in temperature rise due to Climate Change	73
3.4.4	Trends in water, air, and soil temperature	79

3.4.5	Climate sensitivity	80
3.4.6	Attribution of temperature rise to Climate Change.	82
3.4.7	Change in adverse conditions	84
3.5	Discussions	85
3.6	Conclusions	85
3.7	Future scope	86

Chapter 4: Impact of climate change on Thermal Power Production and Anthropogenic Heat Emission 88

4.1	Background and Introduction	88
4.1.1	Water Availability.....	88
4.1.2	Electricity generation and demand.....	88
4.1.3	Classification of Power Plants by Fuel Type	89
4.1.4	Thermal Power plants: Working Principle and Water Demand.....	90
4.1.5	Water-Energy Nexus	91
4.1.6	Impact of Climate Change on Thermal Power Plants and water-energy nexus	92
4.1.7	Ecological Integrity of water bodies.....	92
4.1.8	Role of Power plants in Thermal Pollution and Influence of climate change	93
4.1.9	Water Temperature rise due to Thermal Power plants.....	93
4.1.10	Previous Studies and Research Gaps	93
4.2	Data	95
4.2.1	Hydro-meteorological Data.....	95
4.2.2	Power plant Data	95
4.3	Methods	95
4.3.1	Power plant matching.....	95
4.3.2	Model Development for power plant water withdrawal, power production, and return flow	97
4.4	Power plant capacity and sensitivity analysis for cooling parameters	99
4.5	Results and Discussions	100
4.5.1	Validations.....	100
4.5.2	Changes in power production.....	102
4.5.3	Power plants under adverse conditions	105
4.5.4	Attribution of reduction in cooling efficiency to HIW.....	107
4.5.5	Thermal emissions and thermal pollution caused by power plants	107

4.6	Discussions	111
4.7	Conclusions	112
4.8	Future Scope	112

Chapter 5: Conclusion and Future Works 114

5.1	Synthesis of results and derived conclusions.....	114
5.2	Policy Implications for sustained power production	115
5.2.1	DACT to boost climate resilience and decline the thermal emissions.....	115
5.2.2	Combining solar photovoltaic power plants with thermal power plants	115
5.2.3	Decentralization of new thermal power plants	115
5.3	Future scope of the research	116
5.4	Final Note	116

Appendix 118

Thermal discharge and its decomposition	120
Flow from Land to Ocean.....	122

References 125

List of Figures

Figure 1.1: Possible Shared Socio-economic Pathways, <i>adapted from O'Neill et al., 2017</i>	24
Figure 1.2: Combined SSP-RCP scenarios at the end of the century adapted from Meinshausen et al., 2019	25
Figure 1.3: Sustainable Development Goals Involved in this work (colored)	27
Figure 2.1: The global hydrological cycle [adapted from Oki and Kim, 2016 ⁷⁹].....	31
Figure 2.2: Magnitude and Duration for a discharge time-series, by dividing it into a dry and wet phase using the long-term historical mean discharge. Similar dry and wet phases of discharge are demonstrated for three more rivers in figure A1.	34
Figure 2.3: Calculation of asymmetry. The cartesian plan has dry shift as abscissa and wet shift as ordinate.....	35
Figure 2.4: Trend, mean, and variability for a time-series.....	36
Figure 2.5: FAR for Amazon (at the outlet, fig 2.10), with threshold= ensemble mean + ensemble standard deviation of 99th percentile of magnitude.....	37
Figure 2.6: FAR for the Nile, with threshold= ensemble mean + ensemble standard deviation of 99th percentile of magnitude	37
Figure 2.7: Validation of model simulation. Panels a to k show the correlation coefficient of observed daily discharge and daily discharge from 11 CMIP6 models, across 227 GRDC gauge stations, for all available data from 1961 to 1990. Most models perform reasonably well, except for BCC-CSM2-MR. The summary of performance for each model is represented in a box plot in the last panel. The box plot shows the median (orange line) along with the lower quartile (25 th percentile) and the upper quartile (75 th percentile) of Correlation values for the available gauge stations. The whiskers show the range of the correlation coefficient values, excluding the outliers.....	39
Figure 2.8: Global changes in mean, median, and extreme river discharge. The figure illustrates the historical values of discharge (a, b, and c) and the changes in discharge (d-i), for two future scenarios (SSP126 and SSP585), in excess to historical values of discharge, in its lower extreme (left column), median value (central column) and upper extreme (right column). The difference in the two future scenarios is also shown in panels j, k, and l.	40
Figure 2.9: The figure depicts the hydroclimatic changes that trigger the changes in discharge. The 1st column represents Precipitation (P), the 2nd represents Evapotranspiration (ET), and the 3rd represents Runoff (R). The first row (a-c) shows the historical values of the hydroclimatic variables, while the 2nd and 3rd row (e-l) shows the future changes (for ssp126 and ssp585, respectively) of values in comparison to historical values.	41
Figure 2.10: The thirty river basins considered in the study are shaded, and their outlets are represented by black circles.	42
Figure 2.11: Basin-wise changes in discharge and their hydroclimatic background. The left panel shows the corresponding percentage changes with respect to historical values of the mean (black), median (green), lower extreme (red), and higher extreme (blue) freshwater discharge (at the outlet). The right panel shows multi-model mean changes of spatially averaged values of P (cyan), ET (orange), and R (black) (in comparison to their respective historical values) for the 30 major river basins in the high latitude (grey, only northern hemisphere), mid-latitude (green in the northern hemisphere and black in the southern hemisphere) and low latitude (Crimson for north of equator and orange for the south) regions. The small circles represent the changes for SSP126, while the large circles represent a more hostile SSP585 counterfactual future world. The lines join the changes for SSP126 and SSP585 counterfactual worlds. For the basins marked with a "*" for the discharge changes (left), the coefficient of variation for the mean discharge among the different CMIP6 models	

is greater than 50%, suggesting large variability among models, thus indicating low certainty in the results.....	43
Figure 2.12: The wet (a-h) and dry phase(i-p) values of 50 th percentile of Magnitude (Mag) and Duration (Dur) for historical values (1st column) and changes in their values in the future in comparison to corresponding historical values (2nd and 3rd column) and the difference between the two future scenarios (4th column). The dots show the significance of the change in terms of the model agreement.....	45
Figure 2.13: Same as S6 but for 99 th percentile values The dry phase Magnitude (Mag) and Duration (Dur) for historical values (1st column) and changes in their values in the future in comparison to corresponding historical values (2nd and 3rd column)) is shown in the above figure.....	46
Figure 2.14: The discharge time series for a 30year reference period for the Nile (top) and Niger (bottom)	48
Figure 2.15: Asymmetry in wet-dry shifts. The figure enunciates the asymmetric nature of shifts in magnitude (a) and duration (b) for the wet phase against the dry phase, for moderate (50th percentile) and extreme events (99th percentile), in SSP126 and SSP585 future scenarios. Asymmetry is calculated as the normalized angle formed at the origin between the 1:1 line and the line joining the origin and a point on a plot with wet shift on the x-axis and dry shift on the y-axis. The scatter plots show the ratio of SSP126 (top) and SSP585 (bottom) scenarios to the historical period for moderate (green) and extreme events (red) with dry phase in abscissa and wet phase in ordinate, for magnitude (a) and duration (b). The basin information of these scatter plots is provided in Fig. 2.16.....	49
Figure 2.16: Basin-wise dry phase changes against wet. The figure depicts the dry phase changes against wet phase for moderate(green) and extreme(red) values of magnitude (a and c) and duration (b and d) in SSP126(a and b) and SSP585(c and d) as a ratio to historical values. The grey (yellow) background shows symmetry (asymmetry) of changes, the black(orange) solid line is the 1:1 (-1:1) line, and darker shade means higher symmetry (asymmetry). The numbers in the circles represent basins: 1.Lena, 2.Yenisei, 3.Kolyma, 4.Mackenzie, 5.Ob, 6.Yukon, 7.Nelson, 8.Amur, 9.St.Lawrence, 10.Columbia, 11.Danube, 12.Volga, 13.Yellow, 14.Yangtze, 15.Mississippi, 16.Aravand, 17.Nile, 18.Indus, 19.Ganga-Brahmaputra, 20.Mekong, 21.Orinoco, 22.Niger, 23.Shebelle, 24.Amazon, 25.Tocantins, 26.Congo, 27.Zambezi, 28.Orange, 29.La Plata, 30.Murray-Darling. The color scheme for the basin number is the same as in Fig. 2.11	50
Figure 2.17: Magnitude-duration homogeneity. The figure illustrates the density plot of magnitude shifts against duration for global spatial distribution in dry phase (a) and wet phase (b), and basin-wise distribution for dry (c and e) and wet (d and f) phases in the two future scenarios (SSP126 with small solid circles and SSP585 with large hollow circles in panels c, e and d, f respectively) for P99 (c and d) and P50 (e and f). The numbers inside the circle represent the river basin: 1.Lena, 2.Yenisei, 3.Kolyma, 4.Mackenzie, 5.Ob, 6. Yukon, 7.Nelson, 8.Amur, 9.St.Lawrence, 10.Columbia, 11.Danube, 12.Volga, 13.Yellow, 14.Yangtze, 15.Mississippi, 16.Aravand, 17.Nile, 18.Indus, 19.Ganga-Brahmaputra, 20.Mekong, 21.Orinoco, 22.Niger, 23.Shebelle, 24.Amazon, 25.Tocantins, 26.Congo, 27.Zambezi, 28.Orange, 29.La Plata, 30.Murray-Darling. The color scheme for the basin number is the same as in Fig. 2.11.....	52
Figure 2.18: Symmetric attribution of both increase and decrease in risk to climate change for wet phase changes in historical (a, d, g), SSP126 (b, e, h), and SSP585 (c, f, i) for discharge attributes.....	55
Figure 2.19: Symmetric attribution of both increase and decrease in risk to climate changed for dry phase changes in historical (a, d, g), SSP126 (b, e, h), and SSP585 (c, f, i) for discharge attributes.....	55
Figure 3.1: Comparison of mean simulated water temperature with MIROC6-forced HEAT-LINK and GEMS observation.....	64
Figure 3.2: Global distribution of correlation for modeled water temperature against GEMS data. ...	65

Figure 3.3: Monthly water temperature for model simulation and GEMS observation for the period 1980-1999 for river gauge stations in Rhine River catchment.	65
Figure 3.4: Monthly water temperature for model simulation and GEMS observation for the period 1980-1999 for river gauge stations in different rivers in the world. The 12 months are represented on the x-axis and temperature on the y-axis.	66
Figure 3.5: Different IPCC SREX regions	67
Figure 3.6: Heterogeneity in the distribution of water temperature change with respect to the historical scenario. The vertical lines show the mean value for different SREX regions.	68
Figure 3.7: Heterogeneity in the distribution of air temperature change with respect to the historical scenario. The vertical lines show the mean value for different SREX regions.....	69
Figure 3.8: Heterogeneity in the distribution of soil temperature change with respect to the historical scenario. The vertical lines show the mean value for different SREX regions.....	69
Figure 3.9: Mean changes in water for different SREX regions, compared with shifts in air and soil temperature shifts. Shifts in values for hist-nat, SSP245-nat, SSP126, SSP245, SSP370, and SSP585 are calculated with respect to the historical scenario.	70
Figure 3.10: Spatial variability of temperature change. The figure illustrates the standard deviation of water temperature changes (top panel) and its comparison with air temperature (middle panel) and soil temperature (lower panel). Shifts in values for hist-nat, SSP245-nat, SSP126, SSP245, SSP370, and SSP585 are calculated with respect to the historical scenario.	71
Figure 3.11: Consistency of water temperature and air temperature under anthropogenic warming	72
Figure 3.12: Global change in water temperature for 30year average for natural-historical (e-h), SSP245-nat (i-l), SSP126 (m-p), SSP245 (q-t), SSP370 (u-x) and SSP585 (y-ab) against the historical scenario (a-d). 1961-1990 is considered as reference period for historical period while 2071-2100 is reference period for future scenarios.....	73
Figure 3.13: The spatial variability in the shift in water temperature at a seasonal scale differs for different SREX regions.	74
Figure 3.14: Global change in air temperature for 30year average for natural-historical (e-h), SSP245-nat (i-l), SSP126 (m-p), SSP245 (q-t), SSP370 (u-x) and SSP585 (y-ab) against the historical scenario (a-d). 1961-1990 is considered as reference period for historical period while 2071-2100 is reference period for future scenarios.	75
Figure 3.15: The spatial variability in the shift in air temperature at a seasonal scale differs for different SREX regions.	76
Figure 3.16: Global change in soil temperature for 30year average for natural-historical (e-h), SSP245-nat (i-l), SSP126 (m-p), SSP245 (q-t), SSP370 (u-x) and SSP585 (y-ab) against the historical scenario (a-d). 1961-1990 is considered as reference period for historical period while 2071-2100 is reference period for future scenarios.....	77
Figure 3.17: The spatial variability in the shift in water temperature at a seasonal scale differs for different SREX regions.	78
Figure 3.18: Trends in water, air, and soil temperature for the 30 years reference period for historical (1961-1990) and future periods (2071-2100). Natural-historical (a-c), SSP245-nat (d-f), historical (g-i), SSP126 (j-l), SSP245 (m-o), SSP370 (p-r) and SSP585 (s-u) scenarios.	79
Figure 3.19: Change in net radiative forcing at the top of the atmosphere with respect to the historical period.	80
Figure 3.20: Mean and standard deviation of temperature sensitivity to radiative forcing. The probability density plot for the same is available in the appendix.....	81
Figure 3.21: Symmetric FAR values for extreme water temperature, air temperature and soil temperature under Historical (a-c), SSP126 (d-f), SSP245 (g-i), SSP370 (j-l), and SSP585 (m-o) scenarios.	82

Figure 3.22: Symmetric FAR values for extreme water temperature, air temperature, and soil temperature under Historical, SSP126, SSP245, SSP370, and SSP585 scenarios for different SREX....	83
Figure 3.23: Change in dry, warm, and dry-warm days compared to the historical scenario.....	84
Figure 4.1: Gross electricity production for OECD countries, non-OECD countries, and the world total The Data source: IEA. World Energy Outlook 2019 ¹¹⁰	89
Figure 4.2: Gross electricity production at the global scale for different fuel types Data source: IEA. World Energy Outlook 2019 ¹¹⁰	89
Figure 4.3: Gross electricity production for different fuel types for OECD and Non-OECD countries in 2019 # Includes sources not specified elsewhere, e.g., pumped hydro, non-renewable waste, and statistical discrepancies (which can be positive or negative). Data source: IEA. World Energy Outlook 2019 ¹¹⁰	90
Figure 4.4: Climate change impact on thermal power plants and thermal emissions	92
Figure 4.5: Location of matched power plants with once-through (OT), combined (CB), and tower cooling (TC) systems	97
Figure 4.6: Schematic Representation of Power plant Model coupled with the existing HEAT-LINK and CaMa coupled model (inside the yellow box).....	97
Figure 4.7: Calculation Flow for Each Timestep. The Yellow box represents the existing HEAT-LINK coupled with CaMa-FLOOD.....	98
Figure 4.8: Progression of power plant label capacities (PP Capacity) for power plants with once-through (OT) and combined (CB) cooling systems	99
Figure 4.9: Estimation of cooling parameter “ α ” for once-through cooling systems. The two y-axes are normalized to their respective minimum and maximum values.....	100
Figure 4.10: Correlation of simulated water temperature with GEMS observation	100
Figure 4.11: Monthly values of observed water temperature (black) and two experiments, with power, plants water withdrawal (red) and return flow and without (blue) for various river catchments in the Rhine-Meuse River basin for available data during 1980-1999. For panel 9, there is no upstream power plant.	101
Figure 4.12: Thermal discharge in MW in the current (x-axis) and a previous study (y-axis).	101
Figure 4.13: Cooling efficiency and water sufficiency of Power plants.	102
Figure 4.14: Power production under climate change	104
Figure 4.15: Power plant cooling efficiency in different SREX regions.	105
Figure 4.16: Change in frequency of adverse conditions at power plant location.....	106
Figure 4.17: Cooling efficiency under adverse conditions	106
Figure 4.18: The attribution of reduction in cooling efficiency to HIW	107
Figure 4.19: Rise in water temperature due to power plant thermal emissions in the historical scenario.....	107
Figure 4.20: Thermal emission and temperature rise at power plant location.....	108
Figure 4.21: Rise in water temperature due to power plants compared to the historical scenario ..	109
Figure 4.22: Change in water temperature rise caused by power plants (Δ Temperature Rise) at each grid cell when compared against the historical scenario	110
Figure 4.23: Change in temperature rise due to power plants.....	110
Figure A 1: Wet(blue) and dry(red) phases of river discharge at the outlet, like in fig. 2.2, for Shebelle (small basin), Murray-Darling (Dry basin), and Lena (cold basin).....	118
Figure A 2: The spatial variability of sensitivity in the shift in water temperature for different SREX regions.....	119
Figure A 3: The spatial variability of sensitivity in the shift in air temperature for different SREX regions.....	119

Figure A 4: The spatial variability of sensitivity in the shift in soil temperature for different SREX regions.....	120
Figure A 5: Discharge (Q), Temperature (T), and Thermal Discharge (TD) for global freshwater flow in the historical scenario are shown in panel a-c. Panels d-f, g-l, j-l, and m-o show the shifts in values in SSP126, SSP245, SSP370, and SSP585 future worlds, respectively compared to historical values for discharge (d, g, j, m), water temperature (e, h, k, l) and thermal discharge (f, i, l, o).....	121
Figure A 6: Changes in thermal discharge are decomposed into three components: change due to change in discharge, change due to change in temperature, and covariance term. Panels a-c, d-f, g-l, and j-l show the decomposed values of change in thermal discharge for SSP126, SSP245, SSP370, and SSP585 future worlds, respectively, for discharge change (a, d, g, j), water temperature change (b, e, h, k) and the co-variance term (c, f, i, l).	122
Figure A 7: Flow from land to ocean. The sum of all discharge (a), average water temperature (c), and thermal discharge (e) for all five oceans in the world are shown in the form of a bar chart. The adjacent figures (b, d, and f) show the respective relative change of future scenarios with respect to the historical scenario.....	123

List of Tables

Table 1.1: The four RCPs (as given in Moss et al., 2010) *MESSAGE, Model for Energy Supply Strategy Alternatives and their General Environmental Impact, International Institute for Applied Systems Analysis, Austria; AIM, Asia-Pacific Integrated Model, National Institute for Environmental Studies, Japan; GCAM, Global Change Assessment Model, Pacific Northwest National Laboratory, USA (previously referred to as MiniCAM); IMAGE, Integrated Model to Assess the Global Environment, Netherlands Environmental Assessment Agency, The Netherlands.	24
Table 2.1: Details of ISIMIP2b Data.....	39
Table 2.2: Global values for moderate and extreme events	47
Table 3.1: Input Climatic and land-surface Data Configuration for historical, natural (Hist-nat and SSP245-nat), pi-control, and future (SSP126, SSP245, SSP370, SSP585) scenarios.	62
Table 4.2: Open-sourced data available for power plants. Raptis: Raptis et al., 2016; GEOPP: Global Energy Observatory Power plant; WRI: World Resource Institute; CARMA: Carbon Monitoring for Action.	95
Table 4.3: The electrical efficiency as given in Raptis et al., 2016.	96
Table 4.4: Number of power plants with once-through (OT) and combined (CB) cooling systems till 2014 and in future	99

Abstract

The thermal power plants demand vast volumes of water to cool the steam in their steam cycles. However, the water demand varies depending on the type of cooling system employed. Based on the amount of heat to be discharged by cooling water and the restrictions on thermal effluent discharge (to protect the aquatic and marine ecosystem), the water demand for power plants can be estimated. Inland power plants that use freshwater for cooling purposes, water sufficiency is critical for power production. The cooling efficiency of the power plants depends majorly on two factors: water availability and water temperature. Under climate change, the water temperature is expected to rise, and the water availability may increase or decrease. Therefore, the power plants would need more water to cool the same amount of steam as the scope for heat exchange between the hot steam and cooling water diminishes with increasing water temperature (due to restrictions on thermal emissions).

Would the freshwater available for the power plants be sufficient to meet the increasing demand for cooling water in the future? A few researchers have attempted to answer this question, but they have determined that the changes in cooling efficiency under limited future scenarios and the natural scenarios (without anthropogenic greenhouse gas emissions) have remained entirely unexplored. After addressing these gaps, this research advances a step forward to assess the contribution of human-induced warming responsible for changing future cooling efficiency. Additionally, the water temperature rise due to thermal pollution caused by the power plants on the global rivers was investigated.

A power plant model was developed, coupled with an existing thermodynamic model (HEAT-LINK) associated with a hydrodynamic model (CaMa-Flood) to achieve the above goals. General Circulation Model (GCM) data available under the World Climate Research Programmer's (WRCP's) 6th Phase of Coupled Model Intercomparison Project (CMIP6) were used in this study.

As the first step, the changes in surface water discharge were computed, which governs the water available for the power plants. Many researchers have discussed the future freshwater discharge owing to changing climate, determining the causes for its temporal and spatial changes in mean and extreme conditions. However, the analysis event-scaled studies on daily discharge have not been discussed. In this research, CaMa-Flood simulated discharge was divided into magnitude and duration changes in dry and wet phases for two future scenarios (SSP126 and SSP585), which are compared with their respective historical scenario (with full anthropogenic forcings) to unravel the complexities associated with shifts in discharge under climate change. Additionally, one natural-historical scenario

(Hist-nat) for available models was utilized to determine the risk of extreme changes in magnitude and duration attributed to human-induced warming (HIW). A new index, SymFAR, was defined to determine both the decrease and increase in risk attributed to HIW symmetrically. A substantial asymmetrical shift was found for the magnitude and duration of discharge anomalies under climate change, particularly extreme events. Further, the shifts are primarily larger for the dry phase for the duration of events, whereas extensive wet phase shifts are observed for the magnitude. Moreover, the discharge shifts are associated with relatively homogenous magnitude-duration shifts for the dry phase than the wet phase, particularly for extreme events. This research uncovers a rather voluminous wet-phase shift than dry-phase shifts but lengthier dry-phase shifts than wet-phase shifts, which tend to intensify with additional warming for most regions of the world. Thus, the power plants would face longer dry periods, leading to declining average efficiency. However, there is a possible increase in overall cooling efficiency as the wet phase shifts in magnitude are more prominent than dry shifts.

Nevertheless, there would be increasing variability in production due to the intensification of moderate events in wet and dry phrases. Such increasing variability would affect the power transmitted by the power plants and reduce the revenues generated. Further, it was found that HIW is responsible for both increasing and decreasing the risk of extreme events. Reversal of risk (HIW is causing opposite effects in warmer futures compared to historical period) was also discovered. For instance, for extreme magnitude wet phases in Central Asia and Southern and Eastern Asia and for magnitude and duration of dry events, in most regions (particularly in high latitudes), risk attributed to HIW reverses. Such reversal of risk indicates the significant non-linearity of changes in risk attribution, meaning HIW possibly helps increase the water availability for the power plants in certain regions, even in warmer climates. However, it would depend on cooling water demand which is affected by water temperature.

Hence, in the second step, the changes in water temperature were analyzed. Many researchers have studied the change in water temperature in the current and future world. But these studies project the changes for limited future scenarios. Moreover, the naturally forced scenarios have not been considered in any of the studies, and thus changes in water temperature have not been attributed to HIW. It is critical to realize the contribution of anthropogenic greenhouse gas emissions in the water temperature rise. A river temperature model, HEAT-LINK, was forced by CMIP6 atmospheric and land surface data, with and without the impacts of anthropogenic warming for historical and future periods. These changes were also compared with air and soil temperature as both these temperatures are important determinants of water temperature, apart from the solar radiations. A significant influence of HIW in future water temperature rise was uncovered, which

intensifies with radiative forcing. Similar observations are made for air temperature and soil temperature, but either had higher or lower attributed risk than for water temperature across the globe. However, in the historical scenario, the attribution of water temperature rise to HIW is much lower, in fact, negative at times. This is because even without anthropogenic heating, the average water temperature could have even increased in certain mid-latitude regions of the northern hemisphere, both in the past and at the end of the 21st century. Further, shifts in water temperature in an anthropogenic world show the most remarkable rise in temperature in summers, while water freezing reduces the impacts in winter. Air temperature and soil temperature, in contrast, demonstrates the most noticeable changes in winters. The spatial variability of the water temperature change also increases with radiative forcing in anthropogenically forced worlds.

In naturally forced worlds, regions like Southern Africa and western South America demonstrate higher spatial variability than in the anthropogenically forced historical scenario. Also, soil temperature shows the highest variability, followed by air temperature and least by water temperature. Differences are largest in the high latitudes for soil and air temperature compared to water temperature for both mean and variability of changes. These findings suggest that the water temperature changes can be very different from changes in air and soil temperature, particularly in the cold high latitude regions for long-term mean, spatial variability, and seasonality. Additionally, most of the temperature rise in water, air, and soil can be attributed to HIW. Nevertheless, the water temperature would be higher in certain regions, irrespective of anthropogenic greenhouse gas emissions. As temperature likely rises in all future scenarios in all seasons, cooling water demand would increase throughout the year. Also, as the compounding of warm and dry periods increases under climate change, the lower cooling efficiency periods for the power plants would elongate.

Finally, a power plant model was developed, and the discharge from CaMa-Flood and water temperature from HEAT-LINK are used as inputs for the model. The cooling water demand can be determined if the cooling parameters and thermodynamic efficiencies are known. The efficiency terms are obtained by utilizing a newly produced power plant dataset, developed by combining available data from available open-source power plant data and theoretical values in previous studies. Sensitivity analysis was performed, and theoretical values of water withdrawal were assumed to obtain the cooling parameters. Based on the water temperature and heat transfer equations, the water demand was calculated. The water availability was determined, considering environmental flow requirements, which govern the power production in the power plant. The resultant thermal effluent discharge was also computed and incorporated into the model. It must be noted that the model separates the different cooling systems (OT: power plants with once-through cooling system and CB:

power plants with a combined cooling system) during the simulation and employs a dynamic allocation of cooling tower (DACT) which allows the power plants with a combined cooling system to operate the cooling tower only during warm or water deficit periods. An additional allowance for water temperature rise (AAWTR) of thermal emission during warm periods is also incorporated to imitate such allowances that power plants receive. Such provisions (DACT and AAWTR) haven't been incorporated in previous models. Power production and thermal emission were estimated for two historical and five future scenarios. Results demonstrate an overall decline in power production in all future scenarios compared to the historical period for both OT and CB. However, the total power production increases on a global scale in a higher warming scenario (SSP370) than lower warming scenario (SSP245), which is due to an increase in water availability and declining dry period, despite the rise in water demand. Interestingly, the power production increases at a regional scale in certain regions like Alaska and Central Asia for all future scenarios with anthropogenic forcing. This is due to an increase in water availability (discharge) despite rising water temperature. It was also revealed that the water demand increases for OT while it decreases for CB. This happens due to an increase in the DACT under warmer climates and water shortages. Further, the compounding of dry and warm periods tends to increase, and the inefficiency of the power plants also increases during graver conditions (dry, warm, and dry-warm periods), particularly for OT. Finally, the risk of extreme decline in cooling efficiency attributed to HIW increases in higher warming scenarios for both cooling systems.

Additionally, the water temperature rise due to power plants by both cooling systems will be exacerbated at the points of thermal discharge. However, the value is much smaller for CB than OT, which implies the increased resilience of the CB due to DACT. Also, the water temperature rise at the location of CB is higher than OT, even though the thermal emission for CB reduces (due to DACT) in anthropogenically warmed futures, the reason being lower discharge at the location of CB. From this study, it was concluded that the cooling efficiency of power plants would reduce in the future, but with the adaptation of combined cooling instead of the once-through cooling, the resilience of the power plants can be improved. The thermal emissions of power plants will increase in the future but employing DACT can reduce thermal pollution. As the compounding of dry and warm periods increases, the consistency of power supplied by the power plants reduces. This issue can be confronted by utilizing a solar PV power plant in combination with thermal power plants, as solar PV plants have been reported to have higher potential during warmer periods. Finally, as the effect of temperature rise due to powerplants subsides downstream of the powerplants, decentralized power plants may serve better in the warmer future.

Chapter 1: Introduction

1.1 Climate Change in a nutshell

The Earth's climate is changing^{1,2}: there is a change in precipitation patterns^{3–7}, the evapotranspiration rates^{8–10}, runoff produced^{8,11–13} and the terrestrial water storage. The glaciers are melting^{14–16}, sea level is rising^{17–22}, there is a loss of biodiversity^{22–24}, and species are getting more vulnerable to extinction²⁵. Additionally, there are increasing disasters like floods^{26–28}, droughts^{27,29–32}, heatwaves^{33,34}, and wildfires^{35,36}. Most changes in climate are primarily caused by the global rise in temperature, what we commonly call global warming. Global warming is caused by greenhouse gases like CO₂, methane, water vapor, N₂O, and ozone. These gases absorb the heat that gets diffused into the earth's atmosphere from the earth's surface, causing the greenhouse effect³⁷. The greenhouse gas emissions have been rapidly increasing ever since the industrialization³⁸, in the late 18th century, and hence significantly creating an imbalance in the earth's climate system. Although some natural variabilities are caused by volcanic activities and solar radiation, most of the climate change that we witness today can be attributed to human-induced warming^{39–43}.

1.2 Impacts of Climate Change on Terrestrial Water Cycle

The impacts of climate change on various components of the terrestrial water cycle and their interactions have been broadly studied by many researchers^{1,2}. With increasing global warming, the global discharge in rivers increases, despite the regional decrease in the flow. This shift is primarily due to an uneven increase in precipitation and ET, pointing at the increasing pace and intensification of the terrestrial water cycle in a warmer world. With amplified temperatures, the water evaporates faster, increasing the atmosphere's moisture content and enhancing subsequent cloud formation. Further, the increased temperature provides room for more moisture—consequently, the precipitation intensities and frequencies increase, resulting in a more extensive runoff and discharge afterward. Furthermore, the melting of ice in the summer would increase in a warmer climate, further increasing the snow and glacier-fed river discharge. It would not be wrong to say climate change has changed the terrestrial water cycle's pace^{2,17}.

1.3 Impacts of Climate Change on Water Temperature

In the future, with higher radiative forcing, the air temperature would rise^{44–46}, so would the water temperature. The temperature might further increase in regions with declining discharge due to shallower water depth. The water temperature ascent would affect the aquatic ecosystem^{47–49} and

contaminant transport and reactivity. The higher water temperature would also mean a reduced dissolved oxygen level, suffocating aquatic life.

1.4 Impacts of Climate Change on Thermal Power plants

Most thermal power plants use water as their working fluid ⁵⁰. Steam at high pressure and high temperature is obtained by heating the water inside a chamber called a boiler. The steam then runs a turbine and needs to be cooled down inside a condenser to be heated again. The water used as working fluid is not replaced instead to avoid corrosion and scaling of equipment. Thus, cooling water is needed for power plants operation, which they draw primarily from freshwater resources like lakes, reservoirs, and rivers in case of inland plants, while power plants in the coastal region draw water from sea or ocean. With rising water temperature, the power plants would need more water to cool down the same amount of steam. Although water availability is not a problem for coastal power plants that use saline water, inland power plants face an acute shortage in case of dry and warm weather conditions.

Additionally, policy constraints on water consumption and thermal discharge bound the power plants ⁵¹ from producing electricity to their maximum capacity (known as label capacity). With the ever-increasing power demand, it will be challenging to supply the necessary power and follow environmental regulations. Power plants are projected to have a reduced production efficiency in the future⁵².

1.5 Impacts of Climate Change on Thermal Effluents

Apart from the warmer atmosphere, thermal power plants are significant contributors to increasing water temperature^{50,52–54}. Thermal power plants are found to have increased the water temperature by at least 0.5°C/ decade in certain regions⁵⁵. With increasing water temperature, this study hypothesizes, this temperature rise would also increase along with the extent of river length that gets thermally polluted, adversely affecting the ecological integrity of the aquatic ecosystem.

1.6 Climate models and experiments in CMIP6

Many researchers and research groups have developed physical and statistical models over the years to simulate the Earth's complex climate system and the shifts induced by climate change. These models, running at hourly to decadal-scale⁵⁶ for both regional and global coverage, simulate historical and future periods. This study uses such global model(s) available under the World Climate Research Programme's (WRCP's) 6th Phase of Coupled Model Intercomparison Project (CMIP6). Several

experiments are performed by these global models, with a baseline formed by the pre-industrial controlled (pi-Control) simulations⁵⁷. These pi-Controlled simulations are forced with constant radiative forcing, greenhouse gas concentration, and other forcing constraints at 1850 levels, the period considered as the onset of industrialization. The hist-nat experiments simulate the natural climatic conditions, with only orbital changes, solar forcing changes, and volcanic activities, which account for the natural variability in climate change. At the same time, the historical simulations represent the earth systems with full anthropogenic forcings along with the natural forcings. Apart from this, several other controlled experiments are performed⁵⁷ with controlled CO₂, aerosols, land cover, among others. Future ScenarioMIPs combine Representative Concentration Pathways or RCPs⁵⁸ and Shared Socioeconomic Reference Pathways or SSPs⁵⁹ in CMIP6 climate models. Depending on the possible amounts of radiative forcings, various RCPs are defined (RCP 2.6, RCP 4.5, RCP 6.0, and RCP 8.5) corresponding to the value of the radiative forcing in W/m² (as given in Table 1-1). Also, five Shared Socio-economic Pathways (SSPs) are defined based on adaption policies and mitigation challenges, which are as follows (also shown in fig 1.1)

1. SSP1: Sustainability – low mitigation and adaptation challenges
2. SSP2: Middle of the road – intermediate mitigation and adaptation challenges
3. SSP3: Fragmentation/regional rivalry – high mitigation and adaptation challenges
4. SSP4: Inequality – high adaptation and low mitigation challenges
5. SSP5: and Conventional/fossil-fueled development – high mitigation and low adaptation challenges

A matrix of RCP and SSP is used to define possible SSP-RCP combinations to fill in essential gaps that forcings alone could not suffice⁵⁷. SSP1-RCP2.6, for example, is a combination of SSP1 and RCP 2.6 (henceforth represented as SSP126). Similarly, SSP2-RCP4.5 (SSP245), SSP3-RCP7.0 (SSP370), and SSP5-RCP8.5 (SSP585) are some feasible combinations that are used in this study. These combinations result in different global temperatures at the end of the century⁶⁰, as shown in fig 1.2.

Further, each of the modeling groups performs several ensembles for a particular experiment, with variations in realization (r), initialization (i), model physics (p), and forcings (f). Different combinations of different r, i, p, and f give different results. For instance, r1i1p1f1 has a slightly different output than r2i1p1f1. However, a change in forcings might result in larger differences. Such a multi-ensemble approach is used to reduce the uncertainties of forcing data as well as model uncertainty to a certain degree. Another approach to diminish uncertainty is to use multiple models. A multi-model approach can reduce both model uncertainty and uncertainty in input

forcing's to a significant extent. It is important to note that identical ensemble variant names do not mean different models use the same data and initial conditions. More details on data and model for CMIP6 experiments is available at <https://esgf-node.llnl.gov/search/cmip6/> .

Table 1.1: The four RCPs (as given in Moss et al., 2010) *MESSAGE, Model for Energy Supply Strategy Alternatives and their General Environmental Impact, International Institute for Applied Systems Analysis, Austria; AIM, Asia-Pacific Integrated Model, National Institute for Environmental Studies, Japan; GCAM, Global Change Assessment Model, Pacific Northwest National Laboratory, USA (previously referred to as MiniCAM); IMAGE, Integrated Model to Assess the Global Environment, Netherlands Environmental Assessment Agency, The Netherlands.

Name	Radiative forcing	Concentration (p.p.m.)	Pathway	Model providing RCP*
RCP8.5	>8.5 W m ⁻² in 2100	>1,370 CO ₂ -equiv. in 2100	Rising	MESSAGE
RCP6.0	~6 W m ⁻² at stabilization after 2100	~850 CO ₂ -equiv. (at stabilization after 2100)	Stabilization without overshoot	AIM
RCP4.5	~4.5 W m ⁻² at stabilization after 2100	~650 CO ₂ -equiv. (at stabilization after 2100)	Stabilization without overshoot	GCAM
RCP2.6	Peak at ~3 W m ⁻² before 2100 and then declines	Peak at ~490 CO ₂ -equiv. before 2100 and then declines	Peak and decline	IMAGE

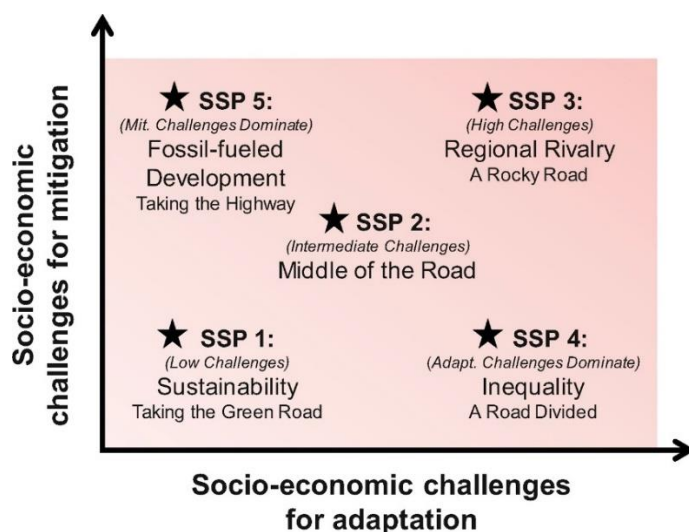


Figure 1.1: Possible Shared Socio-economic Pathways, *adapted from* O'Neill et al., 2017

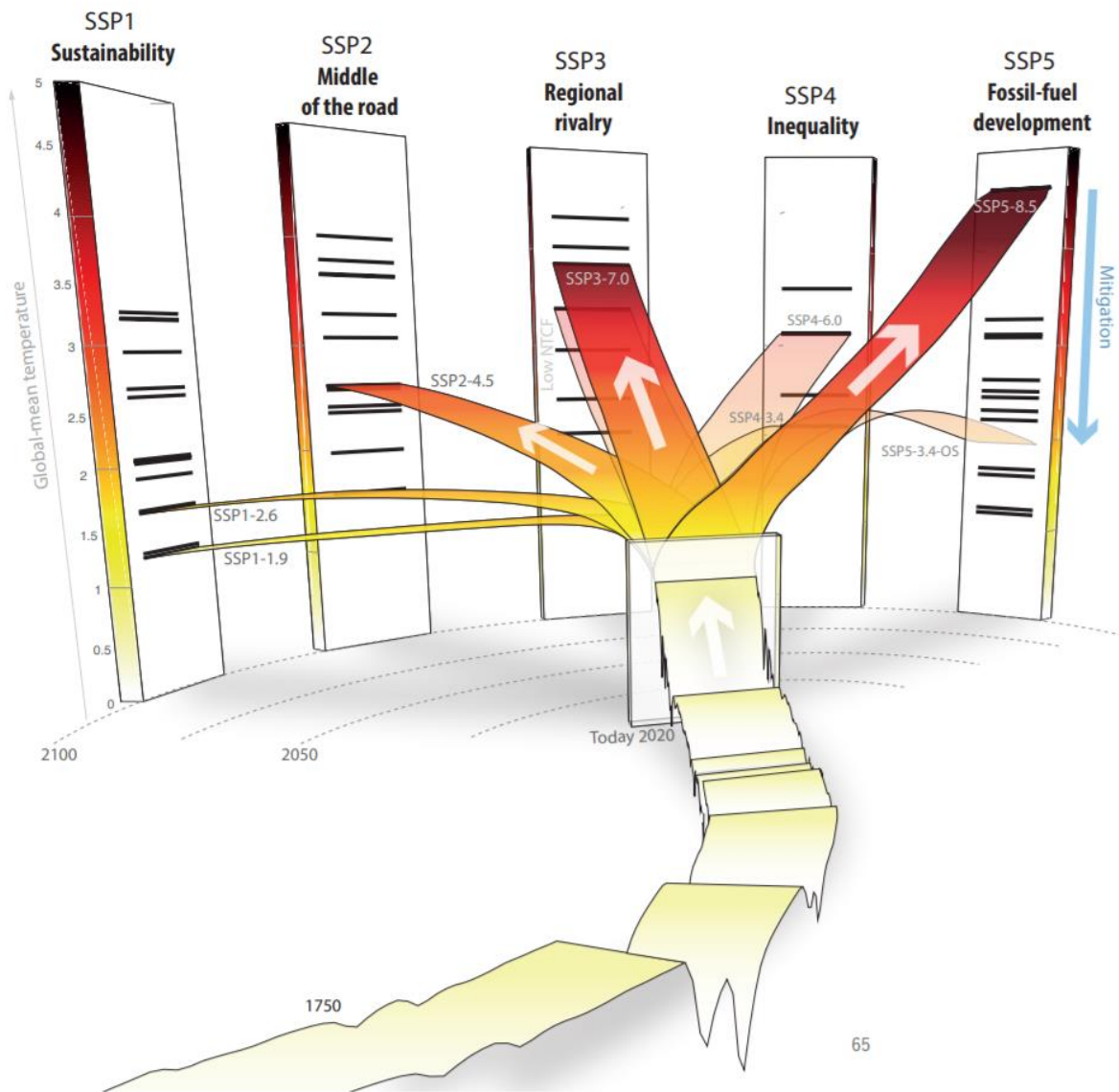


Figure 1.2: Combined SSP-RCP scenarios at the end of the century adapted from Meinshausen et al., 2019

1.7 Rationale, Significance, and Novelty of the Research Work/ Philosophy Behind the Doctorate and Novelty of the Research Work

Climate change has become a pressing concern than ever before. We have lived the changes in rainfall patterns and temperature rise. Understanding how climate change is influencing the terrestrial water cycle is essential. We have witnessed increasing disaster occurrences in the past decade. In the year 1999, a super-cyclone hit the East coast of India (Odisha). It was devastated. Strong winds and heavy precipitation destroyed thousands of lives and livelihoods⁶¹. Till 2012 there wasn't any cyclone to match the 1999's might. However, in the next eight years, at least three cyclones could cause such havoc^{62,63,64}, flooding the state for days, with many lives lost and destruction worth millions of dollars.

However, Odisha had learned to cope with cyclones, and the actual damage to life and property was much smaller^{65–68}. But when resilience is the only option, the question that comes to mind is: what is in store for us in the future? Will there be more floods or droughts, or both? Not just extreme events, but what would be the changes in everyday life? Will we have more water or less every day for usage?

With the COVID-19 pandemic, we have realized the importance of nature and what havoc it can bring upon if warnings are not heeded. Many people claimed COVID-19 to be payback for sins against nature⁶⁹. But what many people failed to realize is that even many of the so-called natural calamities intensify due to anthropogenic impacts on the climate. A portion of most disasters like heavy precipitations, floods, droughts, heatwaves, and forest fires, along with the losses that postdate, can be attributed to human-induced warming. But the question is: to what extent? How much can climate change be attributed to human-induced warming?

Studying the rising water temperature is also essential. As discussed in sections 1.3-1.5, climate change significantly impacts aquatic life and thermal power plants. Power supply has been the heart of development⁷⁰. Hence, global warming is a challenge to the power industry and development in general. Also, only a few studies have presented thermal pollution as a challenge. Hence quantification of such thermal pollution is vital. It is critical to understand the impacts of climate change and mitigate wherever and whenever possible. If mitigation is not feasible, adaptation becomes necessary to combat climate change. Hence policies need to be drafted to save the environment alongside development. Sustainable development is not a mere option anymore if the environment must be protected.

This dissertation presents a global view of climate change impacts on the hydrodynamics (water cycle) and thermodynamics (water temperature) of freshwater resources by binding them with the associated anthropogenic elements (thermal power plants and thermal pollution). Further, it proposes few policies to improve thermal power production and diminish thermal pollution.

Traditionally, moisture content, P, and ET have been used to quantify drying and wetting. A novel approach to quantify the drying and wetting over land and associated asymmetry in the shifts of dry and wet phases of riverine discharge has been proposed in the next chapter. Also, previous studies have attributed the increased risk of extreme events like floods (i.e., extreme wet events) and droughts (i.e., extreme dry events) to anthropogenic warming. However, in the second chapter, a new 'SymFAR' index has been proposed that not only measures the increase in the attributed risk of extreme climate but also the decrease in risk due to anthropogenic warming. The third chapter quantifies the impact of climate change on river water temperature and attributes it to anthropogenic

warming, which has been missing in previous studies. It also focuses on the non-linearity of water temperature changes with warming. For the fourth chapter, a new thermal power plants model (more details in chapter 4), with scope for modification of policy constraints, is amalgamated with a previously developed physical water temperature model incorporating a freezing-thawing cycle (more details in chapter 3). The power plant model also segregates the once-through cooling system from the tower-cooling system, which has been missing in the previous studies⁵². The influence of climate change on the power industry in terms of power production and policy constraints' prominence is examined. Water temperatures rise due to power plants are also analyzed. In this course of the dissertation, several Sustainable Development Goals have been encompassed. These are highlighted in fig 1.3.



Source: <https://www.un.org/sustainabledevelopment/wp-content/uploads/2019/08/E-SDG-2019-posters.zip>

Figure 1.3: Sustainable Development Goals Involved in this work (colored)

1.8 Thesis Outline

Chapter 1 directed a general introduction to the dissertation. It also discusses the work's motivation, importance, and originality. The details of climate change impacts on freshwater discharge and water temperature have been discussed in the subsequent chapters. The gaps in the previous research have been incorporated in each chapter separately.

Chapter 2 discusses the changes in the terrestrial water cycle and their implications on riverine discharge. Daily discharge is calculated from CMIP6 runoff forced CaMa-Flood⁷⁷. The shifts in intensity and persistency of daily discharge variability have been studied for dry and wet phases of moderate

and extreme events. The detection and attribution of such changes due to anthropogenic warming have also been encompassed.

Chapter 3 examines the changes in water temperature and attributes these changes to anthropogenic climate change. Water temperature is calculated using HEAT-LINK⁷⁸. Further, the discrepancy in water temperature changes against air temperature and ground temperature changes have also been discussed. Sensitivities in water temperature shifts with warming are quantified, and the changes in water temperature are attributed to human-induced warming.

Chapter 4 describes the model development to simulate thermal power production based on cooling efficiency and incorporate the anthropogenic impacts on water temperature. Only thermal power plants are considered in this study as they are the most significant contributors to thermal pollution and are also more vulnerable to water temperature rise. The water withdrawal and return flow from power plants are incorporated into the HEAT-LINK⁷⁸. The efficiency of power production in the thermal power plants, which use different cooling systems and fuel types, is estimated. Further, it focuses on the consequences of climate change on thermal power production. Additionally, it furnishes thermal power plants' thermal pollution incorporating the subjection of climate change in the natural world for historical and future scenarios.

Chapter 5 provides conclusions drawn from the work and proposes policy implications from this study to improve power production and control thermal pollution. The future scope of the research is also presented.

Chapter 2: Changes in the Terrestrial Water Cycle: climate change impacts on water availability

2.1 Introduction

2.1.1 The Terrestrial Water Cycle and its budget

Water is a circulating global resource ² and is replenished by nature in the form of precipitation. During the precipitation process, some amount of water is trapped in the canopy and constructional structures and is eventually lost as evaporation before reaching the ground surface. This process is called interception. The rest of the water reaches the ground either in the form of rain or snow. The land surface absorbs some amount of rain, and some amount is used up in filling the depression storage, including lakes, small puddles, and ditches. The rest of the water flows on the ground surface as surface flow. A proportion of surface flow is lost as evaporation and rest flows in streams and sooner or later connects to a river or a lake. A part of the water absorbed by the soil infiltrates into the ground, recharging the groundwater. Some part of it is absorbed by roots of shrubs and trees and is eventually lost as transpiration. The total evaporation along with transpiration is combinedly called evapotranspiration (ET). The rest of the ground absorbed flows slowly under the surface, known as subsurface flow, and joins the surface flow in due course. Some amount of snow straightway melts and flows as water, while others become a part of permanent ice storage and glaciers. These glaciers melt very slowly and contribute to the baseflow of many rivers and streams. The flow of water that we see in streams and rivers is a combination of surface and sub-surface flow that ultimately comes from precipitation (P) minus evapotranspiration (ET). The part of P-ET that eventually contributes to flow in rivers and streams is called runoff (R). The remaining/deficit water is the change in water storage (S). Hence, the terrestrial water budget equation can be obtained as:

$$P-ET=R+ dS/dt$$

Equation 2-1

The rate at which the water flows in the rivers or streams is called discharge (Q). These rivers and streams either end up in the ocean (and sea) or terminal lakes. Water gets evaporated from the water surface of lakes, rivers, and oceans. ET enhances the atmospheric moisture content that gets transported by wind, forming the water vapor flux (Q_v). The water vapor eventually condenses and forms clouds, which comprises the precipitable water (W). In these clouds, when condensed tiny water (snow), particles (crystals) amalgamate to form a drop (flake) that is heavy enough and start to fall again on the ground in the form of rain (snow). Hence this establishes the atmospheric water budget.

$$Q_v - dW/dt = P - ET$$

$$\text{Equation 2-2}$$

Oki and Kim ⁷⁹ provided a combined atmospheric and terrestrial water budget equations and made global estimates of the critical water fluxes, area, and storage components (Fig 2.1), including water use for irrigation, domestic and industrial activities.

$$Q_v - dW/dt = P - ET = R + dS/dt$$

$$\text{Equation 2-3}$$

The entire process of water precipitation, evapotranspiration, terrestrial transportation inform of discharge, atmospheric transport in the form of water vapor flux, condensation, and precipitation again, forming a cyclic flow of water is called the hydrological cycle.

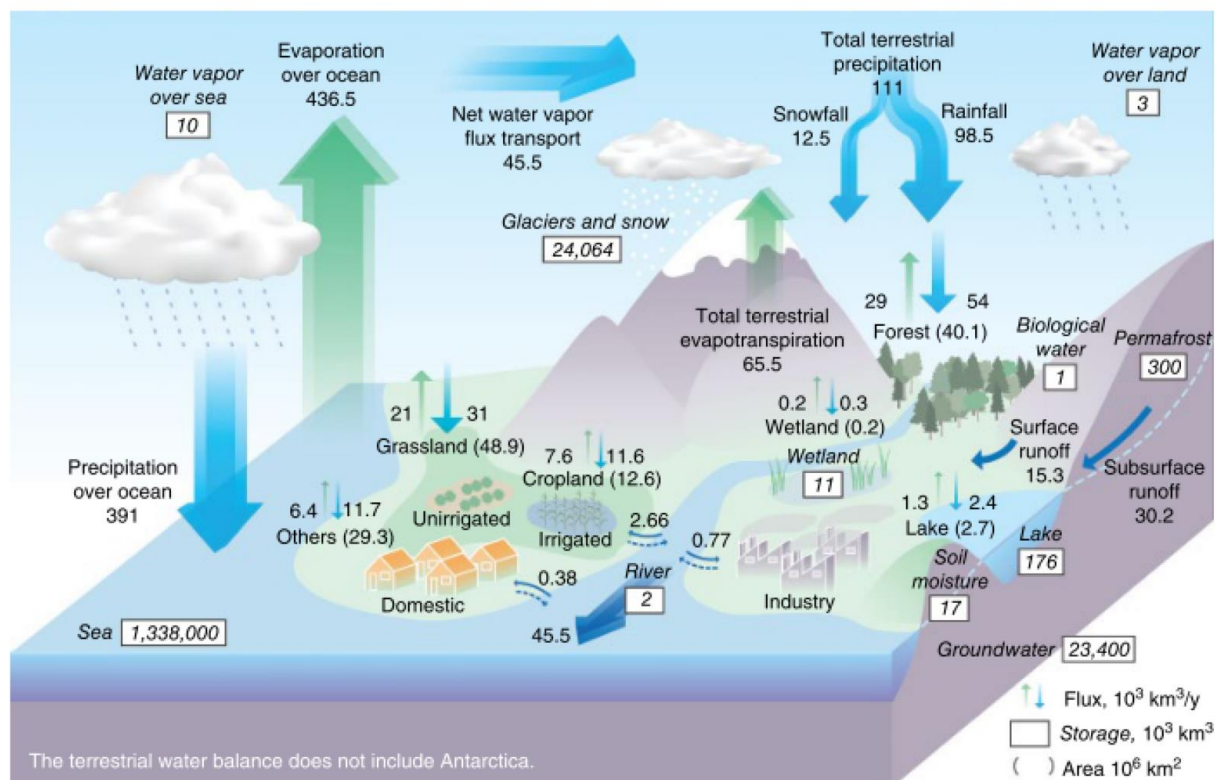


Figure 2.1: The global hydrological cycle [adapted from Oki and Kim, 2016⁷⁹]

2.1.2 Hydrological cycle under Climate Change

Earth's hydrological cycle is being affected by global warming. Climate change affects critical water fluxes like precipitation, evapotranspiration, and moisture transport; consequently, the spatio-temporal variability of water flow changes. With amplified temperatures, the water evaporates faster,

increasing the moisture content of the atmosphere and enhancing subsequent cloud formation. Further, the increased temperature provides room for more moisture—consequently, the precipitation rate and volume increase, resulting in a more extensive runoff and discharge afterward. This intensification has been pointed out in numerous previous works². Furthermore, the melting of ice in the summer would increase in a warmer climate, further increasing the discharge in snow and glacier-fed river.

As a result, some areas might become drier, while some might become wetter than what they are today⁴⁷. Several studies have reported significant variations in mean, trend, and seasonality of streamflow for both the past^{80,81} and the future worlds and changing the climate extremes like floods and droughts^{6,7,40,82–85} as consequences of climate change. Further, these changes are reported not to be linear with increasing global temperature⁸⁶. Drying and wetting of a region occur by changes in discharge. However, an event-wise analysis of these dry and wet changes in discharge is missing. Also, there lies an asymmetry in the distribution of such dry-wet changes in both spatial and temporal scales across and within historical and future worlds.

2.2 Gaps in Previous Research and Scope of this Study

A vast number of previous studies have focused on the changes in mean, trend, seasonality, and variability of flow^{80,81,87–89} for both past and the future worlds and climate extremes like floods and droughts^{6,7,40,82–85} as a consequence of climate change. However, none of the studies have shown the mechanism of change in the terrestrial water cycle associated with discharge changes. The mechanism of change in the hydroclimatic background³ that subsequently causes the changes in discharge, but only a few shows what changes occur within discharge, in terms of magnitude or frequency (or duration) that alters the available water⁸⁵ or disasters like floods and droughts. Further, previous studies considered only runoff at monthly⁸⁵ or annual² scales for computing the impact of climate change.

Attribution of extreme event risk to climate change has been done by several researchers^{39,90–93} in the past. However, these studies focus on the increasing risk due to climate change. Climate change not just increases, but also decreases extreme events, which has been recently pointed out by a few researchers; however, the decrease in risk due to human-induced warming has not been quantified. This study develops a new index to quantify both increase and decrease in attributed risk, which the previous studies lack. The index is used to quantify risks associated with changes in discharge attributes considered in this study, attributed to human-induced warming.

Hence the questions this chapter addresses are as follows:

- 1) What is the mechanism of changing discharge in terms of magnitude and duration of wetting and drying?
- 2) Which changes are more prominent for moderate and climate extreme events: wetting or drying changes?
- 3) How are magnitude changes related to duration shifts?
- 4) How much is human-induced warming responsible for such changes in wetting and drying, particularly for extreme events?

2.3 Data and Methodology

2.3.1 Hydroclimatic Data

The global datasets for daily-scaled total runoff (surface runoff + subsurface runoff) from 11 models (BCC-CSM2-MR, CanESM5, IPSL-CM6A-LR, MRI-ESM2-0, NorESM2-LM, ACCESS-CM2, EC-EARTH3, INM-CM4-8, INM-CM5-0, MIROC6, MPI-ESM1-2-HR) under the sixth phase of Coupled Model Intercomparison Project (CMIP6), which began under the blanket of the World Climate Research Programme (WCRP), are used in this study. More details about the CMIP6 can be found at their official website (<https://esgf-node.llnl.gov/projects/cmip6/>) Three experiments with full anthropogenic including two future scenarios (SSP1-2.6 and SSP5-8.5) from ScenarioMIPS and a historical simulation, are considered for each of the 11 models. Data for one ensemble ("r1i1p1f1") per model is selected from the WCRP website (<https://esgf-node.llnl.gov/search/cmip6/>). Analogous monthly data for P, ET, and R is also obtained from the same source and scaled to a spatial resolution of 0.25°.

2.3.2 Computation of Discharge

The daily runoff gridded dataset from each CMIP6 model ensemble is used as input for the CaMa flood model. The input runoffs are scaled to 1°X1° grids using bilinear interpolation. The total discharge is computed using the CaMa flood model at a spatial resolution of 0.25°X0.25°. The leap day values are considered the average of previous and next day for the models with 365 days of runoff, even for leap years. A period of 30 years for historical (1960-1990) simulations (historical) and future (2071-2100) simulations (SSP1-2.6 and SSP5-8.5) is chosen as a representative period for analysis. The multi-model historical mean and future changes in the discharge are plotted in figure 2.8.

The lower extreme (p10), median (p50), mean and upper extreme (p90) values of discharge are computed for historical and two future scenarios. The changes in these values are calculated for future scenarios compared to the historical scenario and are represented in figure 2.8 and figure 2.9. Additionally, mean P, ET, and R are computed for the historical and future scenarios from the monthly

data. The multi-model historical mean and future changes in P, ET, and R are represented in figure 2.11.

2.3.3 Event-wise analysis

An event-to-event analysis of global discharge data has been done. The mean of discharge (for the representative 30 years) for the historical scenario is considered the datum to classify a day as a dry day or a wet day for all three experiments (historical, SSP1-2.6, and SSP5-8.5), dividing the discharge time series into a dry and wet phase (as shown in figure 2.2). On a particular day, if the discharge is higher than the mean, it is considered a wet day, otherwise considered a dry day. An event is defined as a series of consecutive dry days or a series of consecutive wet days. If the considered period starts with a dry (wet) phase and ends with a wet (dry) phase, the total number of dry and wet events is equal. There is a possibility that the time series may start and end with the same type (dry/wet) of the event. Hence, the maximum difference in the number of dry and wet events can be one. Such a scheme is executed to achieve a closed water budget.

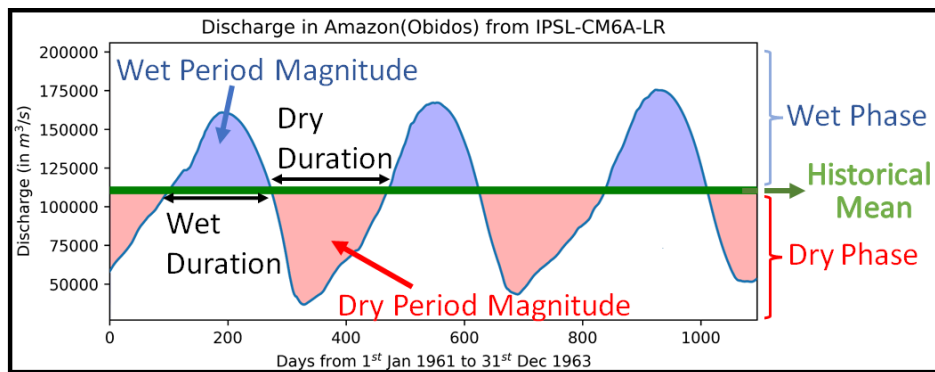


Figure 2.2: Magnitude and Duration for a discharge time-series, by dividing it into a dry and wet phase using the long-term historical mean discharge. Similar dry and wet phases of discharge are demonstrated for three more rivers in figure A1.

The Magnitude of dry deficit (M_{dry}) and wet excess (M_{wet}) is computed as the amount of deficit and excess water (in km^3) to the datum (Historical mean discharge) for each experiment. The length of each dry (wet) event is denoted as the dry Duration, " D_{dry} " (wet Duration, " D_{wet} ").

$$M = \sum_{k=d1}^{d2} (Q_{expt}(k) - \bar{Q}_{hist}) \quad \text{Equation 2-4}$$

$$D = 1 + d2 - d1$$

Equation 2-5

Where, $Q_{\text{expt}}(k)$ is the discharge on a given day k for a given experiment (historical, ssp126 or ssp585), \bar{Q}_{hist} is the average discharge for the historical period, $d1$ and $d2$ are the starting and ending days for a continuous period for which the, Q_{expt} is greater (wet period) or less (dry period) than the mean discharge. The 50th and 99th percentile of Magnitude and Duration for the dry and wet phase for all models for the 30year reference period of historical and future experiments were calculated for each grid cell.

2.3.4 Calculation of Asymmetry

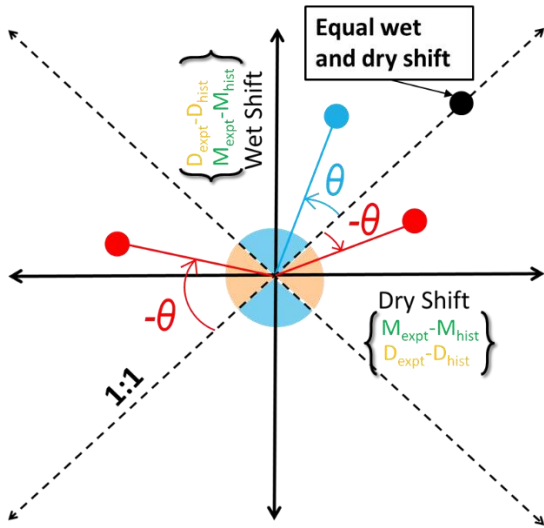


Figure 2.3: Calculation of asymmetry. The cartesian plan has dry shift as abscissa and wet shift as ordinate.

Θ is the angle formed by the slope of a point in a Cartesian plane with the dry shift as abscissa and wet shift as ordinate and 1:1 line, where $\text{shift} = \text{VAR}_{\text{expt}} - \text{VAR}_{\text{hist}}$, where VAR can be Magnitude (M) or Duration (D) and expt is either SSP126 or SSP585. Hence, $\Theta \in (-90^\circ, 90^\circ)$. Asymmetry is defined as:

$$\text{Asymmetry} = \frac{\Theta}{90^\circ}$$

$$\text{Asymmetry} \in (-1, 1)$$

Asymmetry (Θ) is positive when the absolute value of wet shift is higher than dry shift (anti-clockwise moment)

Asymmetry (Θ) is negative when the absolute value of dry shift is higher than wet shift (clockwise moment)

It must be noted that positive (negative) asymmetry does not imply larger wet (dry) events. It means that the absolute shift is larger for wet (dry) events against the shift for dry (wet) events.

2.3.5 Producing new ensembles from existing model ensembles

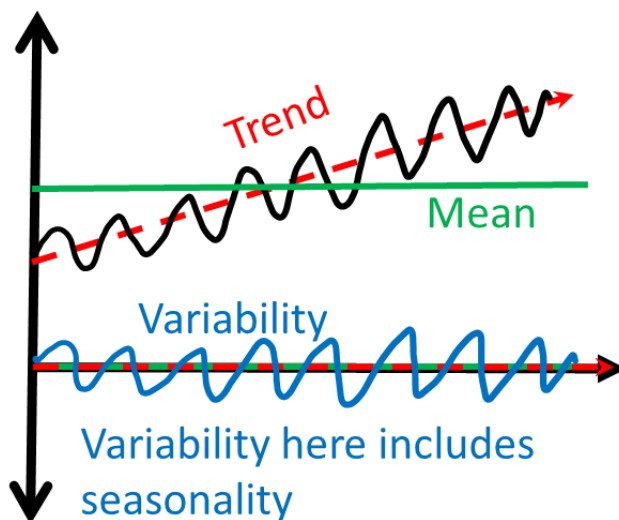


Figure 2.4: Trend, mean, and variability for a time-series

As limited ensembles were available for hist-nat, new ensembles are produced from the existing ones. This is achieved by combining the mean, trend, and variability of different models to form a complete time series. Let us consider three models A, B, and C.

New ensemble = Trend (A) + Mean (B) + Variability (C)

In this manner, for four models, 4^3 permutations are possible. Hence, 64 new ensembles are produced from the existing four models for the input runoff data.

2.3.6 Symmetric Attribution of Risk

Fraction of Attributable Risk (FAR) to Anthropogenic climate change from 4^3 newly created ensembles for each of the four scenarios (Hist, Hist-nat, SSP126, and SSP585).

$$\text{Risk Ratio} = \text{RR} = \frac{P_{\text{expt:th}}}{P_{\text{nat:th}}} \quad \text{Equation 2-6}$$

$$\text{FAR}_{\text{expt}} = 1 - \frac{1}{\text{RR}} = 1 - \frac{P_{\text{nat:th}}}{P_{\text{expt:th}}} \quad \text{Equation 2-7}$$

where $P_{\text{nat:th}}$ is the probability of exceedance of a threshold (th) for an experiment in natural only forcings among the 64 ensemble members.

$P_{\text{expt:th}}$ is the probability of exceedance of a threshold (th) for an experiment with forcings full anthropogenic forcings.

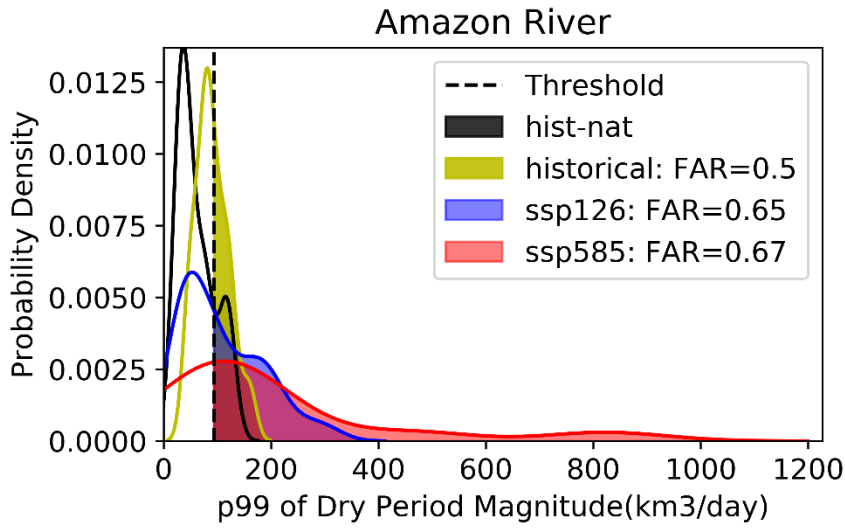


Figure 2.5: FAR for Amazon (at the outlet, fig 2.10), with threshold= ensemble mean + ensemble standard deviation of 99th percentile of magnitude.

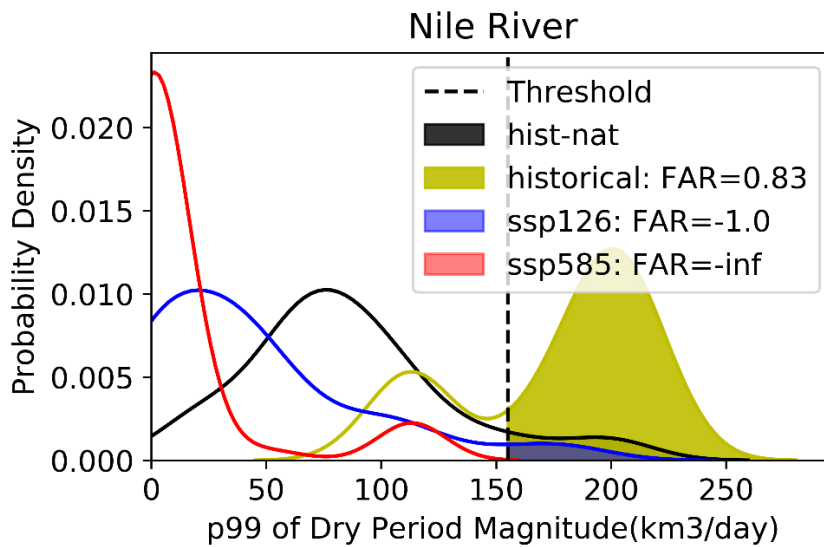


Figure 2.6: FAR for the Nile, with threshold= ensemble mean + ensemble standard deviation of 99th percentile of magnitude

Symmetric-FAR (SymFAR) is defined as follows

$$\text{SymFAR}_{\text{expt}} = \begin{cases} 1 - \frac{1}{\text{RR}} & \text{if } \text{RR} > 1 \\ \text{RR} - 1 & \text{if } \text{RR} < 1 \end{cases} \quad \text{Equation 2 – 8}$$

If $\text{SymFAR} > 0$, $\text{SymFAR} = \text{FAR}$, i.e., the probabilistic risk attributed to the presence of anthropogenic warming increasing the risk of an extreme event

When $\text{SymFAR} < 0$, SymFAR is the probabilistic risk attributed to the presence of anthropogenic warming reducing the risk of an extreme event, and the negative sign indicates this reduction. Anthropogenic impacts reduce to 0 when $\text{SymFAR} = -1$

SymFAR is calculated for extreme (p_{99}) value of magnitude and duration for both dry and wet phases. We consider the median of the 99th percentile values of hist-nat ensembles as the threshold for exceedance.

2.3.7 Considering multi-model mean

For the calculation of discharge, P, ET, and R, mean values of 10 models (BCC-CSM2-MR is) are considered. For relative changes in discharge, the multimodel mean of relative discharge change of each model is calculated, and then the mean of ten models is considered. The same approach was followed for calculating ratio to historical values for magnitude and duration for global and basin-wise changes. However, for calculating asymmetry, the multimodel mean value of changes from historical values of the wet period is divided by dry period to get the slope of the line and finally asymmetric angle and asymmetry. Such an approach is considered as the asymmetric angle is not a continuous measure. It has points of discontinuity at $\pm 90^\circ$ (135° and -45° on dry-wet cartesian plain), where small changes in values of wet and dry shifts may lead to drastic changes in the asymmetry.

2.4 Results

2.4.1 Validation

Out of more than 9000 station data from the GRDC database, the small catchments ($< 10^5 \text{ km}^2$) and low significance of correlation ($p\text{-value} < 5\%$) were screened out. Along with this, the catchments with a small observational period (< 5 years) were also eliminated. Water-stressed catchments were determined by multi-model means values of total water withdrawal, comprising water withdrawal from irrigation, manufacturing, livestock, and domestic demands, which are calculated from the available ISIMIP data (Table 2.1). The total water withdrawal was divided by the mean of runoff and

calculated as the water stress index for each impact model multi-model. The catchments with average water stress over a value of 0.4 are considered water-stressed ² and were omitted in the validation.

Table 2.1: Details of ISIMIP2b Data

Feature	ISIMIP Impact Model	Climate Forcing
Irrigation Water Withdrawal and Total Runoff	PCR-GLOBWB	GFDL, IPSL, MIROC5, HADGEM2
	LPJML	GFDL, IPSL, MIROC5, HADGEM2
	H08	GFDL, IPSL, MIROC5, HADGEM2
	MATSIRO	GFDL, IPSL, MIROC5, HADGEM2
Manufacturing Water Withdrawal	PCR-GLOBWB	-
	LPJML	-
	H08	GFDL, IPSL, MIROC5, HADGEM2
	MATSIRO	-
Livestock Water Withdrawal	PCR-GLOBWB	GFDL, IPSL, MIROC5, HADGEM2
	LPJML	-
	H08	-
	MATSIRO	-
Domestic Water Withdrawal	PCR-GLOBWB	GFDL, IPSL, MIROC5, HADGEM2
	LPJML	-
	H08	GFDL, IPSL, MIROC5, HADGEM2
	MATSIRO	-

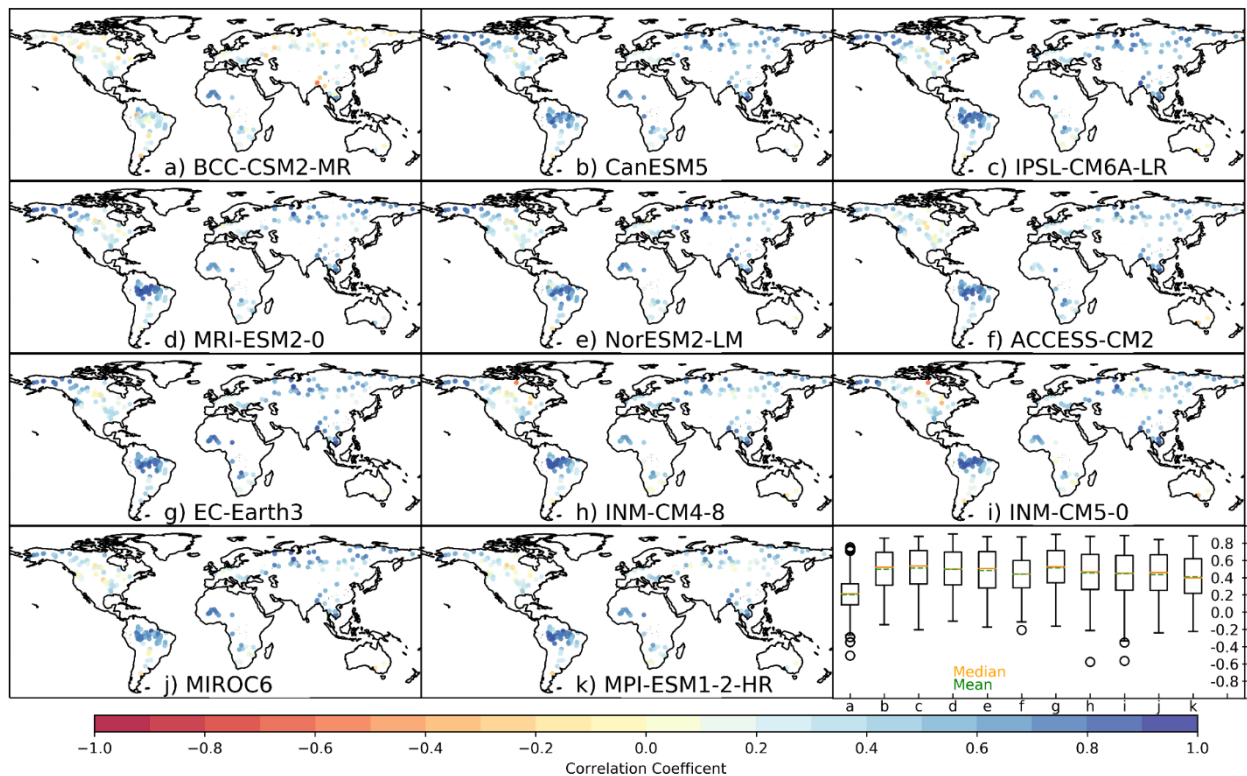


Figure 2.7: Validation of model simulation. Panels a to k show the correlation coefficient of observed daily discharge and daily discharge from 11 CMIP6 models, across 227 GRDC gauge stations, for all available data from 1961 to 1990. Most models perform reasonably well, except for BCC-CSM2-MR.

The summary of performance for each model is represented in a box plot in the last panel. The box plot shows the median (orange line) along with the lower quartile (25th percentile) and the upper quartile (75th percentile) of Correlation values for the available gauge stations. The whiskers show the range of the correlation coefficient values, excluding the outliers

All models, except BCC-CSM2-MR, perform reasonably well in simulating the daily discharge in the remaining 227 large GRDC catchments, showing a correlation of about 0.5 (Fig. 2.7). Due to inadequate performance, BCC-CSM2-MR remained unused in further analysis. Most of the models show relatively low performance in Canada, Central and Eastern America, Southern South America (except ACCESS-CM2 and EC-Earth3), and Australia. We found a high model performance in the tropical regions, possibly due to a strong seasonality.

2.4.2 Global changes in discharge

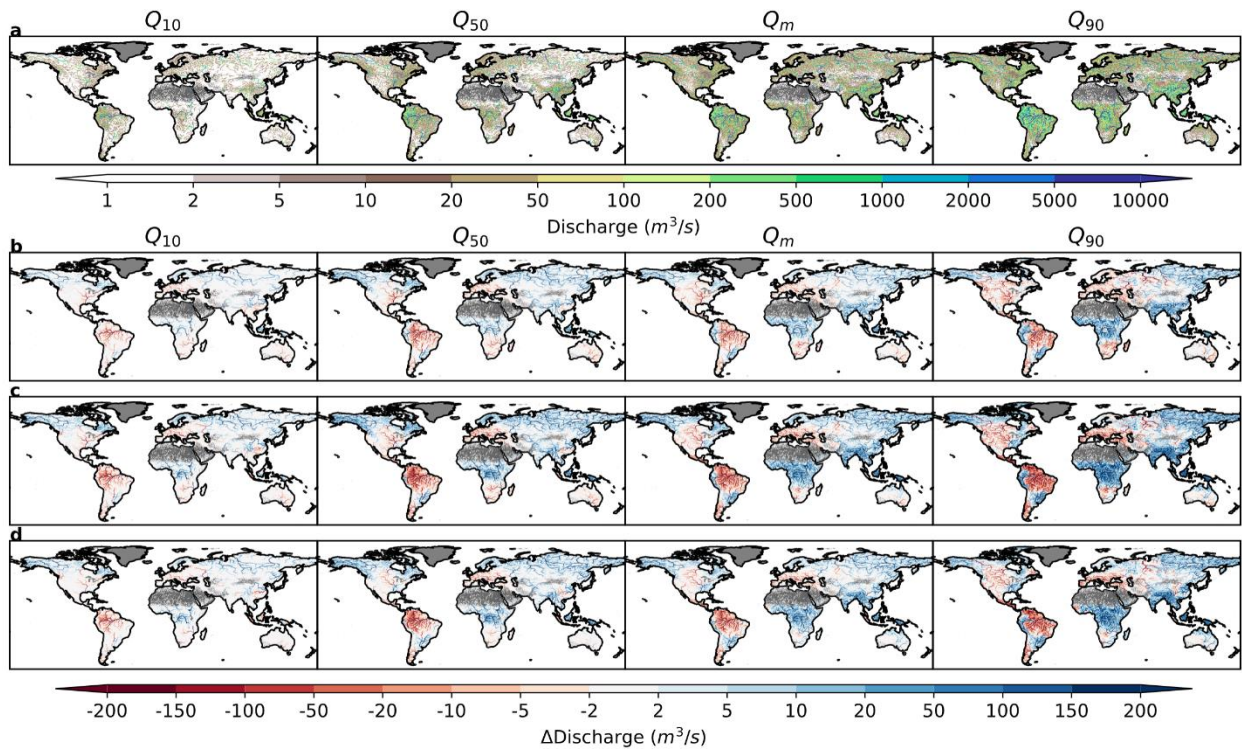


Figure 2.8: Global changes in mean, median, and extreme river discharge. The figure illustrates the historical values of discharge (a, b, and c) and the changes in discharge (d-i), for two future scenarios (SSP126 and SSP585), in excess to historical values of discharge, in its lower extreme (left column), median value (central column) and upper extreme (right column). The difference in the two future scenarios is also shown in panels j, k, and l.

The multi-model mean of freshwater flow simulated from 10 CMIP6 GCM runoffs indicates a global increase with increased radiative forcing, although declining trends are also expected in certain

regions (Fig. 2.8) for both SSP126 and SSP585. The global average discharge (except Antarctica, Greenland, and dry areas with average discharge less than $0.5\text{m}^3/\text{s}$, shaded in grey color in Fig. 2.8) increases from $197.7\text{m}^3/\text{s}$, in the historical scenario, to $206.3\text{m}^3/\text{s}$ in SSP126 and further to $222.5\text{m}^3/\text{s}$ in SSP585. The decline can be seen in (Fig. 2.8) most regions of Central and Eastern North America, Amazon, Southern South America, Southern Africa, Central Europe, and the Middle East, constituting 34% and 28% of the landmass, respectively for SSP126 and SSP585 future worlds. The low flow of discharge variability (10th percentile or P10) declines for a larger share of land (42% for SSP126 and 39% for SSP585), while the high flow (90th percentile or P90) increase is even more significant (64% for SS126 and 69% for SSP585). Further, about 60% of the area shows an intensification (increase in change) of mean discharge changes, with additional warming, from SSP126 to SSP585. Most differences between the SSP126 and SSP585 worlds (Fig. 2.8d) are larger than the historical and SSP126 scenarios (Fig. 2.8b).

2.4.3 Global changes in hydroclimatic background

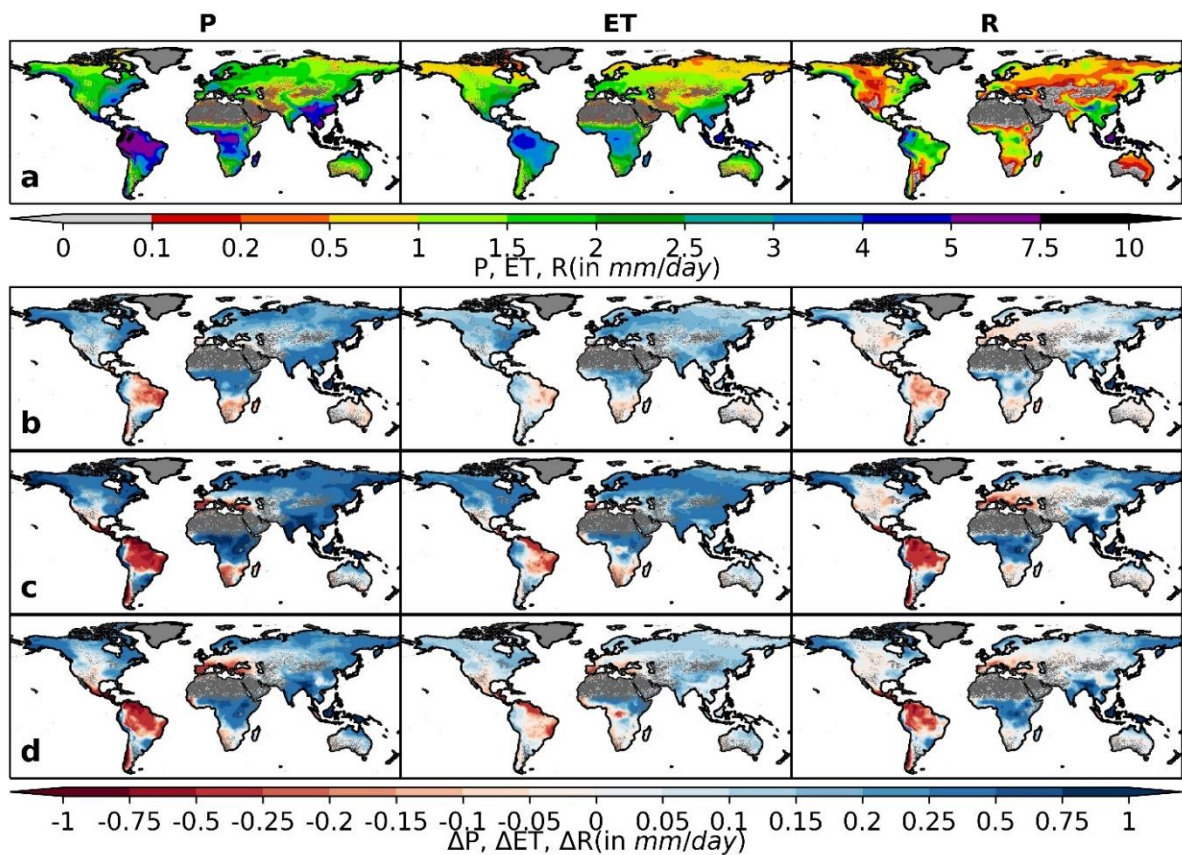


Figure 2.9: The figure depicts the hydroclimatic changes that trigger the changes in discharge. The 1st column represents Precipitation (P), the 2nd represents Evapotranspiration (ET), and the 3rd represents Runoff (R). The first row (a-c) shows the historical values of the hydroclimatic variables, while the 2nd and 3rd row (e-l) shows the future changes (for ssp126 and ssp585, respectively) of values in comparison to historical values.

The global overland P, overland ET, and R (Fig. 2.9) increase with increased warming for both the future worlds compared to the historical period. There is also an increase in the runoff (Fig. 2.9 f, i) generated in future scenarios compared to the past. These changes are more remarkable for a more aggressive SSP585 world in comparison to the SSP126 world. The difference in P, ET, and R (Fig. 2.9 j, k, and l respectively) between the two future scenarios are comparable to (often greater than) changes between historical and lower warming SSP126 scenarios. Majority of the landmass face increase in both P and ET (Fig. 2.9). The decrease in precipitation is over 18.5% of land in SSP126 while 19% in SSP585. 11.7% out of 18.5% (predominantly in Amazon, Northeastern Brazil, Southern South Africa, Sahara, and Western half of Australia) also show a decline in ET while the rest 6.8% (mostly pertaining to Central America, parts of Western South America, and the western upstream regions of Amazon) show an increase in ET in SSP126. For SSP585 world, 12.5% (Central America instead of Western Australia in SSP126) out of 19% show a decline in P, and ET value as the remaining 6.5% (the Mediterranean instead of Central America) show an increase in ET with a simultaneous decline in P.

2.4.3.1 Basin-wise changes in discharge and hydro-climatology

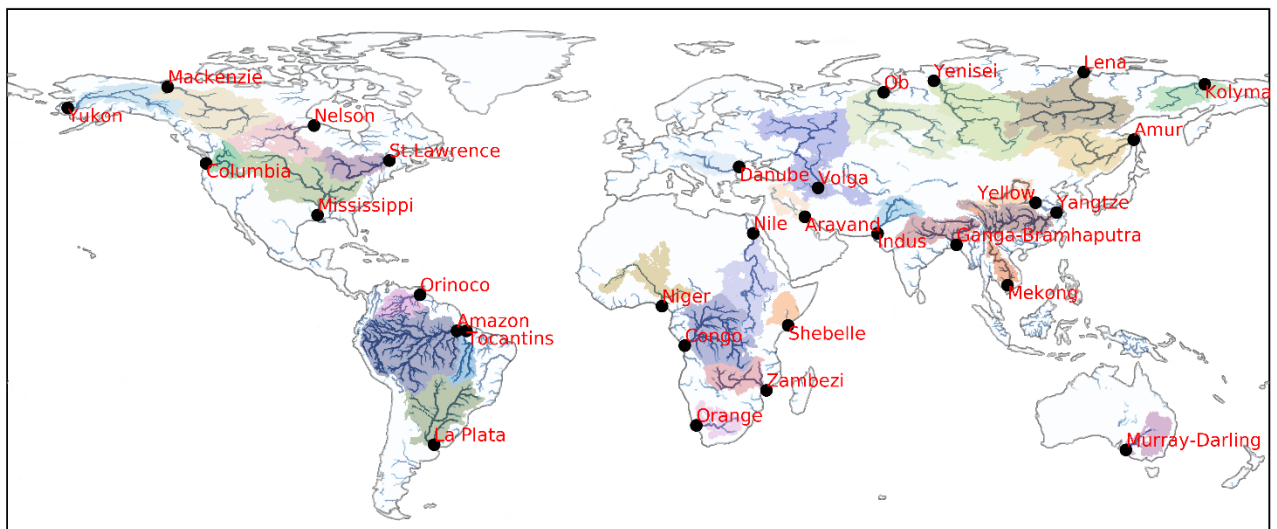


Figure 2.10: The thirty river basins considered in the study are shaded, and their outlets are represented by black circles.

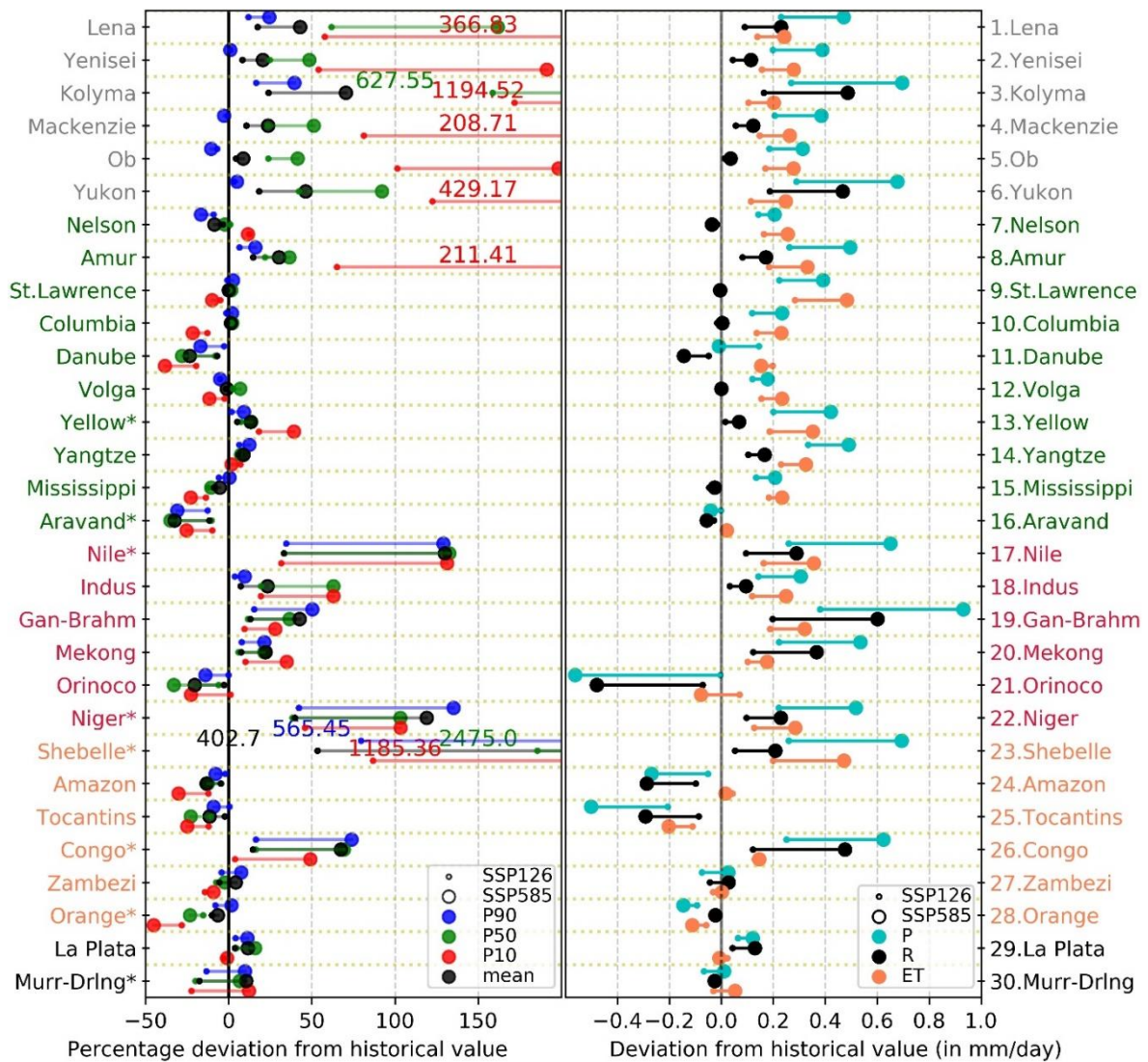


Figure 2.11: Basin-wise changes in discharge and their hydroclimatic background. The left panel shows the corresponding percentage changes with respect to historical values of the mean (black), median (green), lower extreme (red), and higher extreme (blue) freshwater discharge (at the outlet). The right panel shows multi-model mean changes of spatially averaged values of P (cyan), ET (orange), and R (black) (in comparison to their respective historical values) for the 30 major river basins in the high latitude (grey, only northern hemisphere), mid-latitude (green in the northern hemisphere and black in the southern hemisphere) and low latitude (Crimson for north of equator and orange for the south) regions. The small circles represent the changes for SSP126, while the large circles represent a more hostile SSP585 counterfactual future world. The lines join the changes for SSP126 and SSP585 counterfactual worlds. For the basins marked with a "*" for the discharge changes (left), the coefficient of variation for the mean discharge among the different CMIP6 models is greater than 50%, suggesting large variability among models, thus indicating low certainty in the results.

The basin-wise results (Fig. 2.11-left) show the shifts in mean (average), low(P10), moderate(p50), and high(P90) flow for 30 selected basins (Fig. 2.10). The total water flowing into the ocean (considering only these basins and not the island basin Volga) increases by 3.36 % and 10.44% for SSP126 and SSP585, respectively.

The basins in the high latitude region (Fig. 2.11-left) like Lena, Yenisei, Kolyma, Mackenzie, Ob, Yukon, and mid-latitude basin Amur show a tremendous increase in low flows and an increase in mean flow combined with a smaller increase or even decrease (Mackenzie and Ob) in value in comparison to the historical period. Notably, the median values show smaller changes compared to the mean for these cold basins. On the other hand, mid-latitude rivers in both northern (St. Lawrence, Columbia, Volga, Yellow, Yangtze, and Mississippi) and southern (La Plata) hemispheres along with African low latitude basins Orange and Zambezi show smaller changes in comparison to the high latitude basins in mean, median, and lower extreme value of discharge. The low latitude basins in the northern hemisphere (except the Orinoco) and Shebelle and Congo in the southern hemisphere face an increase in discharge (for P10, mean, median, and P90) for SSP126, which intensifies with increased warming and deteriorating mitigation in SSP585 world. The South American basins like Amazon and Tocantins would dry, with a decline in mean, median, and lower extreme value of discharge, heightening with additional warming in the SSP585 world.

The changes with respect to historical values in mean, median, and both the extremes of precipitation(P), evapotranspiration (ET), and runoff (R) generally get amplified with warming from SSP1-RCP2.6 world to SSP5-RCP8.5 world. Most of the basins in the Northern Hemisphere (except Danube, Aravand, and the Orinoco) together with Shebelle and Congo in the southern hemisphere experience a relative increase in both precipitation(P) and evapotranspiration (ET), while a decline in values can be observed for both ET and P for Orange and Tocantins while only for P for Amazon and Orinoco (Fig. 2.11-right). These changes escalate with aggravating conditions of mitigation and warming. Among the basins with increasing P, the ET increase is lower for most basins, except Nelson, St. Lawrence, Volga, and Mississippi.

Murray-Darling shows a non-intensification in P and ET changes with a decrease in relative values in SSP126 while an increase in SSP585, with a decreased runoff(R) in both scenarios. The Danube, Aravand and Orinoco, Amazon, and the Zambezi also show some degree of non-intensification, with either weakening of change in SSP585 or with opposite sign of change in either ET (Orinoco, Amazon) or both ET and P (Danube, Aravand, Zambezi). Nelson, St. Lawrence, Colombia, Danube, and the Volga do not show significant changes in mean R, although large changes can be seen in both P and ET.

2.4.4 Changes in Discharge Attributes: Magnitude and Duration

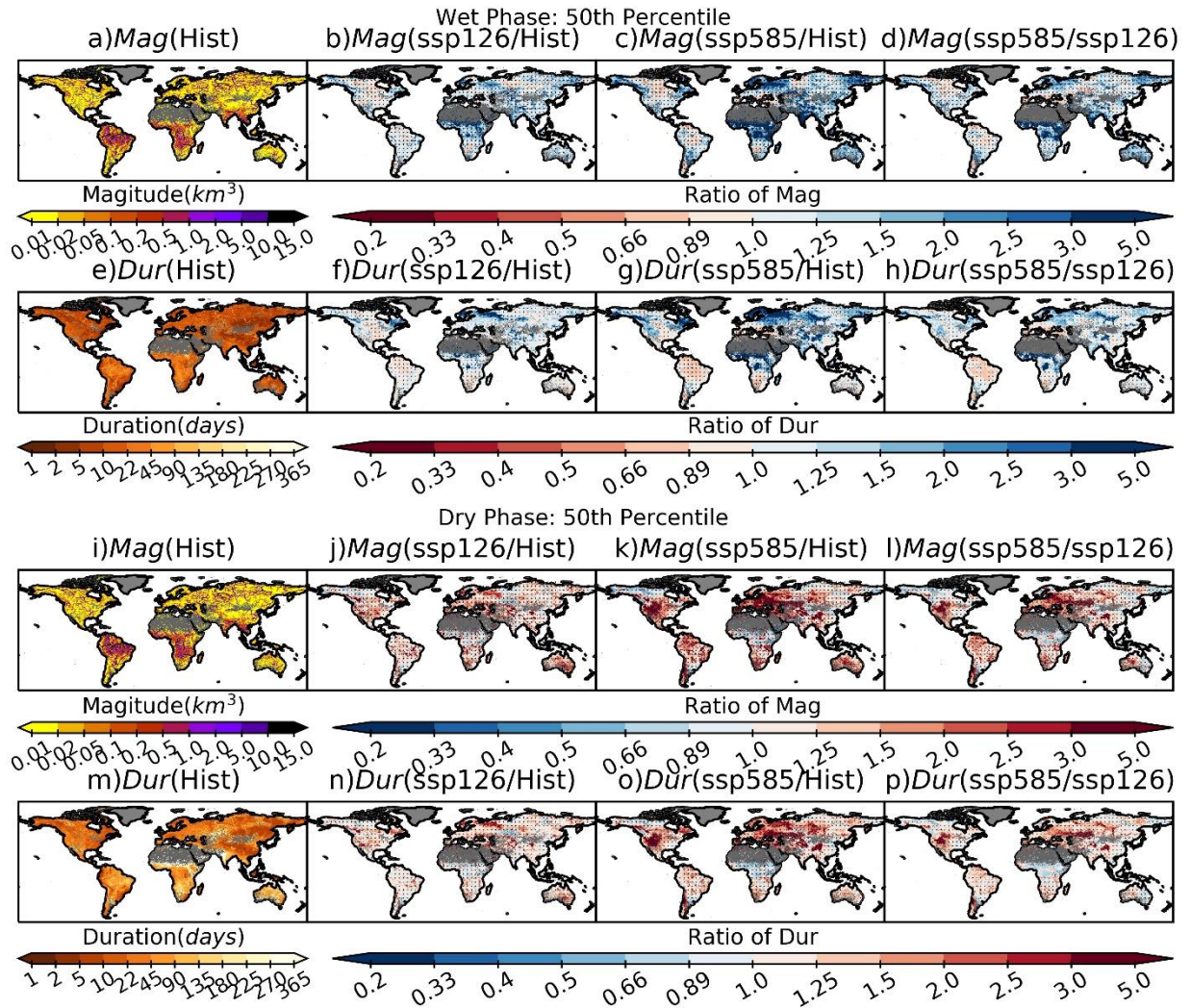


Figure 2.12: The wet (a-h) and dry phase(i-p) values of 50th percentile of Magnitude (*Mag*) and Duration (*Dur*) for historical values (1st column) and changes in their values in the future in comparison to corresponding historical values (2nd and 3rd column) and the difference between the two future scenarios (4th column). The dots show the significance of the change in terms of the model agreement.

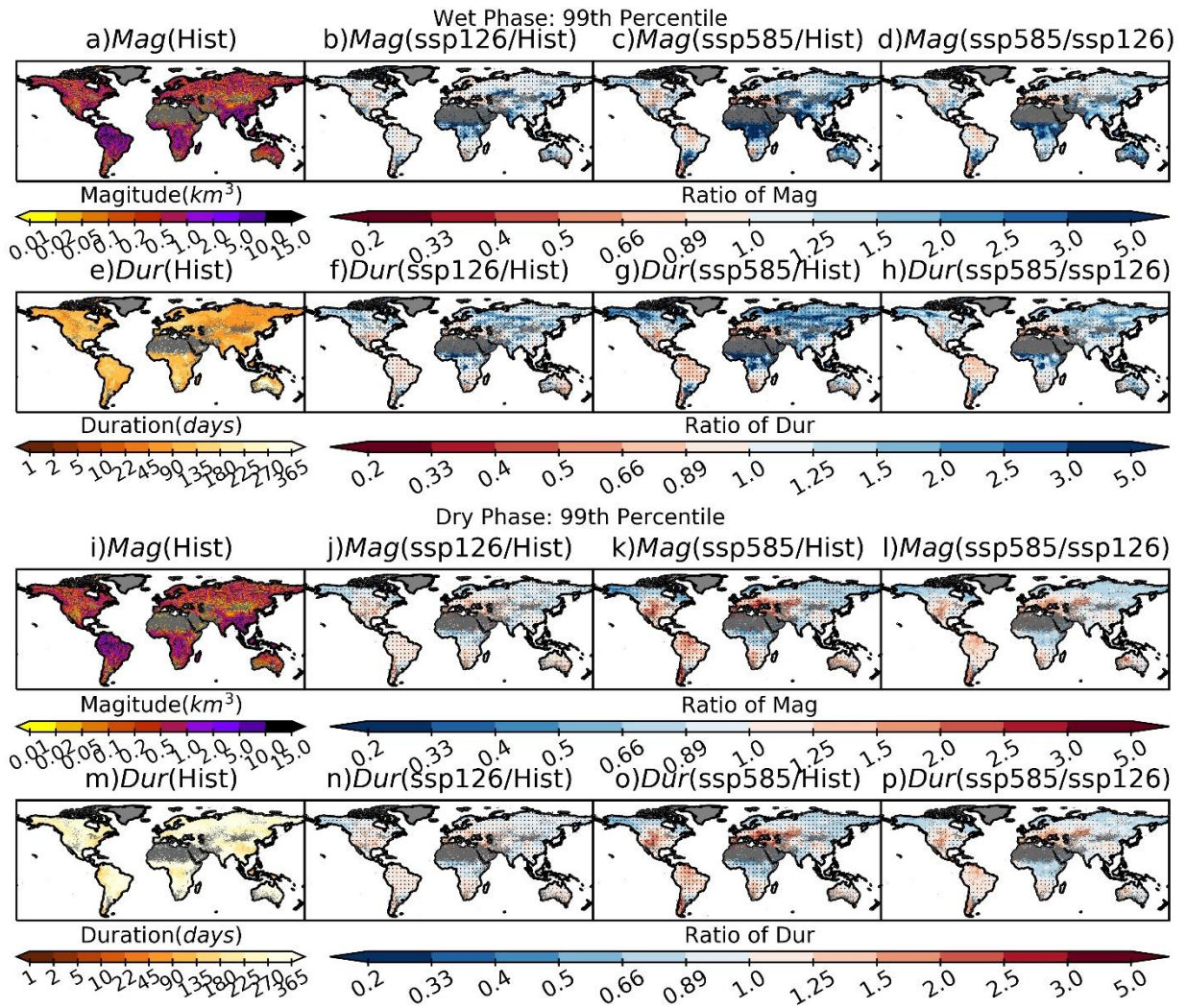


Figure 2.13: Same as S6 but for 99th percentile values The dry phase Magnitude (Mag) and Duration (Dur) for historical values (1st column) and changes in their values in the future in comparison to corresponding historical values (2nd and 3rd column)) is shown in the above figure.

In the case of moderate events, most of the world shows an increase in dry and wet phase magnitude and duration (Fig. 2.12). However, parts of Alaska, Southern South America, and the Sahel show a decline in the dry phase, while Eastern North America, Amazon, Southern Africa, Eastern Asia, and parts of Northern Asia show a decrease in wet phase for both magnitude and duration. Central North America, Amazon, the Mediterranean, Southern Africa, Central Asia, Eastern Asia, and Australia show an increase in extreme dry magnitude and duration (Fig. 2.12) in both future scenarios. With additional warming, the dryness in these regions tends to increase. Similarly, for the wet phase, Alaska, Southern South America, central Africa, Southern Asia, Tibet, Northern Asia, and Australia show an increase in extreme magnitude and duration (Fig. 2.13) in SSP126, which amplifies in SSP585. This result is consistent with previous studies ^{26,94} in most regions. The magnitude and duration boost in a higher

warming scenario in moderate events for about 55% of regions in the dry phase and 60% of regions in the wet phase (Table 2.2). In the case of extreme events, these values are even more prominent, with greater than 70% of the region for magnitude and duration in both dry and wet phases. These results align with the DDWW paradigm for moderate events and more propounding for extreme events with an intensification of scenarios from SSP126 to SSP585. Only a small proportion of land area shows non-intensification or opposite tendencies (Table 2.2).

Table 2.2: Global values for moderate and extreme events

Event	Moderate Events (p50)				Extreme Events(p99)			
Phase	Wet Phase		Dry Phase		Wet Phase		Dry Phase	
Attributes	Mag	Dur	Mag	Dur	Mag	Dur	Mag	Dur
Global Mean (hist/hist)	1.00	1.00	1.00	1.00	1.00	1.00	1.00	1.00
Global Mean (SSP126/hist)	17.42	3.64	1.40	1.22	1.42	1.39	1.02	1.02
Global Mean (SSP585/hist)	172.35	9.73	2.01	1.56	3.38	2.20	1.09	1.07
% area with increasing value in SSP126 compared to historical period	71.32	61.80	65.91	64.89	69.87	68.97	45.51	45.64
% area with decreasing value in SSP126	28.68	38.20	34.09	35.11	30.13	31.03	54.49	54.36
% area with increasing value in SSP585	77.12	66.44	68.37	69.56	76.34	71.61	46.51	45.58
% area with decreasing value in SSP585	22.88	33.56	31.63	30.44	23.66	28.39	53.49	54.42
% area with opposite signs in SSP126 and SSP585	20.94	21.47	22.71	22.72	17.82	12.41	13.95	16.49
% area with decreasing intensity	19.49	18.15	21.43	21.70	11.62	11.30	11.95	12.85
% area with increasing intensity	59.57	60.38	55.86	55.58	70.56	76.29	74.10	70.66

2.4.5 Special case for Nile and Niger

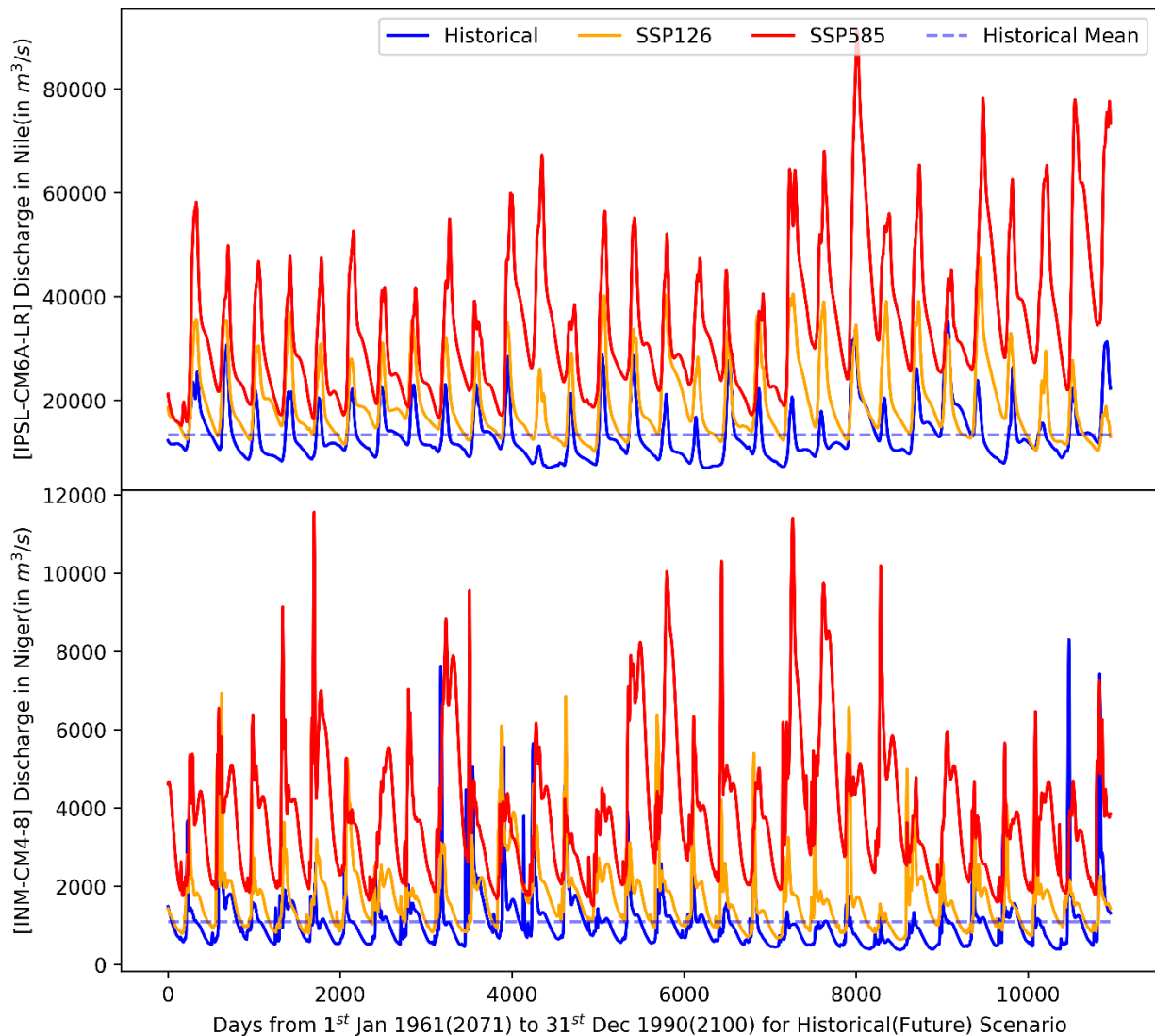


Figure 2.14: The discharge time series for a 30year reference period for the Nile (top) and Niger (bottom)

Under the SSP585 scenario, for Nile in IPSL-CM6A-LR and Niger in INM-CM4-8, the minimum discharge is larger than the historical value, leading to just one large wet event with no dry event at all. Such cases have not been treated differently, and instead, such events demonstrate extreme asymmetric behavior in dry and wet phases in those regions.

2.4.6 Asymmetry in dry-wet shifts

Globally, magnitude shifts are more prominent for the wet phase than for the dry phase (Fig. 2.15), while the shifts in duration are more substantial for the dry phase in both the future worlds for

extreme and moderate events. Such trends in asymmetry in dry and wet shifts get intensified with increased radiative forcing in most regions. For instance, Central North America, South-Western Europe, and the middle east, eastern Canada and Northern Asia show intensification in magnitude shifts from SSP126 to SSP585 for moderate events. A conflicting inclination of asymmetry can also be noticed in regions like Western South America for magnitude shifts and North-Eastern Europe for duration shifts in moderate events.

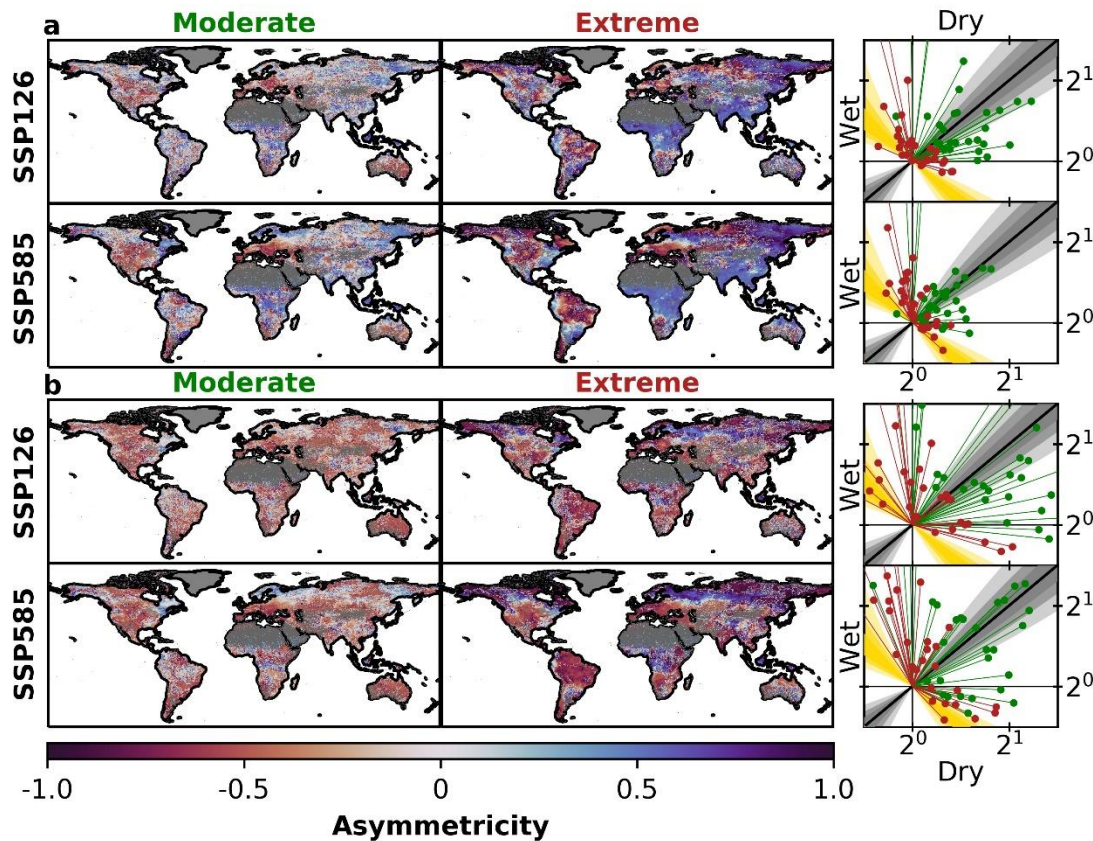


Figure 2.15: Asymmetry in wet-dry shifts. The figure enunciates the asymmetric nature of shifts in magnitude (a) and duration (b) for the wet phase against the dry phase, for moderate (50th percentile) and extreme events (99th percentile), in SSP126 and SSP585 future scenarios. Asymmetry is calculated as the normalized angle formed at the origin between the 1:1 line and the line joining the origin and a point on a plot with wet shift on the x-axis and dry shift on the y-axis. The scatter plots show the ratio of SSP126 (top) and SSP585 (bottom) scenarios to the historical period for moderate (green) and extreme events (red) with dry phase in abscissa and wet phase in ordinate, for magnitude (a) and duration (b). The basin information of these scatter plots is provided in Fig. 2.16.

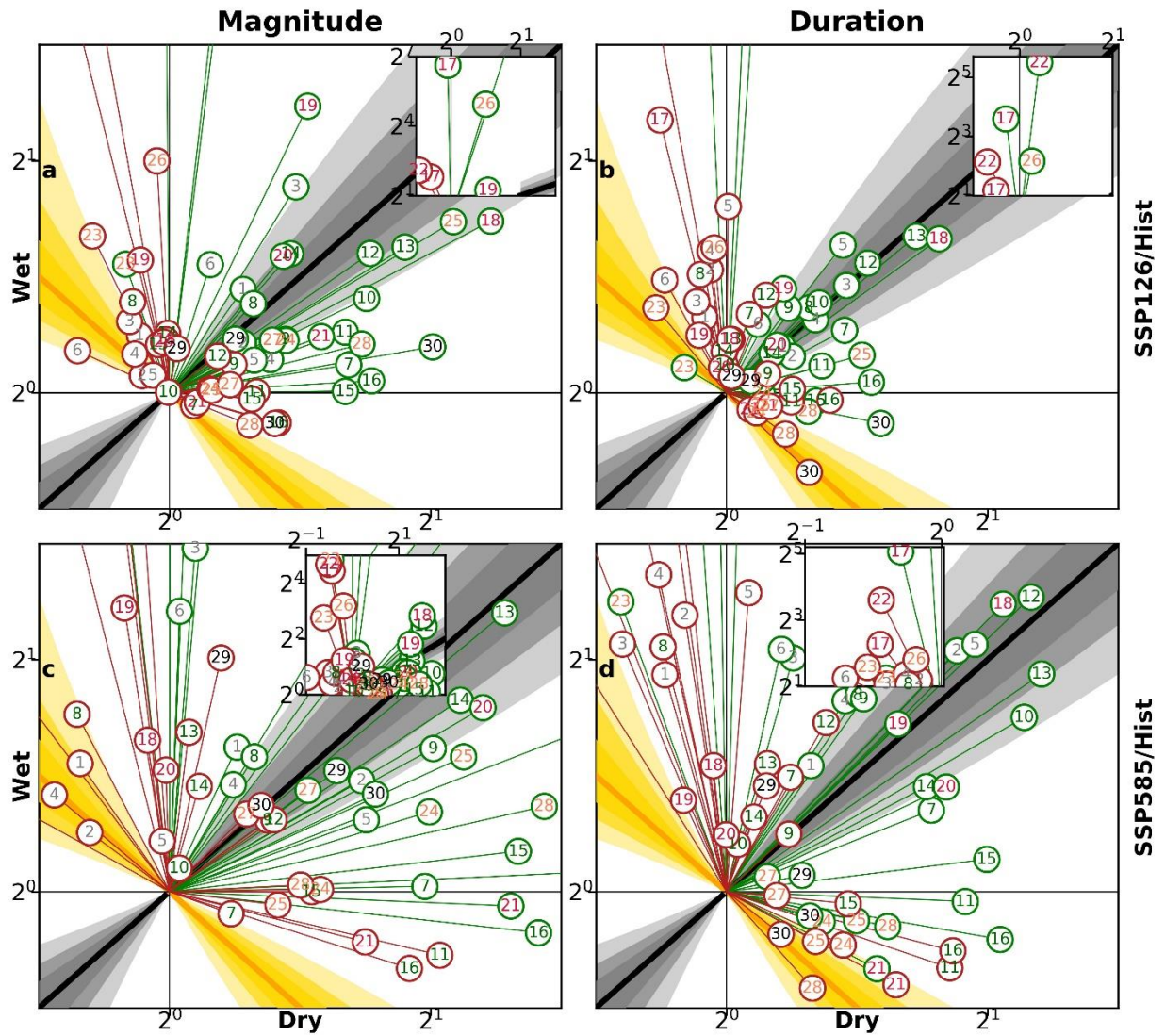


Figure 2.16: Basin-wise dry phase changes against wet. The figure depicts the dry phase changes against wet phase for moderate(green) and extreme(red) values of magnitude (a and c) and duration (b and d) in SSP126(a and b) and SSP585(c and d) as a ratio to historical values. The grey (yellow) background shows symmetry (asymmetry) of changes, the black(orange) solid line is the 1:1 (-1:1) line, and darker shade means higher symmetry (asymmetry). The numbers in the circles represent basins: 1.Lena, 2.Yenisei, 3.Kolyma, 4.Mackenzie, 5.Ob, 6.Yukon, 7.Nelson, 8.Amur, 9.St.Lawrence, 10.Columbia, 11.Danube, 12.Volga, 13.Yellow, 14.Yangtze, 15.Mississippi, 16.Aravand, 17.Nile, 18.Indus, 19.Ganga-Brahmaputra, 20.Mekong, 21.Orinoco, 22.Niger, 23.Shebelle, 24.Amazon, 25.Tocantins, 26.Congo, 27.Zambezi, 28.Orange, 29.La Plata, 30.Murray-Darling. The color scheme for the basin number is the same as in Fig. 2.11

Asymmetric shifts for both magnitude and duration are more prominent for extreme events (Fig. 2.15b) than for moderate events (Fig. 2.15a). The shifts in extreme events show an aggravation in

SSP585 compared to SSP126. For instance, Alaska, Central North America, Eastern Canada, Amazon, Northeastern Brazil, West Coast of South America, Central Europe, South-Western Europe, and the Middle East and Northern Asia for magnitude shifts shows amplification from SSP126 to SSP585. Furthermore, asymmetry is greater than 0.5 and less than -0.5 for most of the land area in the case of extreme events for both magnitude (>60%) and duration (>70%) for both the future worlds. In other words, the decline(increment) in magnitude and duration of the dry phase is accompanied by an increment(decrement) in the wet phase in these regions.

No basin shows a decline in both wet and dry phases compared to historical values for magnitude and duration (Fig. 2.15 and Fig. 2.16). For moderate events (Fig. 2.15), out of 30 basins, 28 and 27 basins for magnitude shifts in SSP126 and 585 respectively, and 23 and 20 basins, mainly comprising the high latitude basins, for magnitude ratios in SSP126 and SSP585 respectively demonstrate an increase in both wet and dry phases. Near-symmetric changes in basins are more common for duration than for magnitude in respective warming worlds. In contrast, in the case of extreme events, an increase in dry phase value is complemented with a decrease in wet phase value and vice-versa, indicating a large asymmetric behavior. Such a pattern can be seen for most basins in all four popsicle plots in Fig. 2.15, especially for high latitude basins (Fig. 2.16). This result aligns with the global asymmetry of extreme events, where values are either greater than 0.5 or less than -0.5 for most regions for both magnitude and duration. Certain basins like Yellow and Indus show a high degree of wet-dry symmetry (Fig. 2.16).

2.4.7 Heterogeneity in magnitude-duration shifts

Homogeneity in magnitude-duration shifts. For both moderate and extreme values, the changes in magnitude and duration are relatively more analogous for the dry phase (Fig. 2.17a) than the wet phase (Fig. 2.17b). However, such Magnitude-Duration homogeneity is more coherent for extreme values (P99), especially for the dry phase (Fig. 2.17c). This result is consistent for both the future worlds; however, the heterogeneity increases with additional warming from SSP126 to SSP585. In both phases, the changes for moderate and extreme values are more prominent for magnitude than duration. However, for the wet extremes (P99), a significant proportion of the area shows a substantial increase in duration compared to magnitude. Such changes in the wet phase can be seen in the high latitude regions of the Northern Hemisphere (Fig. 2.17d, Fig.S3). Intensification for such anomaly can be seen in higher warming scenarios. Further, the increase in both magnitude and duration is generally more prominent for the moderate state (Fig S10) than for the extreme state (Fig 4c and 4d), especially in the wet phase. The DDWW behavior is also evident for most basins for both extremes (Fig. 2.17c and 4d) and moderate events (Fig. 2.17). However, certain basins like Indus (#18) and Murray-Darling

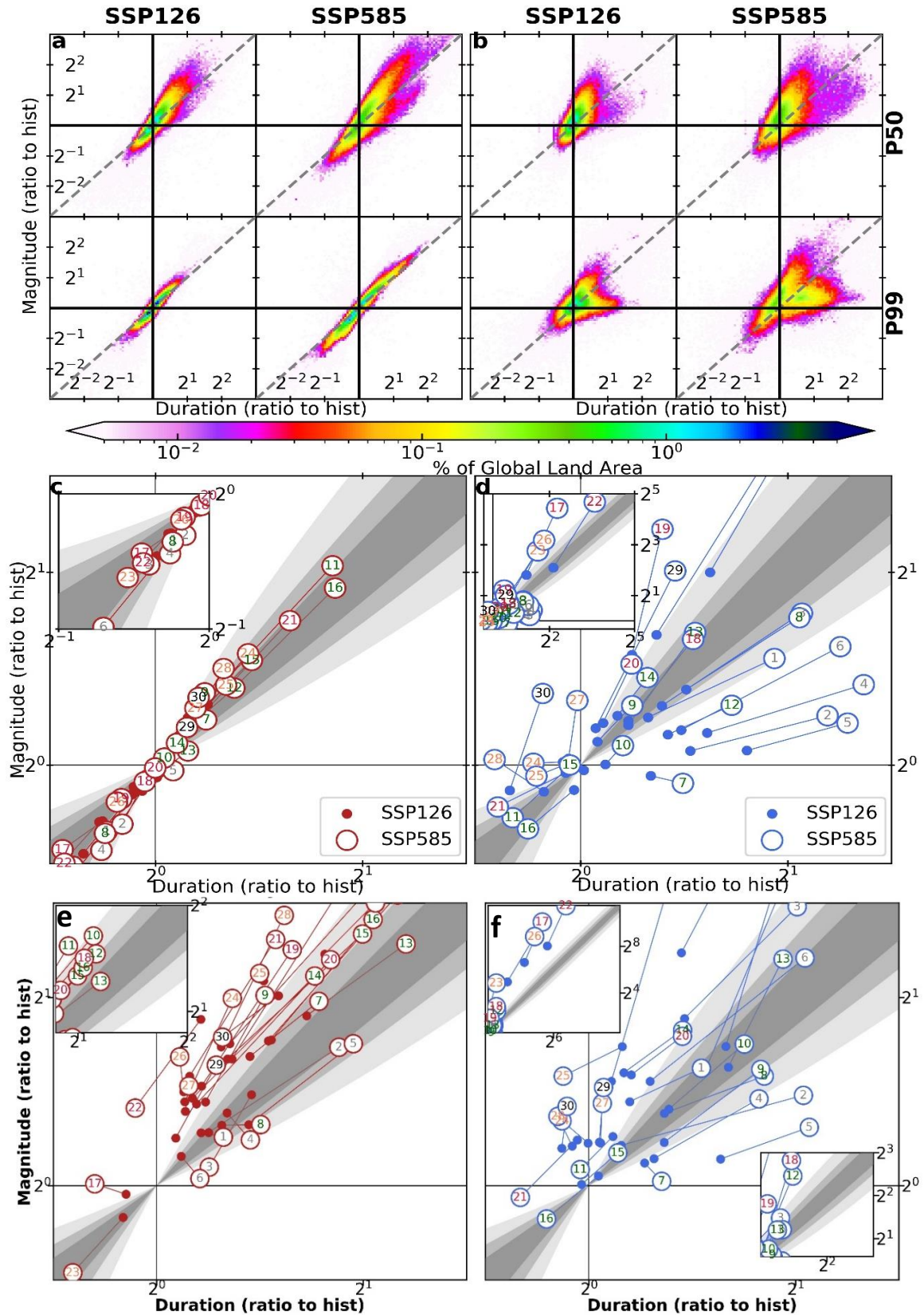


Figure 2.17: Magnitude-duration homogeneity. The figure illustrates the density plot of magnitude shifts against duration for global spatial distribution in dry phase (a) and wet phase (b), and basin-wise distribution for dry (c and e) and wet (d and f) phases in the two future scenarios (SSP126 with small

solid circles and SSP585 with large hollow circles in panels c, e and d, f respectively) for P99 (c and d) and P50 (e and f). The numbers inside the circle represent the river basin: 1.Lena, 2.Yenisei, 3.Kolyma, 4.Mackenzie, 5.Ob, 6. Yukon, 7.Nelson, 8.Amur, 9.St.Lawrence, 10.Columbia, 11.Danube, 12.Volga, 13.Yellow, 14.Yangtze, 15.Mississippi, 16.Aravand, 17.Nile, 18.Indus, 19.Ganga-Brahmaputra, 20.Mekong, 21.Orinoco, 22.Niger, 23.Shebelle, 24.Amazon, 25.Tocantins, 26.Congo, 27.Zambezi, 28.Orange, 29.La Plata, 30.Murray-Darling. The color scheme for the basin number is the same as in Fig. 2.11.

(#30) for extreme events in the dry phase (Fig. 2.17c), and Nelson (#7), Danube (#11), Mississippi (#15), Amazon (#24), and Tocantins (#25) for extreme events in wet phase (Fig. 2.17d) show non-intensification of either magnitude or duration with additional warming. In case of moderate events, such non-intensification can be seen for more basins such as Lena (#1), Kolyma (#3), Mackenzie (#4), Yukon (#6), Niger (#22), Congo (#26), and Murray-Darling (#30) for dry phase (Fig. 2.17 left) and Nelson (#7), Danube (#11), Aravand (#16), Orinoco (#21), and Tocantins (#25) for wet phase (Fig. 2.17 right).

2.4.8 Explanation of the mechanism of changes in discharge

For some mid-latitudinal (#11 Danube, #15 Mississippi, and #16 Aravand) and equatorial (#21 Orinoco, #24 Amazon, #25 Tocantins, and #28 Orange) river basins, the declining outflow is due to the higher increase in ET than P or more diminutive decline ET than P. The decline in moderate, low, and high flow is associated with the moderate and extreme magnitude and duration shifts in dry and wet phases. These drying basins evidently demonstrate an increase in both dry period Magnitude and Duration for both extreme (Fig. 2.17 c and d) and moderate (Fig. 2.17 e and f) events, with extreme values exhibiting fairly homogenous magnitude-duration changes. However, for the moderate events, the mid latitudinal drying basins show a larger magnitude shift than duration, while shifts for equatorial basins are relatively homogenous for the dry phase. Hence for all these drying basins (both mid-latitude and equatorial), an increase in both dry magnitude and duration contributes to the drying of these rivers, with magnitude changes being a greater contributor. These tendencies are valid for both future scenarios. Again, for both futures, the drying of the basins is also due to a decline in duration of wet events for both moderate (Fig. 2.17 e) and extreme values (Fig. 2.17c), even though the magnitude may increase.

All the drying basins show a larger dry shift than wet shift for both magnitude and duration in both futures (Fig. 2.16). For these basins, the low flow declines due to large magnitude and longer duration shifts for extreme events in the dry phase (Fig. 2.17c), thus indicating substantial and elongated future droughts in these basins.

The increase in mean discharge values in most basins is due to increased precipitation, which supersedes the increase in ET. The increase in low flow for all the high latitude basins along with Amur and some equatorial basins (#17 Nile, #18 Indus, #19 Ganges-Brahmaputra, #20 Mekong #22 Niger, #23 Shebelle, and #26 Congo) (Fig. 2.11) is a result of a decline in both magnitude and duration of dry phase extreme values (Fig. 2.17d); expect Ob with an increase in duration. For extreme events in high latitudinal regions, large durational shifts are accompanied by smaller magnitude shifts in the wet phase for both futures (Fig. 2.17d). This results in smaller changes in the high flows. It should be noted that the P90 values of future discharge (fig. 2.11) in some basins like Ob (#5) and Mackenzie (#4) decline, even though the wet extreme magnitude increases (fig. 2.17). This is achieved due to a sizeable heterogenous shift in the extreme wet phase duration compared to magnitude. Magnitude changes alone cannot be considered a reliable indicator of flood events. It must be combined with durational changes to access the rapidity of the change. It should be noted that at the global scale, most of the changes are slightly larger for magnitude compared to duration (Fig. 2.17b), except for the high latitude regions (Fig. 2.12 and 2.13). Additionally, the magnitude obtained within a short timespan has more drastic effects in comparison to the same magnitude achieved over a longer span. Such severity of magnitude changes can give more information about the flashiness of floods and droughts. However, it is not in the scope of this study. Nevertheless, it may be observed that the heterogeneity of changes in magnitude and duration (with higher wet magnitude than duration) for the wet phase being more prominent than the dry phase, indicating more flash-floods than flash-droughts in the future. The mean and moderate flow also increases for these high latitudes and equatorial basins. Most of the wetting basins demonstrate a larger shift in magnitude and duration of the wet phase than the dry phase (Fig. 2.16). However, wetting basins like the Yenisei (#2) and Mackenzie (#4) show a larger positive dry phase shift than wet shifts for both Magnitude and Duration of the moderate event in SSP126. These changes are comparatively symmetric for dry and wet phases. Additionally, some mid-latitudinal basins (Amur, Yellow, Yangtze, and La Plata) get wetter in the future due to increased precipitation. However, the increasing low flow for Yellow cannot be explained as dry period magnitude and duration increase (Fig. 2.17).

Mid-latitude basins Nelson (#7), St. Lawrence (#9), Columbia (#10), and Volga (#12) do not show significant changes in the discharge changes, however, have large shifts in P and ET can be seen in these basins, which tend to balance each other, leading to no net changes in resultant runoff (Fig. 2.11). While Columbia demonstrates small shifts in moderate magnitude and duration values for wet and dry phases, other basins show considerable changes. St. Lawrence (#9), Columbia (#10), and Volga (#12) portray an increase in extreme value of dry magnitude and duration (Fig. 2.17c), resulting in a decline in low flow and hence increasing drought risks. In contrast, Nelson (#7) displays calmer

changes with decreasing high flow, which is due to positive shifts in extreme duration accompanied by declining extreme magnitude. Nelson also demonstrates an unexplainable increase in high-flow, like Yellow. Zambezi and Murray-Darling show some contradicting results for SSP126 and SSP585. Such large non-linearity of changes with warming can be attributed to the non-linearities in P and ET changes (Fig. 2.11).

2.4.9 Symmetric Attribution of Extreme Event Risk to human-induced warming

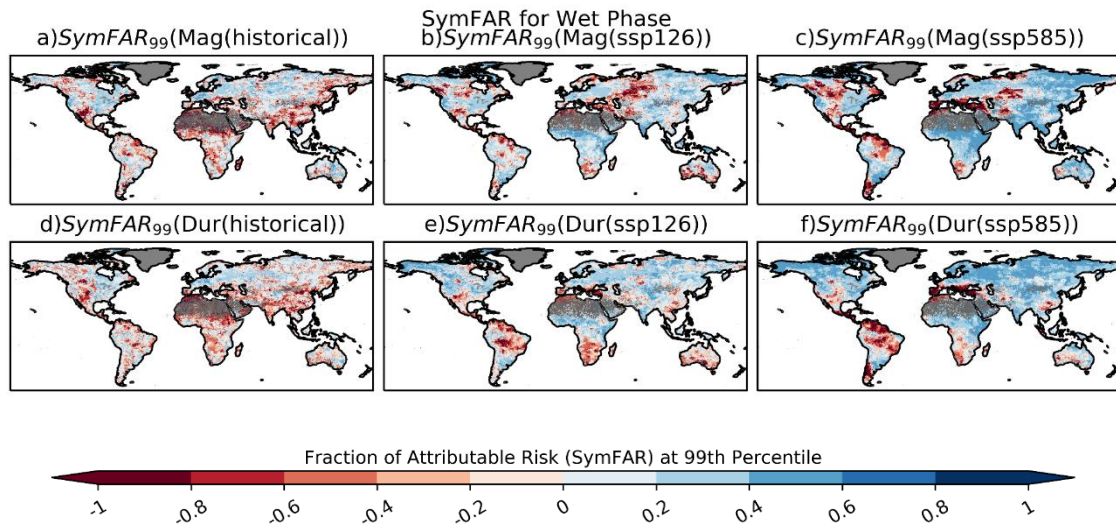


Figure 2.18: Symmetric attribution of both increase and decrease in risk to climate change for wet phase changes in historical (a, d, g), SSP126 (b, e, h), and SSP585 (c, f, i) for discharge attributes

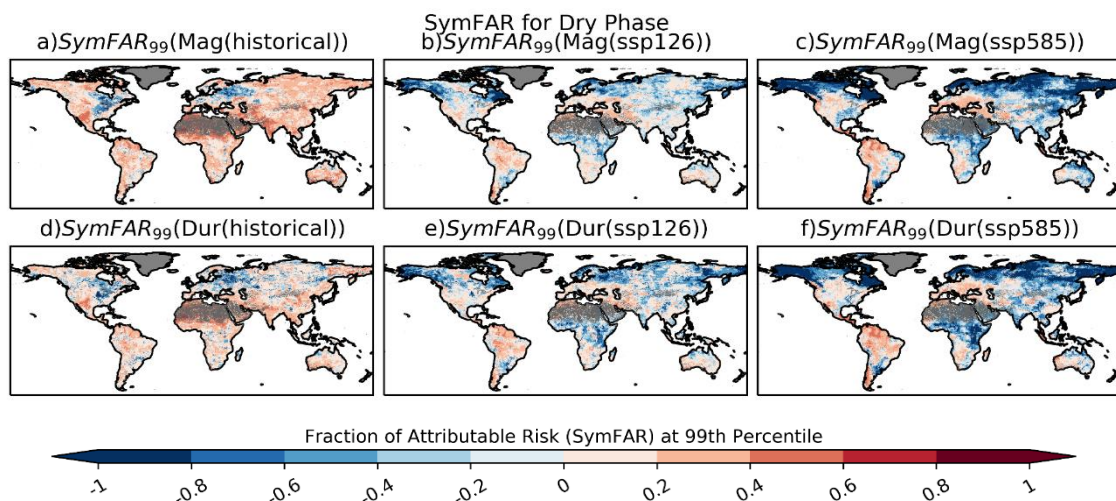


Figure 2.19: Symmetric attribution of both increase and decrease in risk to climate change for dry phase changes in historical (a, d, g), SSP126 (b, e, h), and SSP585 (c, f, i) for discharge attributes.

Human-induced warming (HIW) is responsible for both increasing and decreasing the risk of extreme events as both positive and negative values of SymFAR were discovered for wet (Fig. 2.18) and dry (Fig. 2.19) events. The symmetric fractional attributed risk to HIW shows intensifying attributed risk for wet phase changes in most regions. In contrast, for the dry phase, there is a drastic difference in attributed risk to HIW that can be seen in the future scenarios when compared against the historical scenario, often demonstrating a reversal of risk. Reversal of risk means HIW is causing opposite effects in warmer futures compared to the historical period. For dry events, in most regions, extreme event risk attributed to HIW reverses (particularly in high latitudes) risk for the future scenarios. Reversal of risk can be seen in wet phases in Central Asia and Southern and Eastern Asia. In the historical scenario, tipping points can be seen for risk attributed to HIW for increment and decline in risk of extreme wet and dry events, such as in Europe and Amazon.

2.5 Discussion

With increasing global warming, the global discharge in rivers increases, despite the regional decrease in flow. However, this result does not contradict the previous research^{27,46,80,81,95}. Not only the amount but also the spread of such increasing discharge intensifies. This increase is primarily due to increased precipitation and ET, pointing at the intensification of the terrestrial water cycle in a warmer world, which has been supported by multiple researchers^{11,82,96} in the past. Furthermore, the early melting of ice in the summer would increase in a warmer climate, possibly further increasing snow and glacier-fed river discharge on a seasonal scale. However, this study does not explore such seasonal impacts in this study. The findings of this study align with past studies globally⁸¹ as well as for most basins¹², not only in mean values but also for extreme values of discharge^{27,46}. Even for P, ET, and R⁹⁷, the results agree with past works^{12,27,97}, apart from a few regional discords like precipitation in Amazon¹² and runoff in Niger⁹⁷. The extreme wet^{26,27,98} and dry²⁷ changes can also be deemed consistent with previous research. Most conflicts pertain to the Amazon region. Though some studies show a contradicting increase in discharge in the Amazons^{12,46}, there is a decline in runoff and discharge in others^{27,95,97}. Such conflicts may be due to different data or models, showing the uncertainty of results compared with previous works.

The median value of magnitude and duration increase in both the dry and wet phases (Fig. 2.15) suggests a general increase in intensity and a longer duration of the events compared to the past. This increased median intensity and duration also occur for most of the basins. A longer and more intense dry and wet period would have drastic effects on various aspects of the biota and human life. Agriculture, industrial, and domestic water needs (especially in the dry season) will be primarily affected. Power generation would face drastic impacts due to declining water availability aided with

an increased temperature. The water temperature rise would also adversely affect the riverine ecosystem.

The changes in magnitude and duration for both wet and dry phases are the consequences of climate warming and mostly get aggravated as warming increases and adaptation declines. Results reveal that with the warming world, all changes in discharge attributes are asymmetric to some extent, although, in several regions, changes and intensification in these values with warming. Non-intensification, as well as opposite tendencies, can also be seen in certain areas.

SymFAR reveals a reversal of risk in the extremely dry and wet events that can be attributed to HIW. A similar decline in flood risk with warming was demonstrated in a previous research ²⁶, but the changes were not attributed to HIW in particular. By removing the risk caused by natural variability, SymFAR quantifies the change in risk caused due to HIW. With the symmetric attribution of risk, it was possible not just to quantify the increase in risk but also decrease in risk due to HIW. The paper discusses future discharge changes compared to historical discharge in the mean state and how they differ from the extreme states. Further, it accounts for the reason for such changes for river basins and decomposes those in terms of Magnitude and Duration for separate dry and wet phases. It also discusses implications of Magnitude and Duration changes for both the dry and wet phases. Finally, this study provides a global view of future projections for hydrological water deficit and water excess phases in two counterfactual future worlds compared to the historical period, using indices calculated from discharge.

The study, however, does not discuss the seasonal changes, which might give some new insights. Further intra-basin changes are essential in basins like Ob, where some parts are getting dry while others get wet. As most of the changes in warming can be attributed to human-induced changes, it would be worth knowing the contribution of such impacts on the discharge, its components, and its precursors.

The changes in discharge are measured globally and 30 major large basins, ranging from a 20% decrease to a greater than 100% in some basins. Nevertheless, the influence of climate warming on Earth is not uniform globally. There is considerable spatial heterogeneity in the changes, apart from the high latitude basins. Changes with warming are at times of declining intensity or even opposite directions. These characteristics are not just for discharge but also hydroclimatic variables such as P and ET and indices like magnitude and duration, particularly for extreme events. The changes in discharge are driven by a combination of P and ET that shape the runoff. The dry and wet events will

increase in their intensity for most regions; however, the extreme events might strengthen or weaken with increased warming. Non-intensifications also exist for extreme events.

While most of the changes in discharge for the 30 river basins can be explained by wet and dry changes of Magnitude and Duration, a few changes like low flow in Nelson and Yellow cannot be explained through this methodology. More importantly, increasing high flows and declining low flows can be explained by magnitude-duration changes in wet and dry phases.

2.6 Conclusions

The magnitude and duration of dry and wet events explain the mechanism of changing discharge, particularly for high and low flows. The asymmetry demonstrates magnitude in the wet phase being dominant over the dry phase, while the duration of the dry phase is found to be dominant over the wet phase. Moreover, the magnitude and duration shifts are analogous, particularly for extreme events in the dry phase. Finally, HIW is responsible for the changes in extreme events of wetting and drying, both for increasing and decreasing the risk. Also, a reversal of risk means preparedness for both dry (droughts) and wet (floods) disasters might be needed. Regions that have invested in mitigating droughts in the past might have to invest again for flood mitigation and vice-versa.

An increase in climate extremes in the future is inevitable; however, effective adaptation strategies like rainwater harvesting, appropriate reservoir operations can diminish if not alter the outcomes. Proper policy implementations for adaption and mitigation against extreme events can save the lives and properties of many who are threatened by climate change. As human-induced warming is responsible for increasing the risk of extreme events, particularly in the wet phase, the risk of flood events can diminish by a reduction in greenhouse gas emissions that causes anthropogenic climate warming.

Chapter 3: Changes in River Water Temperature

3.1 Introduction

3.1.1 Importance of water temperature

The water temperature is an essential aspect of the aquatic ecosystem and contaminant transport. With the increased radiative forcing and air temperature, the water temperature is also increasing and is likely to increase further in a warmer future^{44,46}. In addition to the rising water temperature, the dissolved oxygen content would reduce⁹⁹ and lead to the loss of habitat¹⁰⁰ and possible extinction of numerous aquatic species^{25,46,101–103}, causing loss of biodiversity. The rising water temperature would increase the toxicity of chemicals like endosulfan, chlorpyrifos, and phenol⁹⁹ and increase trace metals' solubility and toxicity¹⁰⁴. Rising temperature also causes insecticide toxicity and may be lethal to insects like mayfly larvae¹⁰⁵. Water temperature is also crucial for the industrial sector, especially in thermal power plants, where a heavy demand for cooling water would impact power production.

3.1.2 Factors influencing water temperature.

Water temperature is affected by several factors, natural and anthropogenic. Some of the most crucial factors are listed below:

1. **Shortwave Radiation:** The incoming shortwave radiation is the major contributor to heating the water. It is the driving component, and all other components directly or indirectly get affected by it.
2. **Longwave Radiation:** Downwelling longwave radiation also heats the water.
3. **Water Depth:** The depth of water also plays an important role. Smaller water depths lead to higher water temperature rise.
4. **Air Temperature:** The convective transfer of heat at the water surface depends on the air temperature.
5. **Soil Temperature:** Soil temperature serves as water head temperature. The temperature of the runoff water is almost equal to soil temperature.
6. **Latent Heat:** Heat is lost as latent heat during phase change. Thus, some amount of heat does not contribute to water temperature change
7. **Surface Evaporation:** Surface Pressure, Wind speed, and Humidity affect the evaporation of water from the surface.

8. Reservoirs: Reservoirs act as artificial lakes with large water depths and surface areas. Large surface area leads to large evaporative losses. Also, a significant vertical temperature gradient is formed.
9. Waste Heat: Power plants are the largest contributors to thermal pollution and significantly increase the water temperature. The thermal discharge from these power plants would foster a local increase in water temperature, further increase with the rising temperature^{53,106}.
10. Others: Stream temperature may vary if a hot-spring forms baseflow¹⁰⁷ in certain cases. Effluent for the domestic sector also increases the water temperature. Agriculture has a large water requirement and decreases the depth of water, thereby increasing water temperature indirectly.

3.1.3 Water temperature model: HEAT-LINK

Several models have been developed in the past to simulate the water temperature. These models either follow a statistical approach or a deterministic approach⁷⁸. Although statistical models have their advantages over deterministic models in terms of better accuracy in data-abundant sites, the former cannot be used for ungauged basins with the same feat. Hence parameterization of physical factors serves better than model calibration⁴⁴. In this study, the deterministic model, HEAT-LINK, developed by Tokuda et al. (2019), which considers the seasonal freeze-thaw cycle, was adopted to estimate the water temperature. It should be noted that reservoirs, waste heat, and hot springs have not been incorporated in the HEAT-LINK model.

3.1.4 Gaps in Previous research and scope of the study

The previous studies¹⁰⁸ on water temperature have concentrated on the changes in water temperature for anthropogenically warmed scenarios. However, changes for a naturally forced world have not been addressed. Detection and attribution of changes to human-induced warming remain unaccomplished. Further, it is understandable that the earth's temperature would warm with increased radiative forcing. However, it is important to understand the susceptibility of temperature change to radiative forcing. Such sensitivity of water temperature change to radiative forcing has also not been explored by previous works. Also, the changes in water temperature are often compared with air temperature; however, comparison with soil temperature is still not performed in any of the previous studies on climate change. This study aims to bridge these research gaps. Additionally, the combined effect of water temperature and water flow (discharge) change for anthropogenic and natural worlds are explored. The thermal discharge changes and decomposition of the changes into

flow and temperature components are explored (in appendix). A daily scale temporal analysis for warm days, dry days, and the confluence of warm and dry days are also performed.

3.1.5 Research Questions

1. How do water temperature changes for mean, seasonal variability, and trend differ from that of air temperature and soil temperature in natural and anthropogenically-forced scenarios?
2. How sensitive is the temperature change for water, air, and soil to change in net radiative forcing of the earth?
3. How much is human-induced warming responsible for the change in water temperature, and how is it different from air temperature and soil temperature?
4. How is the frequency of warm days and dry days changing, individually and compounded events changing under different projections of the climate?

3.2 Data

Data from MIROC6 experiments under CMIP6 are used in this study. Table 1 provides the details of input forcing. In the case of hist-nat, where data is available only at monthly scale or daily scale, the pi-control experiment is used to increase the temporal resolution. Pi-control experiments are the control experiments in the GCM simulations under CMIP6.

Table 3.1: Input Climatic and land-surface Data Configuration for historical, natural (Hist-nat and SSP245-nat), pi-control, and future (SSP126, SSP245, SSP370, SSP585) scenarios.

Sl no.	Forcing Variable Name	Units		Temporal scale of CMIP6 Simulations			
		Model requirement	As given in CMIP6 data	Historical	Natural	Pi-control	Future Scenarios
1	Downwelling Short Wave Radiation	W/m ²	W/m ²	3hr	Daily	3hr	3hr
2	Downwelling Long Wave Radiation	W/m ²	W/m ²	3hr	Daily	3hr	3hr
3	Air Temperature	K	K	3hr	Daily	3hr	3hr
4	Soil Temperature	K	K	6hr	Monthly	6hr	6hr
5	Runoff	m ³ /m ² /s	kg/m ² /s	3hr	Monthly	3hr	3hr
6	Wind speed	m/s	m/s	3hr	Daily	3hr	3hr
7	Specific Humidity	kg/kg	kg/kg	3hr	Daily	3hr	3hr
8	Near Surface Pressure	hPa	Pa	3hr	Monthly	3hr	3hr

3.3 Methods

3.3.1 Adjustment of spatial and temporal resolution

The input data is scaled to a resolution of $1^\circ \times 1^\circ$ using bilinear interpolation. The temporal scale has been adjusted for hist-nat and SSP245-nat to that of pi-controlled simulations by using the variability of the pi-controlled simulation.

3.3.2 Water temperature simulation and validation

Data from the seven scenarios (hist-nat, SSP245-nat, historical, SSP126, SSP245, SSP370, and SSP585) force the HEAT-LINK model to produce discharge and water temperature. The model generates the input forcing data at the model-run scale, i.e., $0.25^\circ \times 0.25^\circ$. Water temperature is validated against the observed GEMS station data. The monthly value of water temperature from HEAT-LINK simulation and available GEMS observation are compared. Separate analysis for a thermally polluted basin, Rhine, has also been done.

3.3.3 Seasonal changes in temperature change

The monthly values are computed from the daily-scaled model output, and the mean for MAM, JJA, SON, and DJF triads are considered as spring, summer, autumn, and winter in the northern hemisphere. The mean values for 30 years for each triad are computed for water, air, and soil temperature, and the differences in temperature in the natural and anthropogenic worlds are calculated against their respective historical scenarios.

3.3.4 Sensitivity of temperature change

The change in net radiative forcing is calculated at the top of the atmosphere (TOA) as

$$\text{Net Radiation} = \text{SWR}_{\text{IN}} - (\text{SWR}_{\text{OUT}} + \text{LWR}_{\text{OUT}}) \quad \text{Equation 3-1}$$

where SWR is Downwelling Short Wave Radiation at TOA and LWR is Downwelling Long Wave Radiation at TOA.

The difference in global net radiation with respect to the historical scenario is computed, and change in temperature (water, air, and soil) per unit change in net radiation is defined as the sensitivity of temperature change.

3.3.5 Attribution of extreme temperature to human-induced warming

The changes in water, air temperature, and soil temperature are computed against the naturally forced scenario; hist-nat for the historical period and SSP245-nat for future scenarios. Detrended monthly values of temperature are considered as the population for the 30-year reference period for historical (1961-1990) and future scenarios (2071-2100). SymFAR is calculated for extreme water, air, and soil temperature caused by human-induced warming by calculating the exceedance probabilities, considering the 95th percentile of hist-nat temperatures as the threshold, for the 360 samples in the natural and historical scenarios as in section 2.4.6.

3.3.6 Change in warm days, dry days, and the confluence of warm and dry days.

The dry days are the days for which the discharge falls below historical mean discharge (1961-1990). It is a warm day when the water temperature is higher than the historical mean water temperature (1961-1990). A warm and dry day is when both events occur. For every year, dry days, warm days, and dry and warm days are computed for historical (1961-1990) and future scenarios for natural and anthropogenic worlds.

3.4 Results

3.4.1 Validation

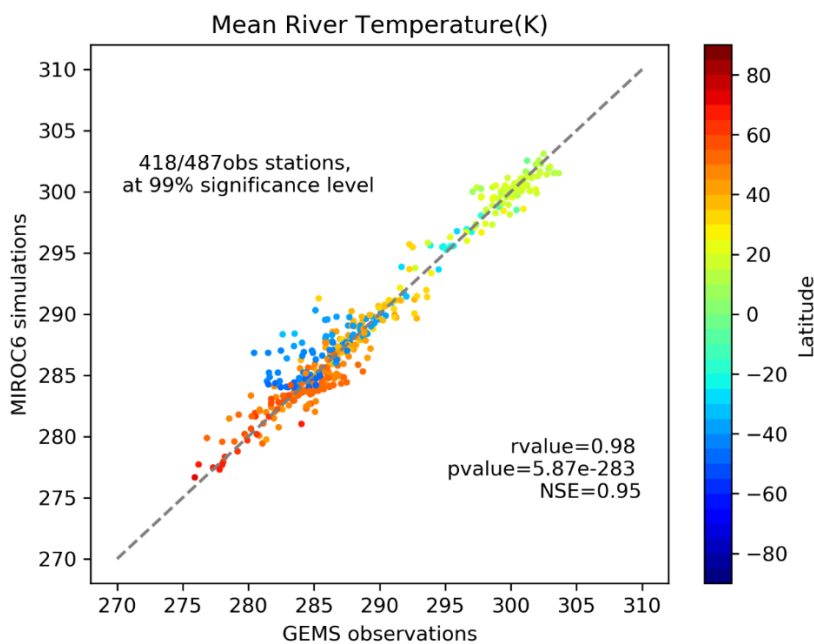


Figure 3.1: Comparison of mean simulated water temperature with MIROC6-forced HEAT-LINK and GEMS observation.

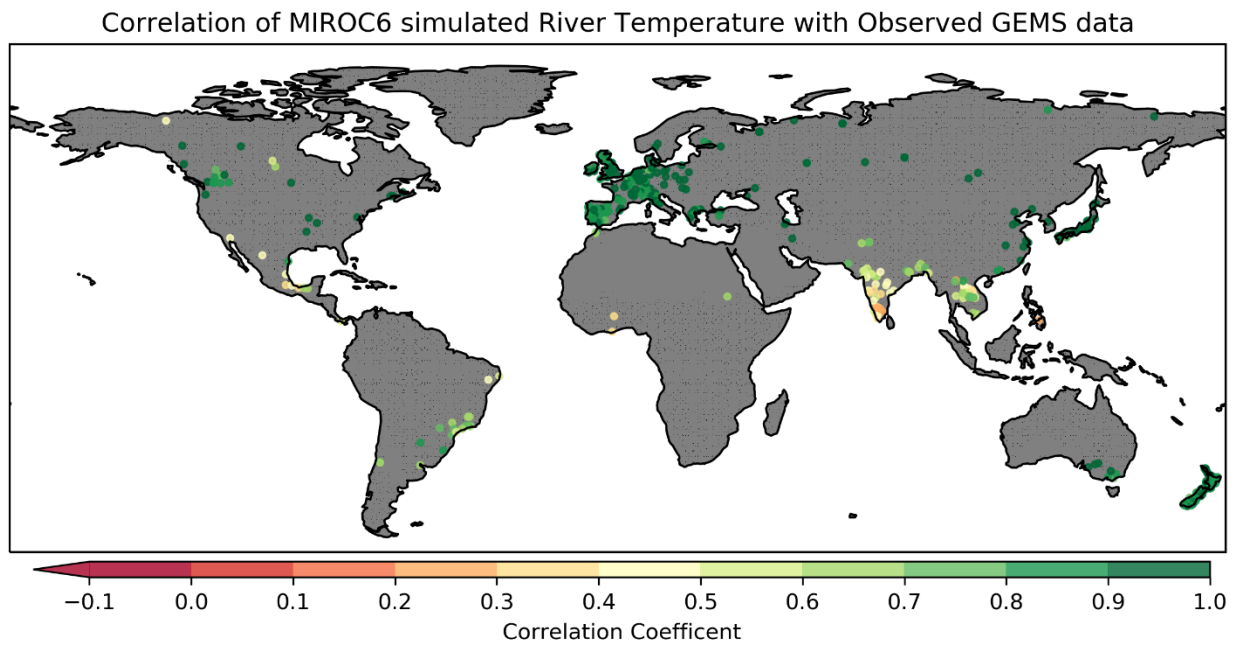


Figure 3.2: Global distribution of correlation for modeled water temperature against GEMS data.

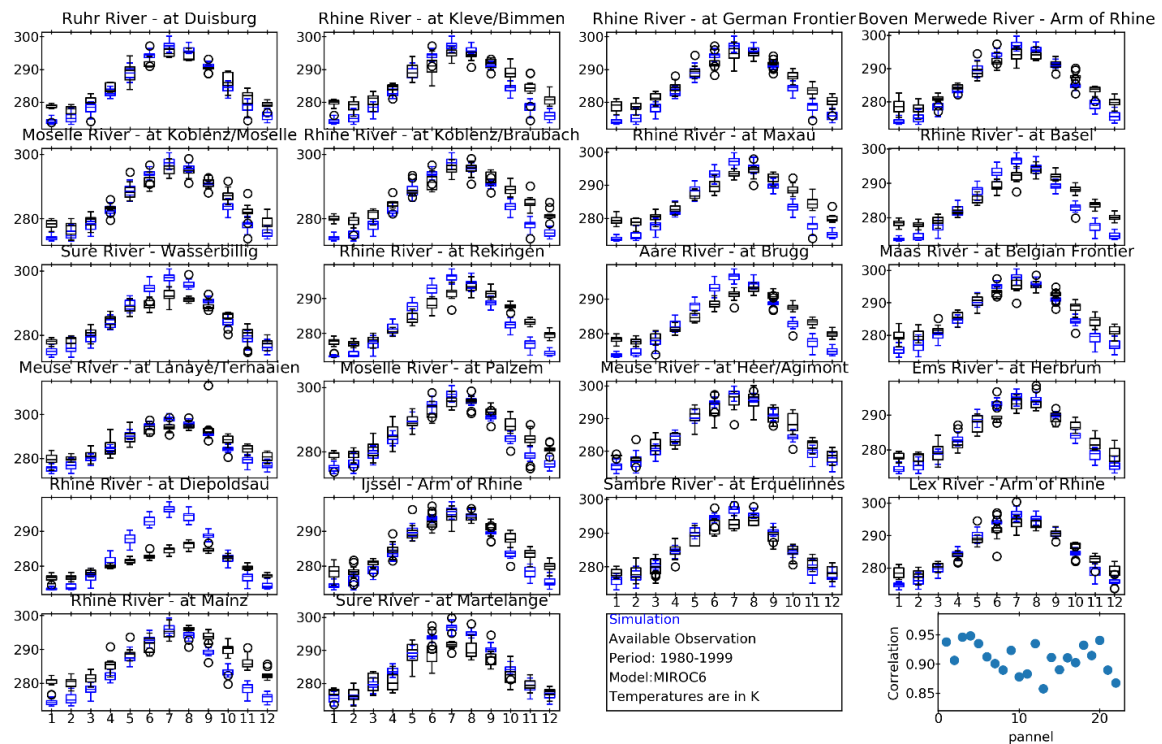


Figure 3.3: Monthly water temperature for model simulation and GEMS observation for the period 1980-1999 for river gauge stations in Rhine River catchment.

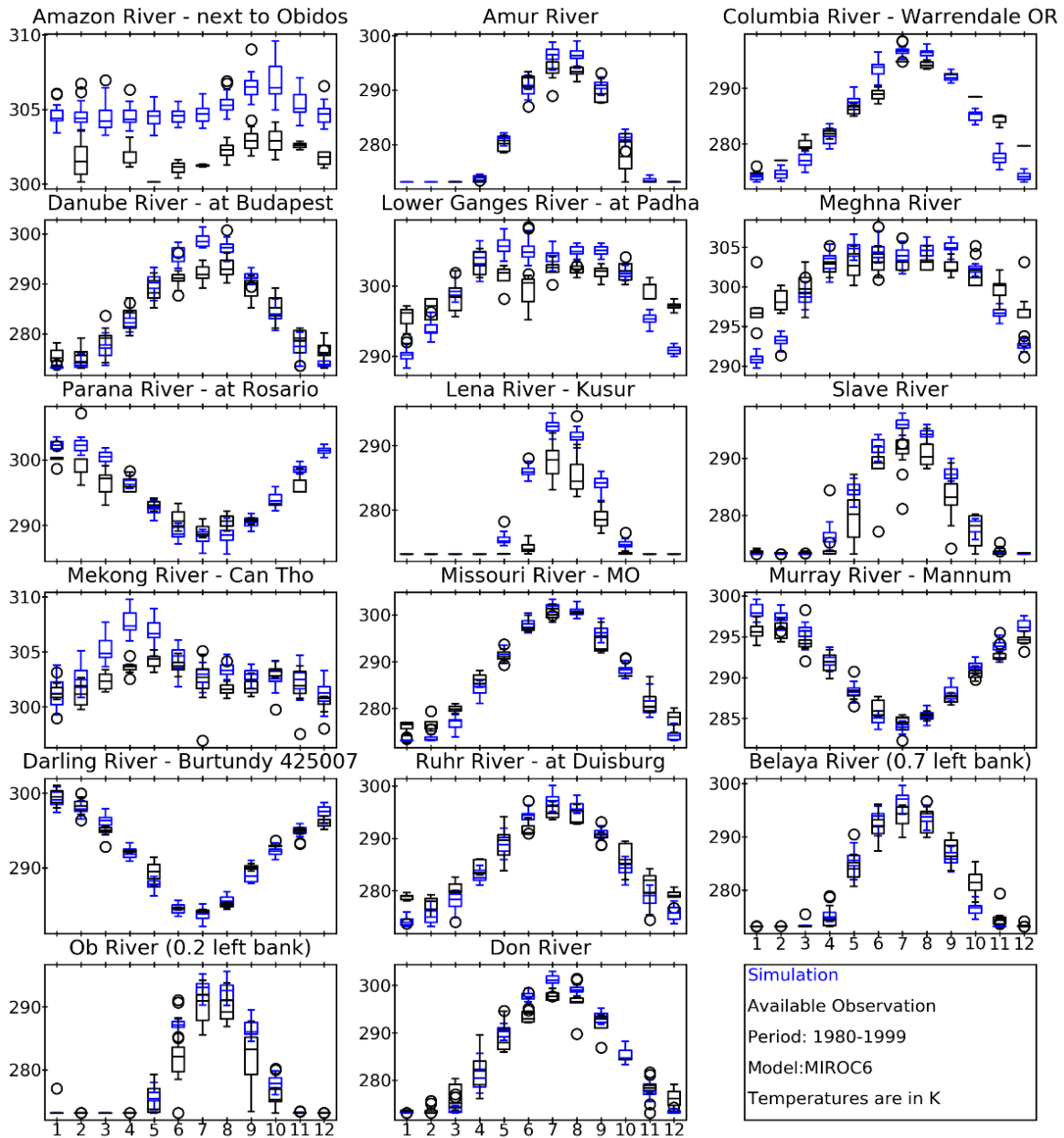


Figure 3.4: Monthly water temperature for model simulation and GEMS observation for the period 1980-1999 for river gauge stations in different rivers in the world. The 12 months are represented on the x-axis and temperature on the y-axis.

The HEAT-LINK model performs well in simulating the mean water temperature when tested against GEMS observed data, with a very NSE value of 0.95 and correlation coefficient of 0.98 (Fig 3.1). 99% statistically significant correlations with observed data are observed for 410 basins out of 487 basins with available data for the period 1980-1999. The model performs the best in the temperate zone, followed by the tropical zone and tundra regions (Fig. 3.2). The model is also tested for the Rhine in particular (Fig. 3.3). Results demonstrate a good correlation between model simulations and

observations and appropriate seasonal variability. The seasonal cycle is also well represented by the model simulation for most basins in both the hemispheres (Fig. 3.4).

3.4.2 Water temperature rise in natural and anthropogenic scenarios

IPCC divided the world into different SREX regions in its 5th assessment report, as shown in figure 3.5. In this chapter, this geopolitical division is used to demonstrate the spatial heterogeneity of the water temperature change.

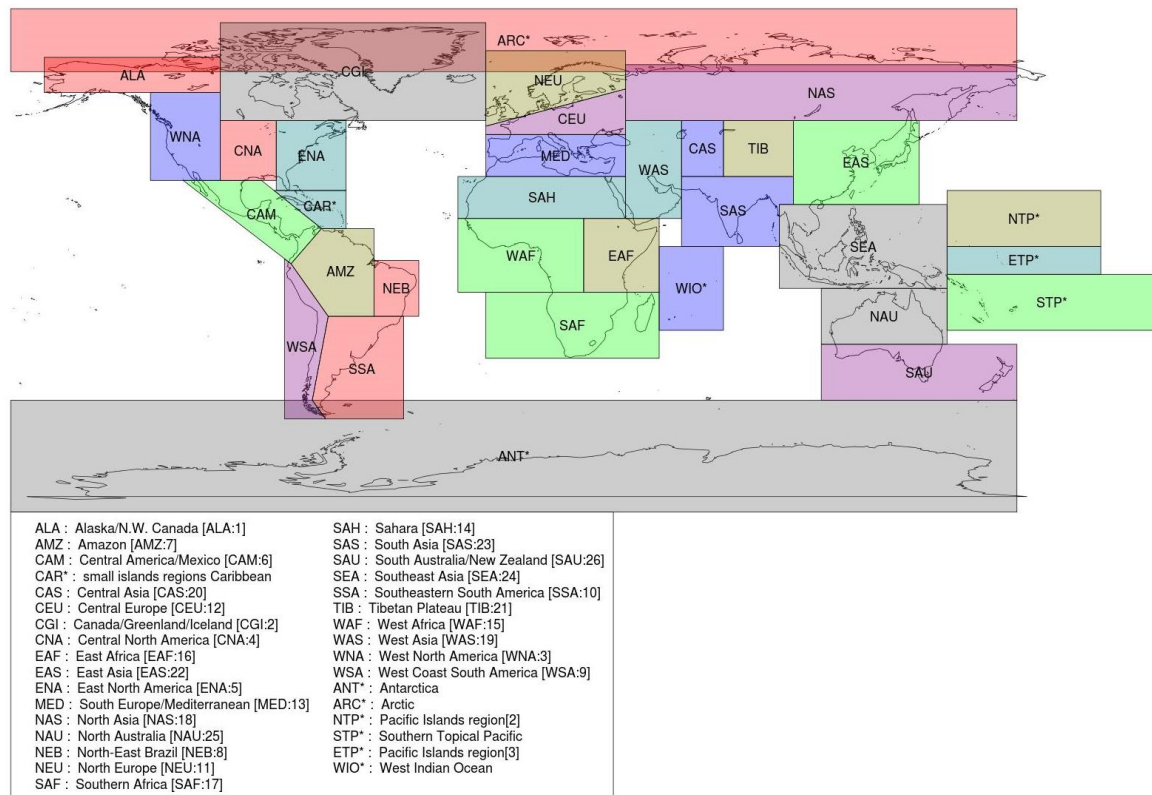


Figure 3.5: Different IPCC SREX regions

In future scenarios with full anthropogenic forcings, globally, the average water temperature increases compared to the historical period, with an increase in radiative forcings (fig 3.6). However, for both historical and future scenarios with natural forcings only, there is almost no change in global mean temperature from the historical scenario. This implies that the impact of anthropogenic forcing will increase extensively in the future, resulting in a global mean freshwater temperature rise of more than 3 °C in SSP585. The changes in temperature are highly heterogeneous. Central Asia, Central Europe, Southern Europe, Mediterranean, Eastern North America, Central North America, and western Asia demonstrate the largest rise in water temperature (>4°C in SSP585) in the future anthropogenic worlds. Additionally, there is a clear intensification of temperature rise with increasing radiative

forcings (fig 3.9). Interestingly, even in the natural setting for historical and future periods, the Caribbean, Central Europe, Southern Europe, Mediterranean, Central and Western North America, and Eastern Asia show a considerable increase in water temperature compared to the historical scenario. Most of these regions coincide with the largest temperature rise in anthropogenically forced futures listed above. Other regions show no change or lower water temperatures compared to the anthropogenically forced historical scenario in both naturally forced scenarios.

In terms of spatial distribution, the heterogeneity of temperature rise generally gets amplified with increased radiative forcings (fig 3.10). Large variabilities can be seen for Central America, Central Asia, Canada, Northern Asia, North-Eastern Brazil, Tibet, and the West Coast of South America. However, it can be observed that Western Africa, the West coast of South America, and Western Asia show very large spatial variabilities of water temperature change in the natural setting than anthropogenically forced worlds.

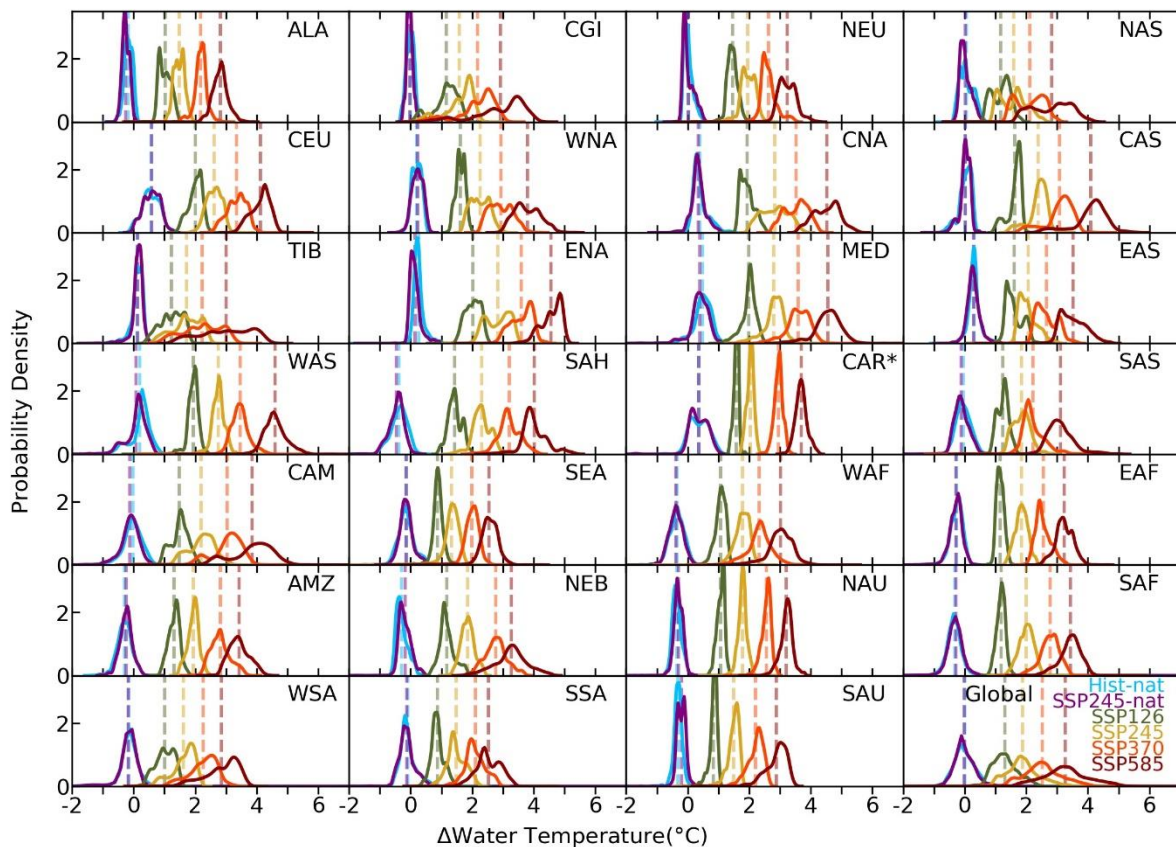


Figure 3.6: Heterogeneity in the distribution of water temperature change with respect to the historical scenario. The vertical lines show the mean value for different SREX regions.

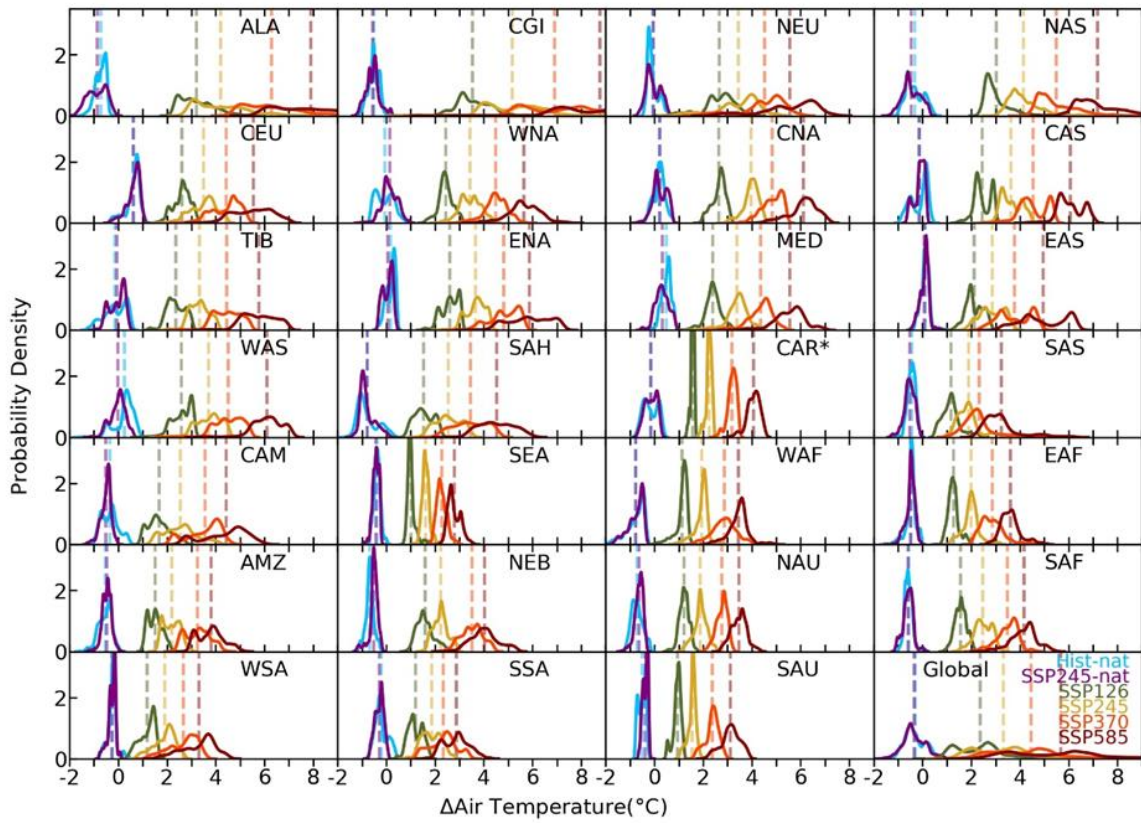


Figure 3.7: Heterogeneity in the distribution of air temperature change with respect to the historical scenario. The vertical lines show the mean value for different SREX regions.

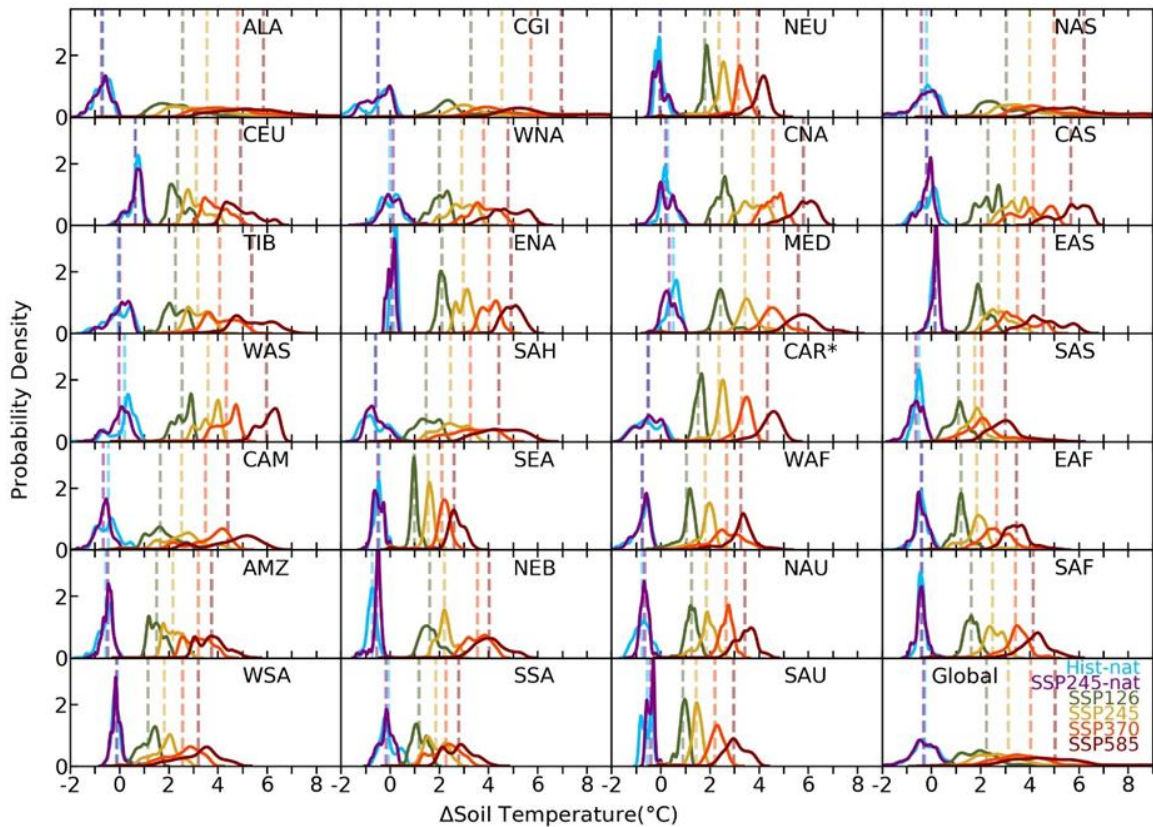


Figure 3.8: Heterogeneity in the distribution of soil temperature change with respect to the historical scenario. The vertical lines show the mean value for different SREX regions.

The air temperature (fig 3.7) demonstrates much more significant changes (fig 3.9) than water temperature. The most extensive changes in air temperature ($>6^{\circ}\text{C}$ in SSP585) can be seen for Alaska, Canada, Central, Northern, and Western Asia, Central North America, and Tibet. For the anthropogenically warmed future scenarios, soil temperature changes (fig 3.8) are more prominent than changes in water temperature but smaller than air temperature shifts (figure 3.9). In other words, the change in the difference between air/soil and water temperature increases in a warmer future. The largest difference in water temperature shifts with air and soil temperature shifts can be seen for high-latitude regions like Alaska, Canada, and Northern Asia. In contrast, in the natural scenario, for both historical and future periods, shifts are more prominent for the water temperature in most regions in the world than air and soil temperature. In contrast, Southern Asia shows a slight decline in

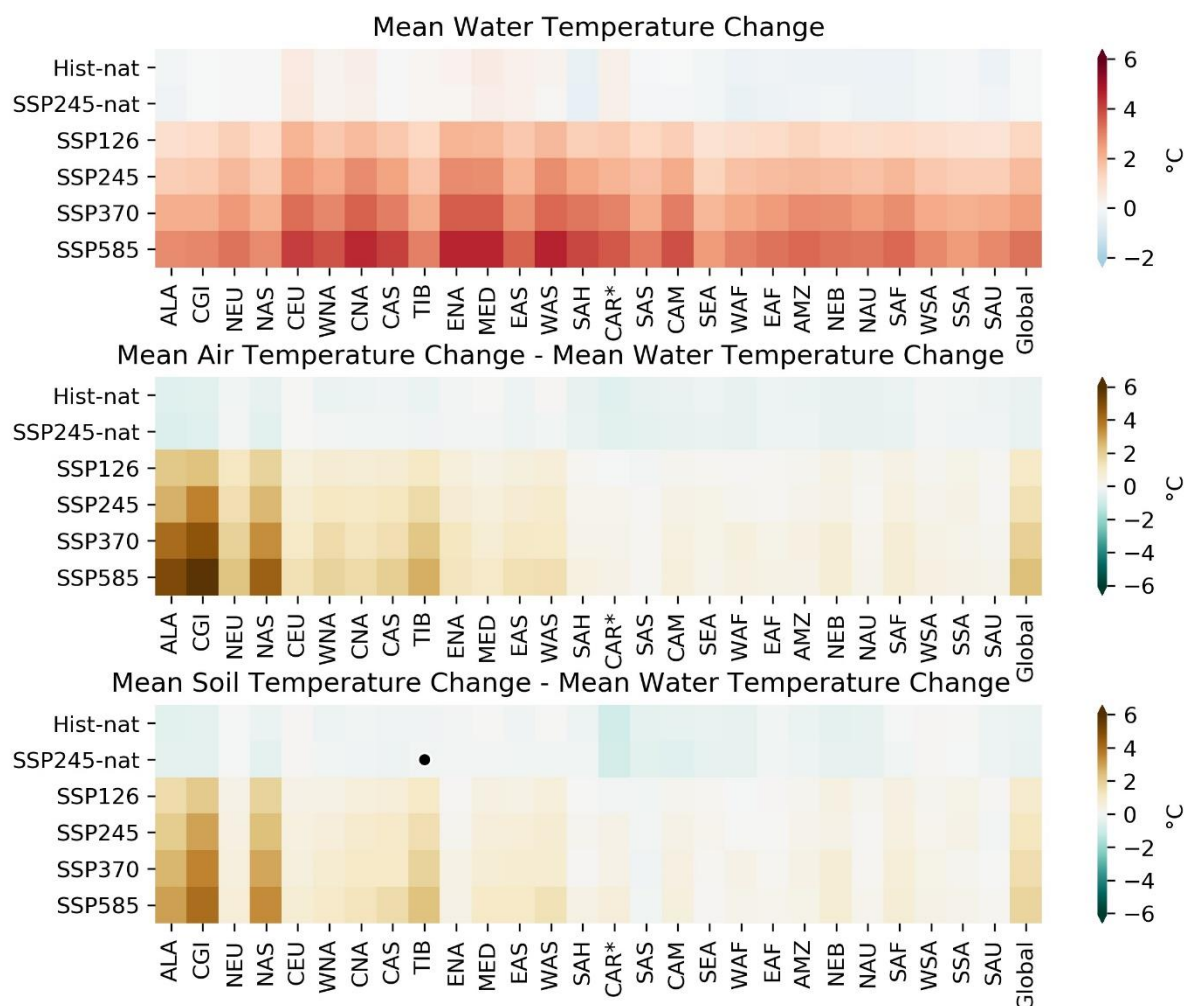


Figure 3.9: Mean changes in water for different SREX regions, compared with shifts in air and soil temperature shifts. Shifts in values for hist-nat, SSP245-nat, SSP126, SSP245, SSP370, and SSP585 are calculated with respect to the historical scenario.

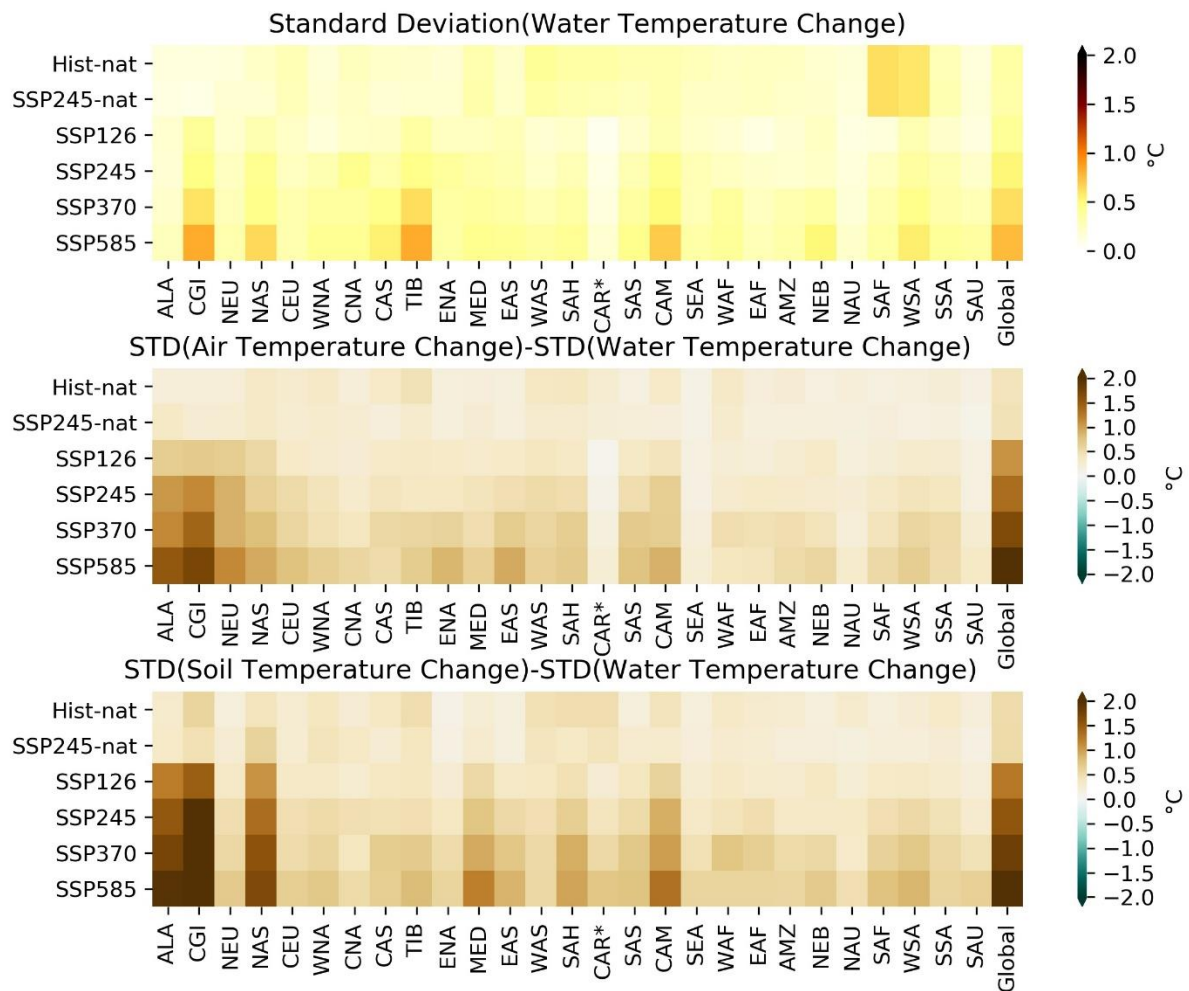


Figure 3.10: Spatial variability of temperature change. The figure illustrates the standard deviation of water temperature changes (top panel) and its comparison with air temperature (middle panel) and soil temperature (lower panel). Shifts in values for hist-nat, SSP245-nat, SSP126, SSP245, SSP370, and SSP585 are calculated with respect to the historical scenario.

The difference between air and water temperature in warmer climates compared to historical values. While for air temperature, there is negligible difference in historical and future scenarios.

However, the spatial variability in both air and soil temperature shifts is higher in natural as well as anthropogenic settings when compared to water temperature changes (figure 3.10).

3.4.2.1 Consistency of water temperature and air temperature

There is a lower limit to the water temperature: the freezing point of water. Thus, in figure 3.11, it can be noticed that the water temperature is higher than the air temperature in cold regions like Alaska

and Tibet. However, the air temperature may be higher or lower than the water temperature in the warmer areas.

Additionally, it can be noted that with increasing warming, the air temperature rises faster than water temperature, suggesting lower sensitivity of water temperature to increased radiative forcing. Such sensitivities have been discussed in detail in section 3.4.5.

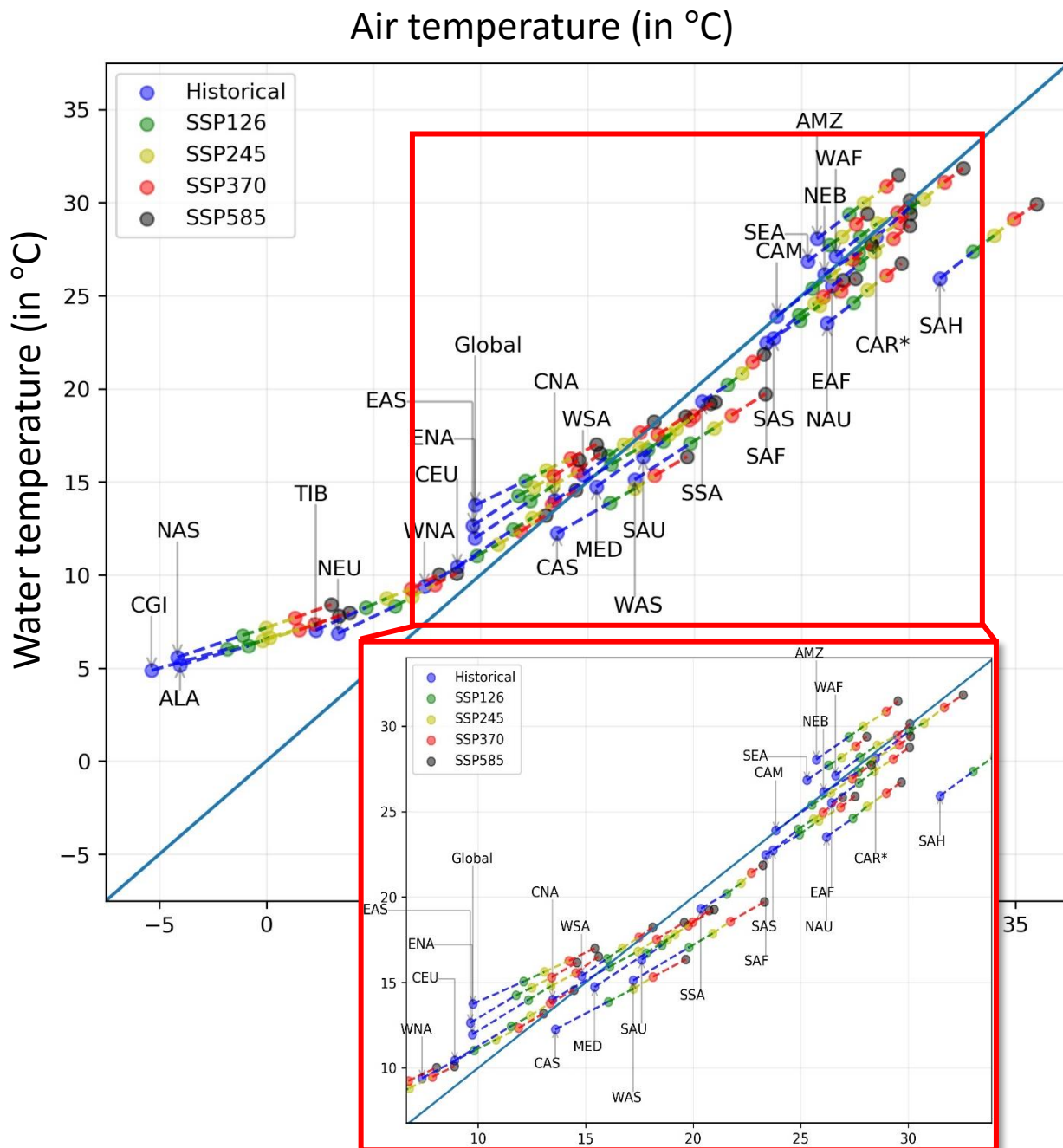


Figure 3.11: Consistency of water temperature and air temperature under anthropogenic warming

3.4.3 Seasonal changes in temperature rise due to Climate Change

3.4.3.1 Water Temperature

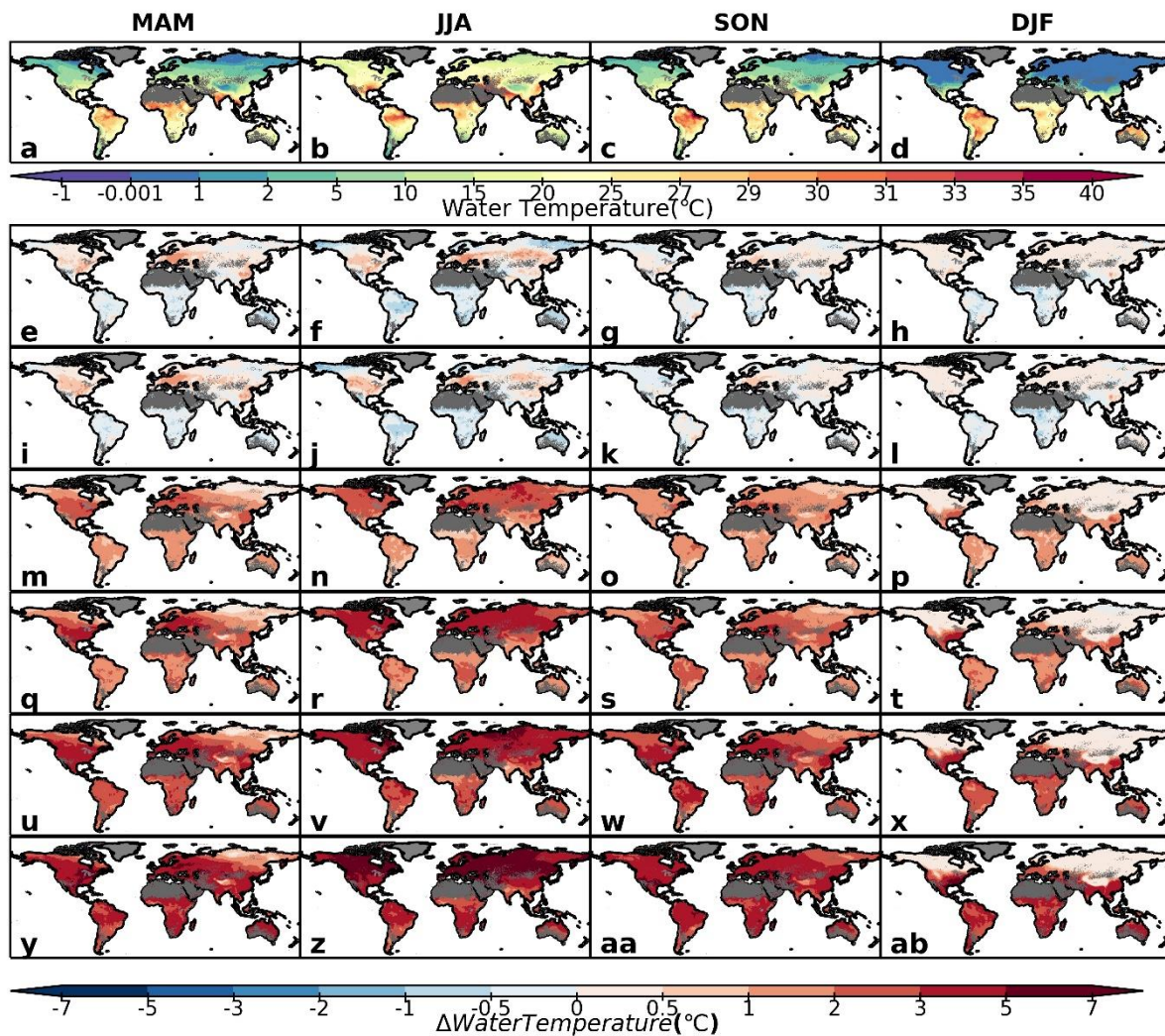


Figure 3.12: Global change in water temperature for 30-year average for natural-historical (e-h), SSP245-nat (i-l), SSP126 (m-p), SSP245 (q-t), SSP370 (u-x) and SSP585 (y-ab) against the historical scenario (a-d). 1961-1990 is considered as reference period for historical period while 2071-2100 is reference period for future scenarios.

Globally, there is almost no change in the water temperature during all seasons in the naturally forced world; however, there are some regional differences with the historical scenario (Fig 3.13). Under the naturally forced world, for historical and future scenarios, the water temperature is lower than the historical period in the equatorial region throughout the year (Fig 3.12). Such decline can be seen for high latitude regions, particularly during the summer months (JJA) but not during winter (DJF).

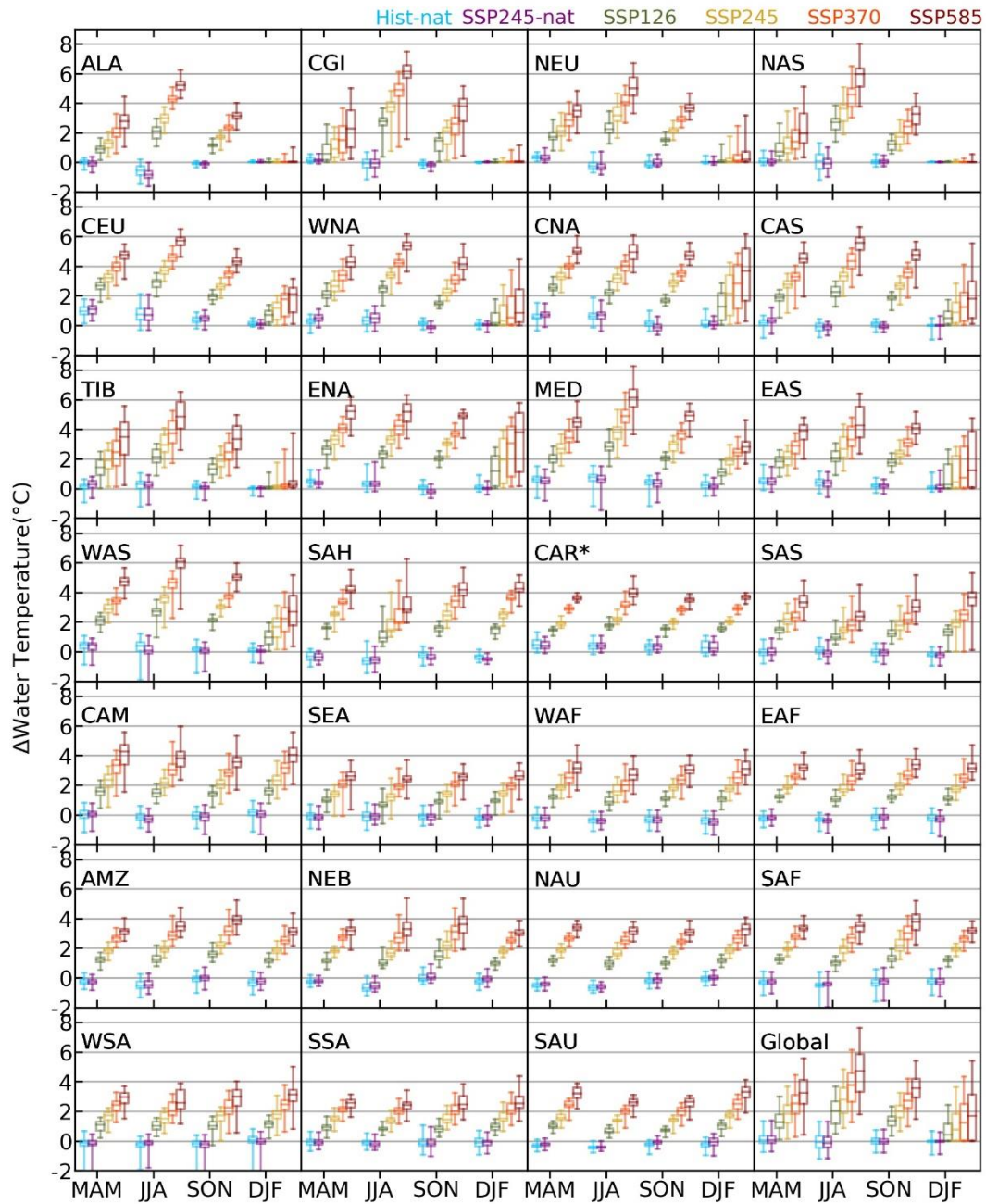


Figure 3.13: The spatial variability in the shift in water temperature at a seasonal scale differs for different SREX regions.

It may also be noticed that the water temperature is higher in a naturally forced scenario than one with the anthropogenically-forced historical scenario in the mid-latitude regions, particularly in summer. However, in all the anthropogenically forced worlds, all areas demonstrate an increase in water temperature in all seasons, although a minimal rise can be seen during the winter months. The rise in temperature is much higher in all seasons for the anthropogenically forced futures compared to the naturally forced simulations. Globally, on average, the water temperature rises by 2°C in SSP126

while about 5°C in SSP585 during the summer months. Under the anthropogenically warmed future scenarios, high latitude regions like ALA, CGI, NEU, and NAS demonstrate minimal water changes in winters (DJF), while the changes in summers (JJA) are pretty substantial (Fig 3.13). The temperature rise is restricted in winter due to the freezing of water, while there are no such constraints in the summer. A similar phenomenon can be observed in Tibet. Water temperature changes in summer are more prominent than in winter, even in the mid-latitudes of both the northern and southern hemispheres. However, equatorial regions show almost similar shifts in water temperature in all seasons. The most significant rise in water temperature can be seen under the SSP585 future.

3.4.3.2 Air Temperature

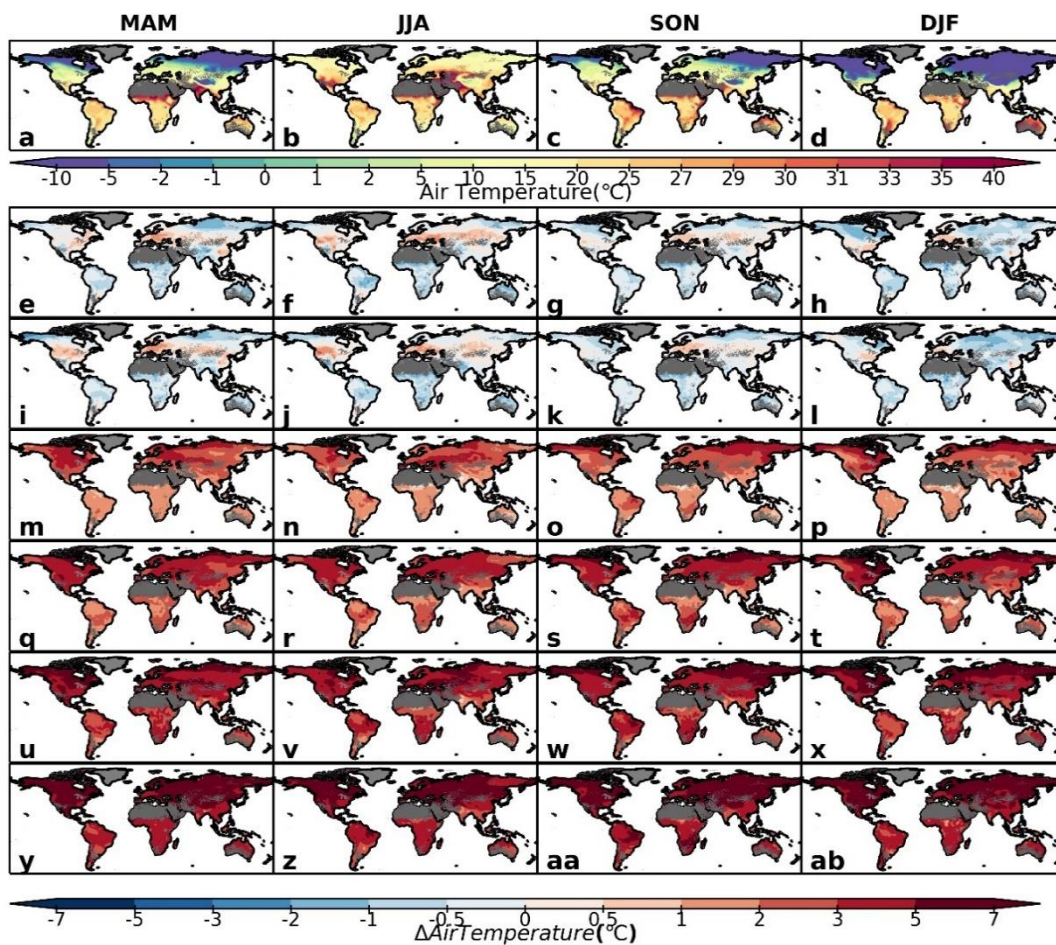


Figure 3.14: Global change in air temperature for 30year average for natural-historical (e-h), SSP245-nat (i-l), SSP126 (m-p), SSP245 (q-t), SSP370 (u-x) and SSP585 (y-ab) against the historical scenario (a-d). 1961-1990 is considered as reference period for historical period while 2071-2100 is reference period for future scenarios.

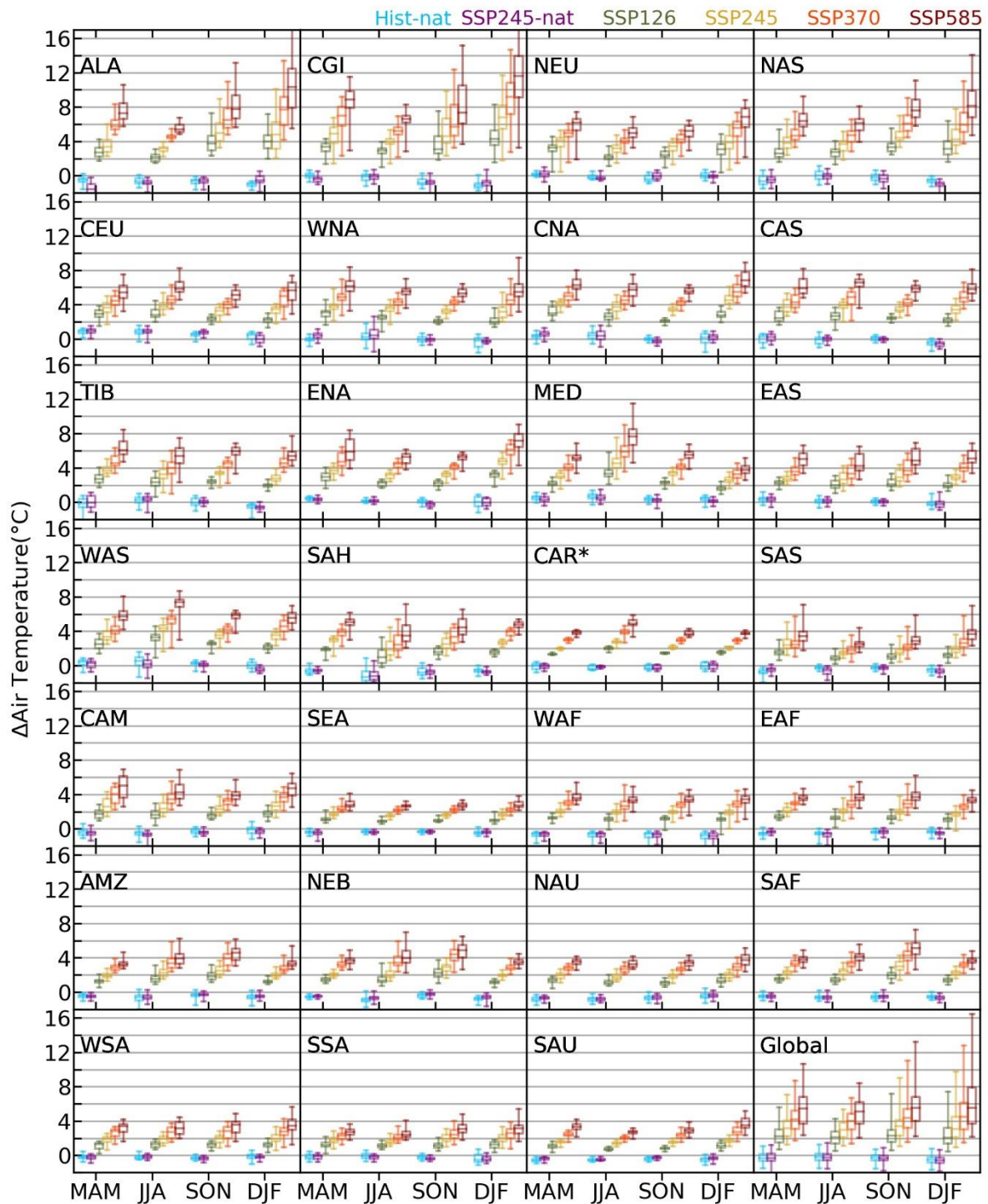


Figure 3.15: The spatial variability in the shift in air temperature at a seasonal scale differs for different SREX regions.

In the case of air temperature, the global rise over land is much higher than water temperature. The high latitude basins show the largest shift in the winters, in contrast to water temperature (Fig. 3.14). The spatial variability is also higher in the case of winter shifts in the high latitudes (Fig. 3.15). The largest changes in air temperature can be seen in SSP585, and in the natural scenario, higher than

historical period (with anthropogenic emissions) can be seen only for mid-latitude regions. However, some regions in the mid-latitude and equatorial regions (Fig. 3.15) show the largest change in the summer season like CEU, CAS, MED, WAS, CAR in the northern hemisphere (JJA) and WSA, SSA, NAU, and SAU in the southern hemisphere (DJF).

3.4.3.3 Soil Temperature

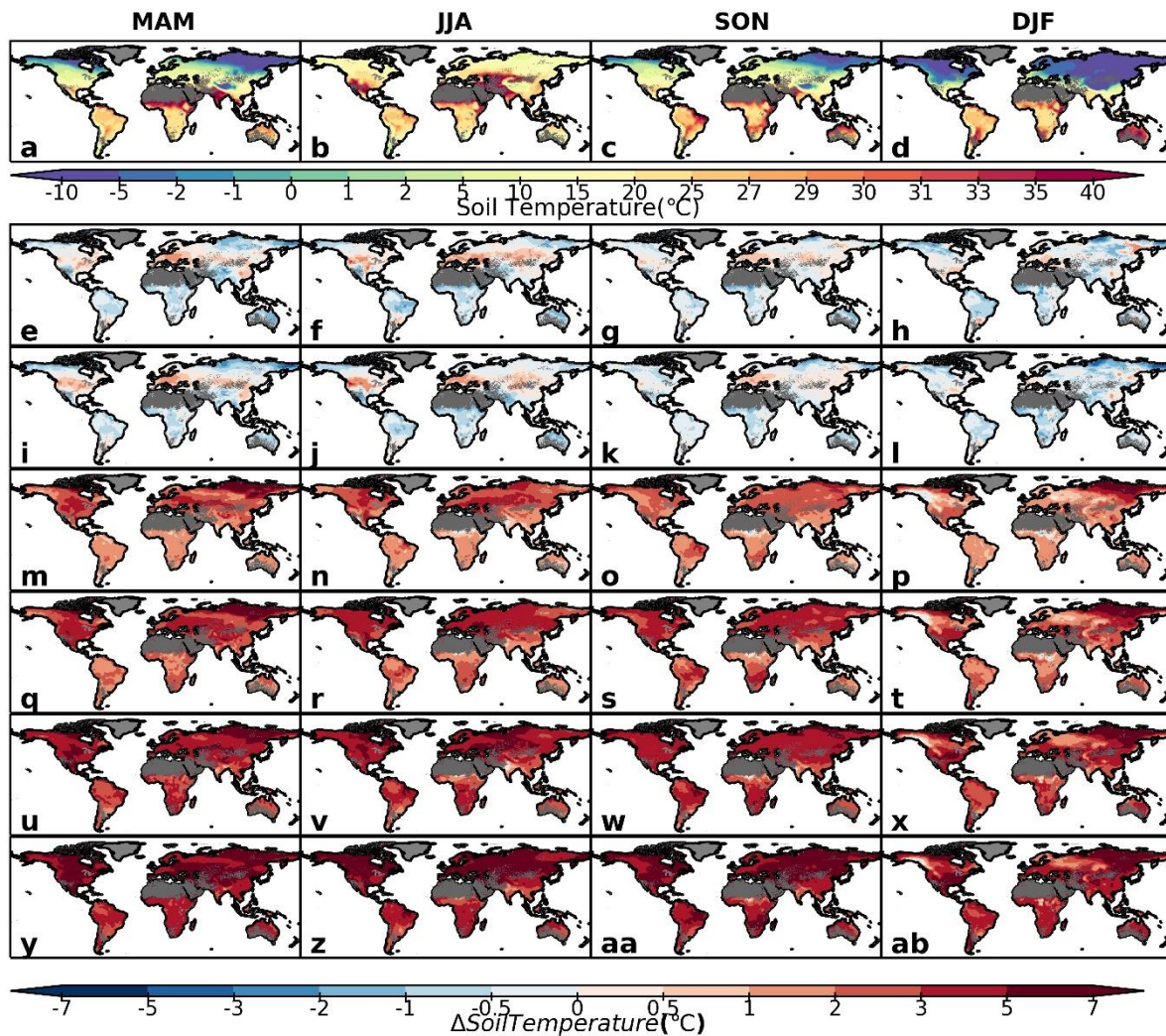


Figure 3.16: Global change in soil temperature for 30-year average for natural-historical (e-h), SSP245-nat (i-l), SSP245 (m-p), SSP126 (q-t), SSP370 (u-x) and SSP585 (y-ab) against the historical scenario (a-d). 1961-1990 is considered as reference period for historical period while 2071-2100 is reference period for future scenarios.

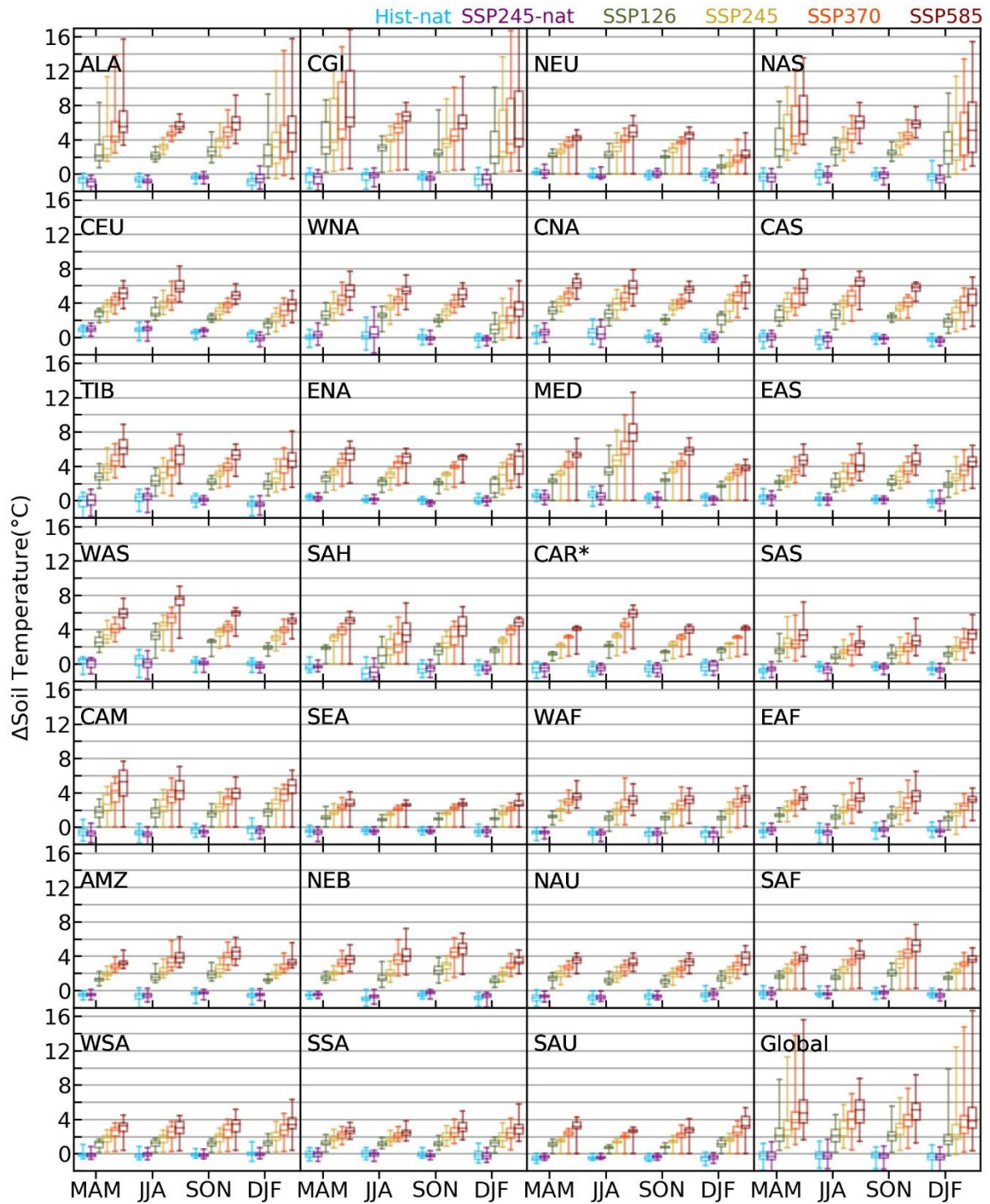


Figure 3.17: The spatial variability in the shift in water temperature at a seasonal scale differs for different SREX regions.

Similar to water temperature, higher temperature shifts for soil temperature in the high latitude regions can be seen for the summer months than winter months (Fig. 3.16).

3.4.4 Trends in water, air, and soil temperature

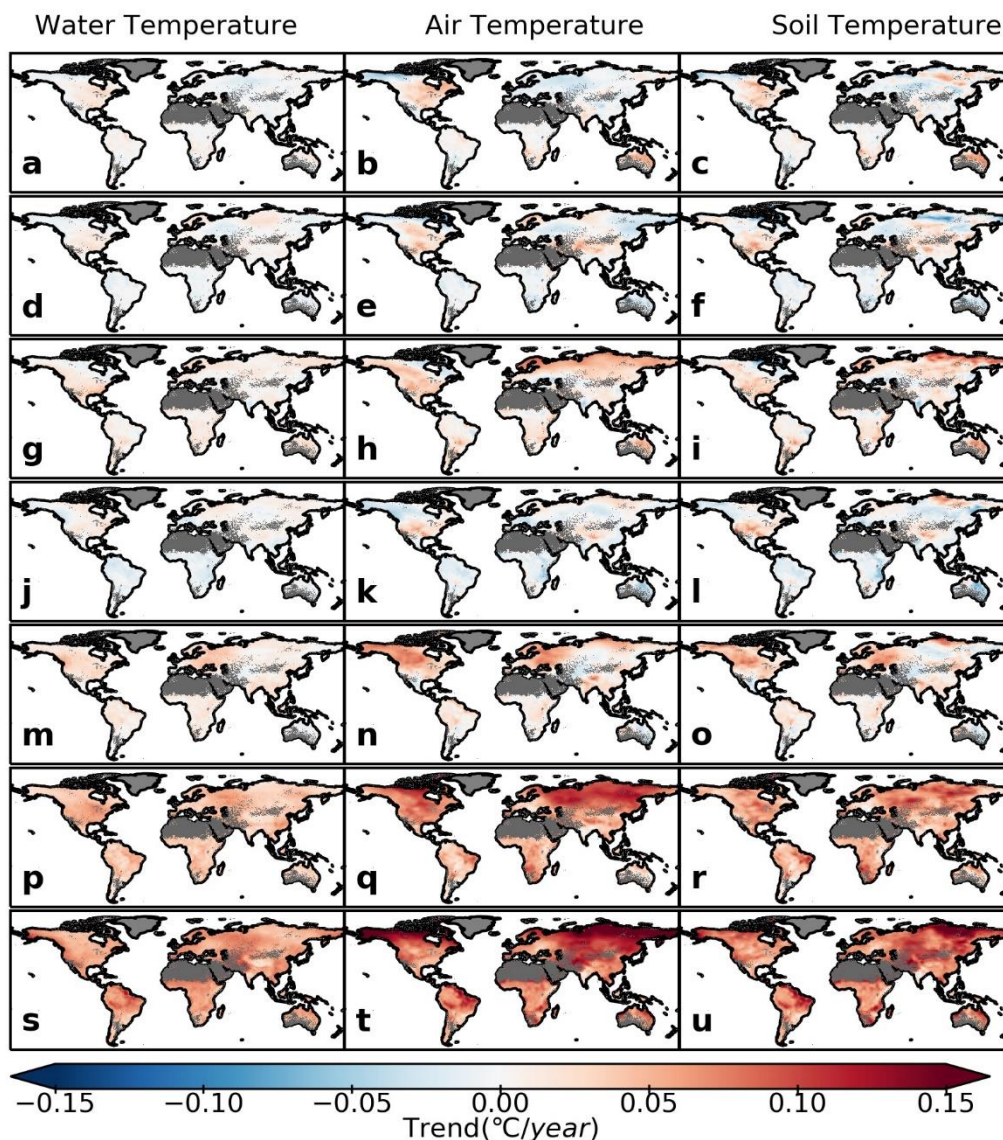


Figure 3.18: Trends in water, air, and soil temperature for the 30 years reference period for historical (1961-1990) and future periods (2071-2100). Natural-historical (a-c), SSP245-nat (d-f), historical (g-i), SSP126 (j-l), SSP245 (m-o), SSP370 (p-r) and SSP585 (s-u) scenarios.

Trends in water, air, and soil temperatures are negative in most scenarios, but in highly warmed future scenarios (SSP370 and SSP585), global temperature rises in the reference period (Fig. 3.18). Stronger positive trends are demonstrated in the case of air temperature followed by soil temperature and water temperature. A strong spatial variability can be seen in the trends for all scenarios. Stronger positive trends can be seen in the high latitudes, particularly in higher warming scenarios. However, tipping points for such strong trends can be seen in the historical scenario. Natural (hist-nat and SSP245-nat), historical, and moderate warming scenarios (SSP126 and SSP245) exhibit a negative trend in temperature at the last 30 of the 21st century. However, there were definite positive trends

initially, at least for SSP126 and SSP245, that lead to the increase in the temperature with respect to the historical scenario.

3.4.5 Climate sensitivity

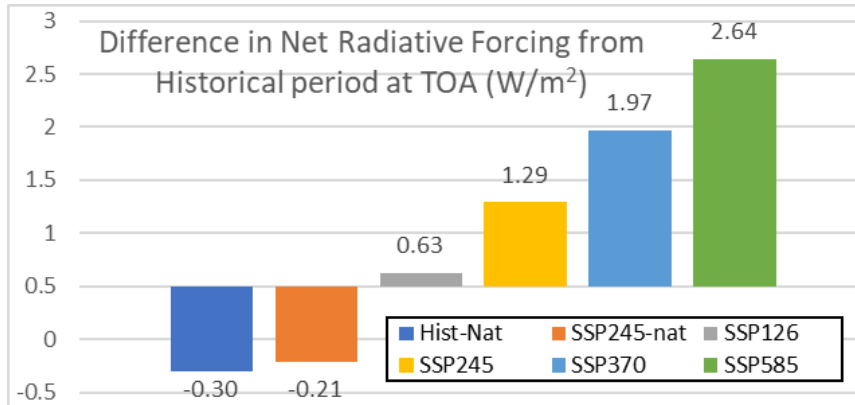


Figure 3.19: Change in net radiative forcing at the top of the atmosphere with respect to the historical period.

In natural simulations, the net radiative forcing at the top of the atmosphere is lower than the historical scenario. The radiative forcing increases in anthropogenically forced climatic scenarios, being least for SSP126 and highest for SSP585. This result is self-evident as SSP5-RCP scenarios are based on radiative forcings. The sensitivity of temperature rise to net radiative forcing at the top of the atmosphere for multiple climatic scenarios divided into different SREX regions is depicted in figure 3.20. Most interestingly, the temperature sensitivity is found to be negative under the natural scenarios in certain areas like Central Europe, Central North America, and the Mediterranean. Such negative sensitivity is not a result of the natural variability, as sensitivity is consistent for past and future natural scenarios. Rather anthropogenic warming is causing such large variability in the historical scenario. Hence, despite a greater radiative forcing, the water temperature declines. Large spatial variability under the natural simulations can also be seen in many regions.

Under anthropogenic warming, the temperature sensitivity declines with an increase in radiative forcing. The highest water temperature sensitivity is observed in the high latitude regions under SSP126. The spatial variability of such sensitivity also declines with increased radiative forcings.

Air and soil temperature sensitivity is mostly higher than water temperature, particularly in the colder regions like Alaska, Canada, Northern Asia, and Tibet. The spatial variability for air and soil temperature sensitivity is also higher than water temperature. Both mean and spatial variability of the difference in air and soil temperature sensitivity with water temperature sensitivity declines in higher warming scenarios.

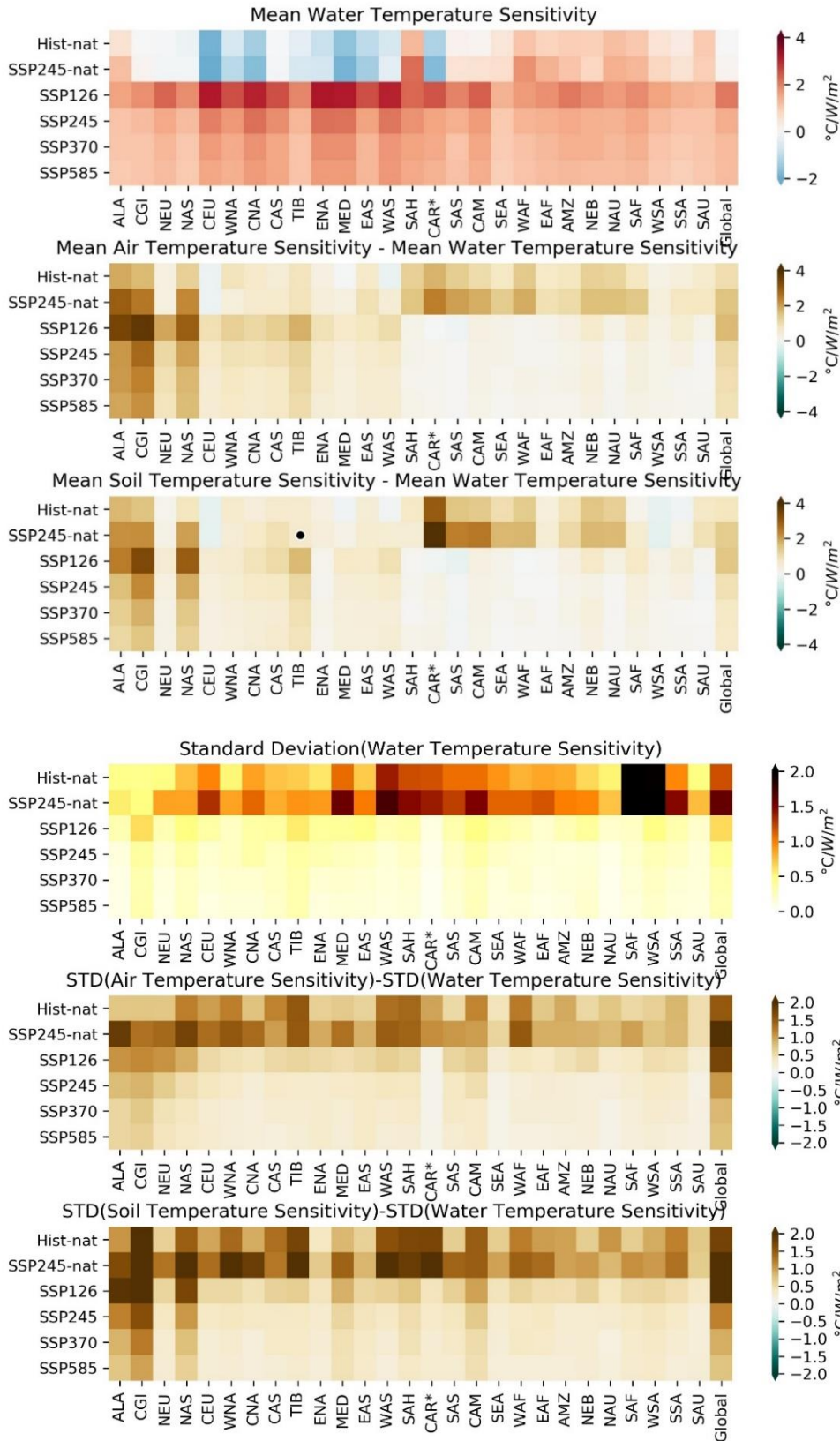


Figure 3.20: Mean and standard deviation of temperature sensitivity to radiative forcing. The probability density plot for the same is available in the appendix.

3.4.6 Attribution of temperature rise to Climate Change.

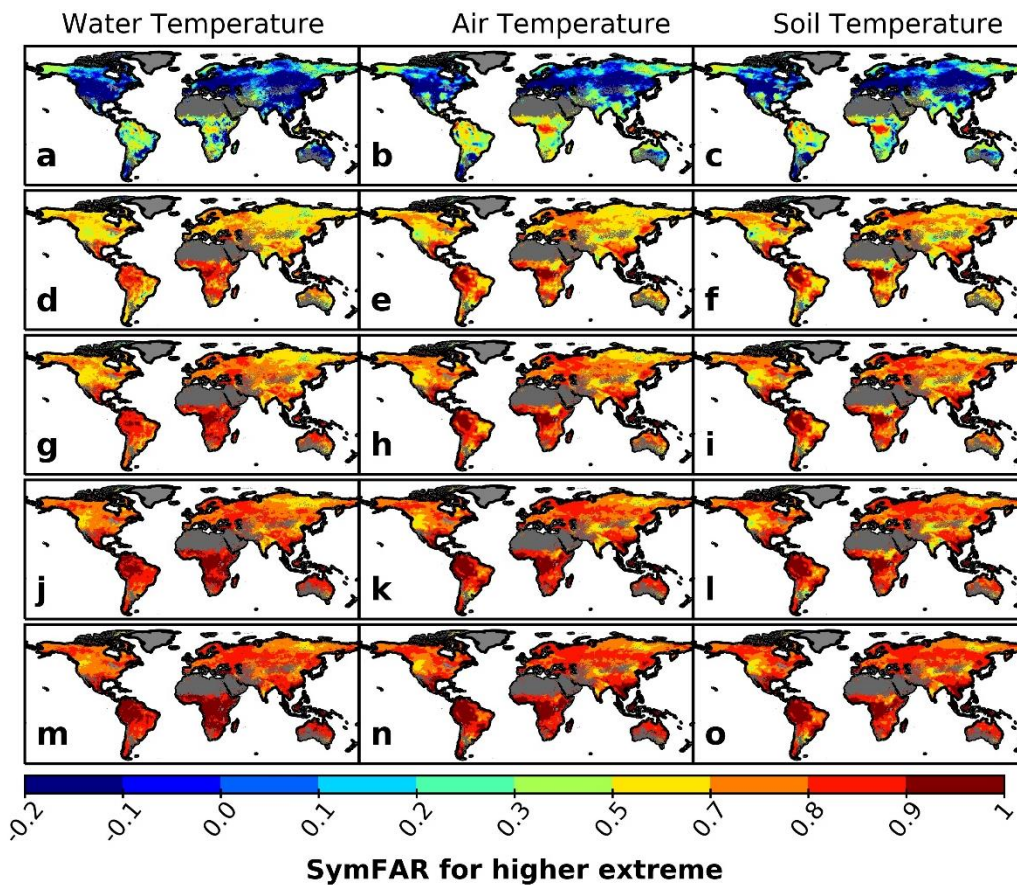


Figure 3.21: Symmetric FAR values for extreme water temperature, air temperature and soil temperature under Historical (a-c), SSP126 (d-f), SSP245 (g-i), SSP370 (j-l), and SSP585 (m-o) scenarios.

A large proportion of land, particularly in the mid-latitude regions of the northern hemisphere, displays a negative value of SymFAR in the historical scenario, signifying a decline in water temperature values due to human-induced warming (Fig 3.21a). However, all regions show a positive SymFAR in future scenarios. Regions such as Alaska, North-Eastern parts of Asia, Amazon, and most of Africa exhibit tipping points of anthropogenic influence responsible for increasing water temperature, which aggravates in future scenarios with increasing global warming (Fig. 3.21). Similar but more prominent tipping points exist for air temperature and soil temperature in their respective historical scenarios. Amazon, Central America, the west coast of South America, the Caribbean, Western Africa, and South-East Asia demonstrate the largest values of SymFAR for water, air, and soil temperature in the future scenarios (Fig. 3.22). Regions like Southeast Asia and Western Africa demonstrate a large influence of anthropogenic warming for air and soil temperature but not for water temperature.

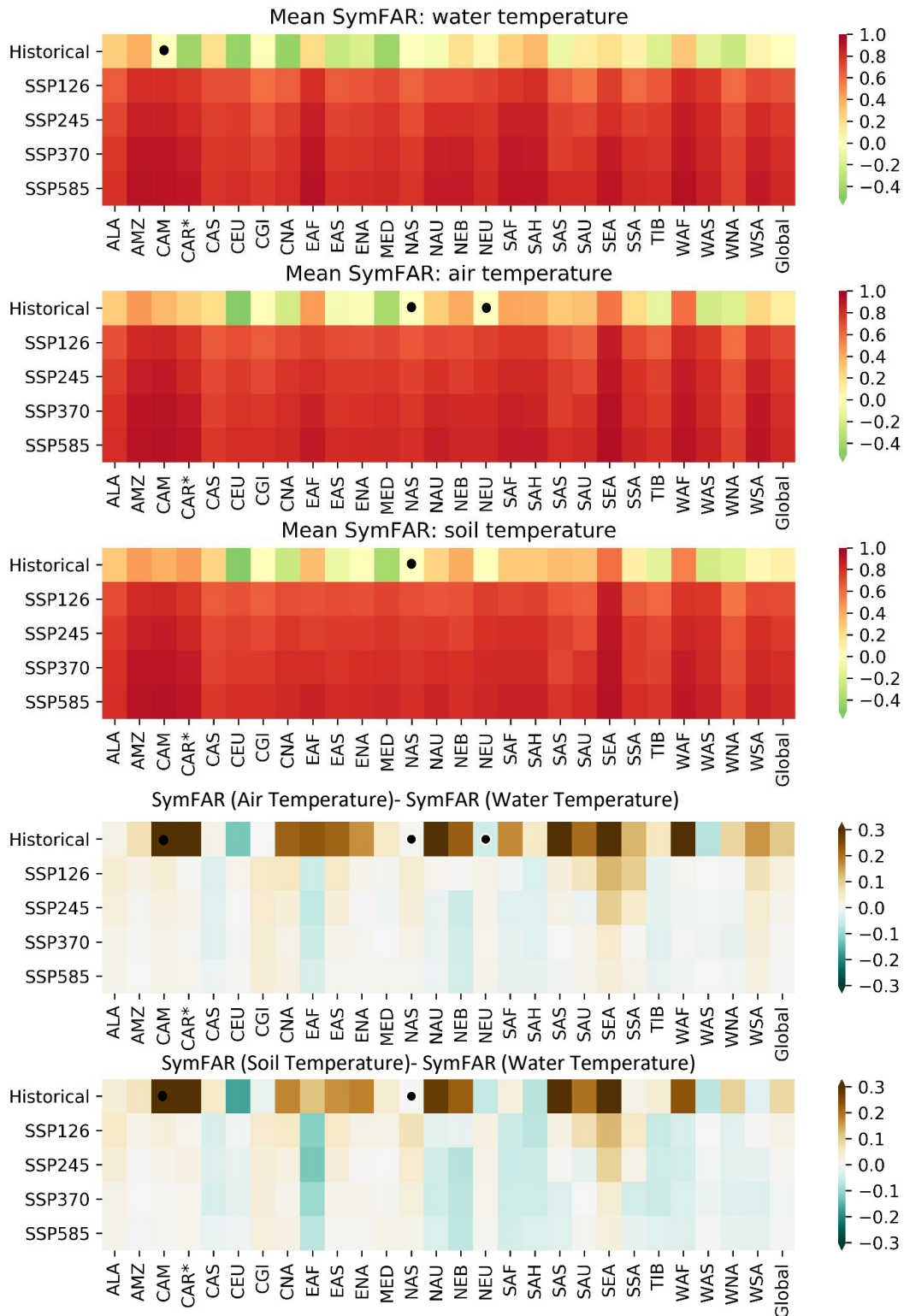


Figure 3.22: Symmetric FAR values for extreme water temperature, air temperature, and soil temperature under Historical, SSP126, SSP245, SSP370, and SSP585 scenarios for different SREX regions and globally. The 4th and 5th panels demonstrate the difference in risk attribution from water temperature for air and soil temperature, respectively.

3.4.7 Change in adverse conditions

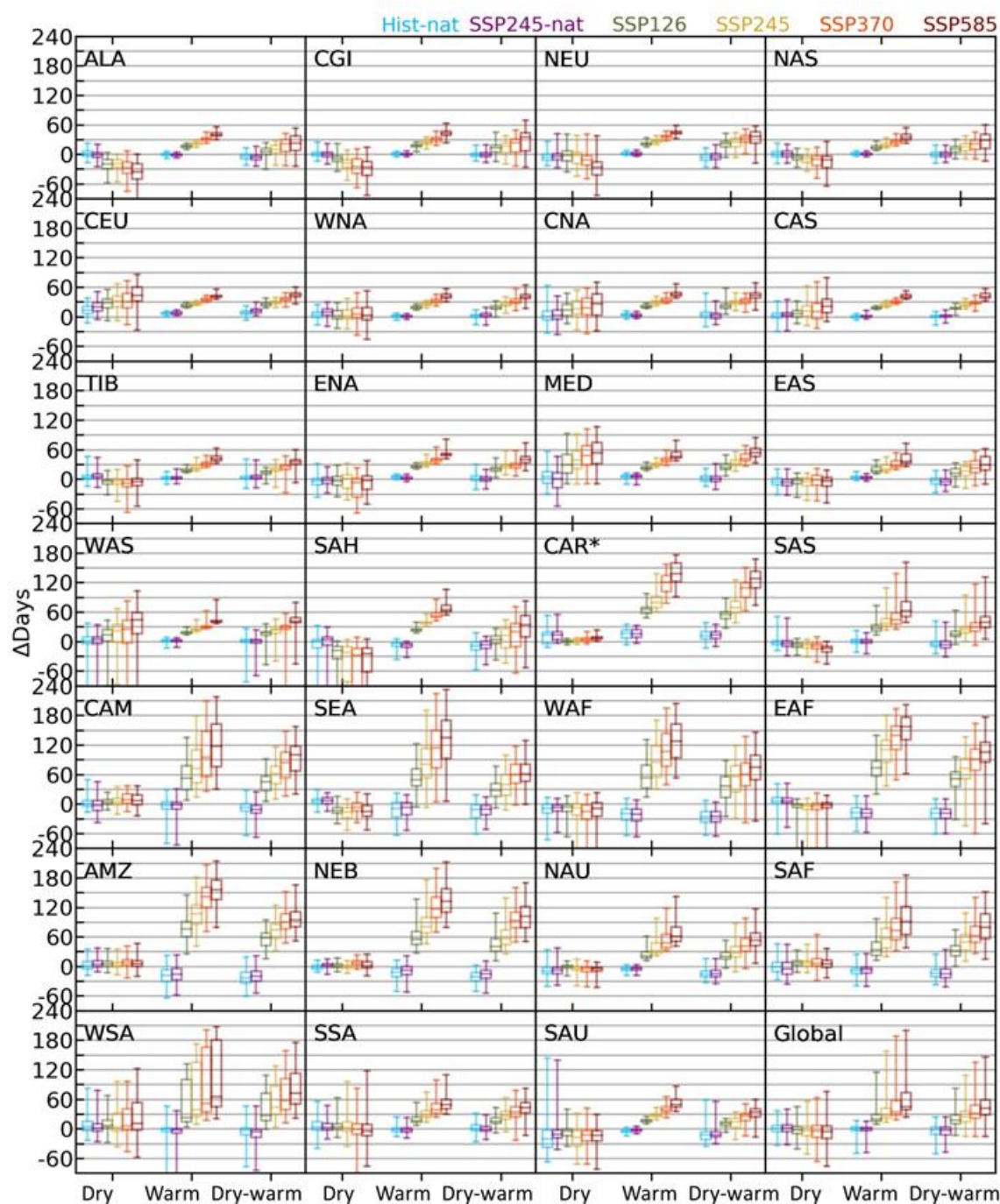


Figure 3.23: Change in dry, warm, and dry-warm days compared to the historical scenario.

Under anthropogenic warming, the number of dry days in a year increase for certain regions like Central Europe and Western Asia while decreasing for most landmasses like Southern Asia and Sahara, leading to a net decline globally. The warm days, on the other hand, increase worldwide in all four

future scenarios. The compounding of these dry and warm periods also increases in all regions and globally in these worlds. However, the changes are pretty minimal at the global scale for naturally forced worlds. Certain regions like Central Europe demonstrate a significant increase (25th percentile >0) in the number of dry days, warm days, and dry-warm days even without anthropogenic greenhouse emissions.

3.5 Discussions

The results for temperature sensitivity (Section 3.4.5) demonstrate sharp contrast with findings of mean temperature change (section 3.4.2). The mean water temperature rise intensifies in higher warming scenarios (Fig. 3.9), but the rate of intensification must decline so that the temperature sensitivity also declines (Fig. 3.20) with increased radiative forcing.

This study reveals a large spatial variability in the water temperature but does not investigate the reasons for such variability. Also, the component-wise analysis causing changes in water temperature is missing. For instance, the temperature rise that is caused exclusively due to air temperature changes and changes in incoming solar radiations can provide insights into the mechanism of water temperature change under climate change. Moreover, these results are based on a single GCM, “MIROC-6”. A multi-model analysis will decrease the uncertainties of the input data, even though the bias caused due to the HEAT-LINK itself may not be addressed.

3.6 Conclusions

This study presents a detailed analysis of water temperature changes and compares them with air temperature and soil temperature. The study uncovers these changes in historical and multiple future scenarios under natural climates and anthropogenically influenced climates. This study reveals that under anthropogenic warming, the water temperature rises at an annual and seasonal scale in all future scenarios, which increases with an increase in radiative forcing. Although, the distribution of such rise may vary over space and time for different scenarios. Multiple future scenarios reveal a decline in sensitivity of temperature rise to change in radiative forcing in anthropogenically forced worlds, while in naturally forced worlds, increase in temperature even though lower radiative forcing can be witnessed. Moreover, the increase in the compounding of dry and warm periods, that increase in the future worldwide, would severely impact aquatic life, irrigation, and power production.

Compared with air temperature and soil temperature, water temperature shows a smaller change on average and has lower sensitivity to changing radiative forcing. The seasonal variability of air temperature is different from water temperature and soil temperature. The attribution of extreme temperature shifts to HIW for water, air, and soil varies considerably in different regions. However,

HIW is majorly responsible for the extreme rise in these temperatures. Therefore, waning greenhouse gas emissions may considerably decline the temperature rise of water, air, and soil.

3.7 Future scope

The causes of water temperature variability in spatial and temporal scales have not been unearthed in this study and can provide insights into the mechanism of the shift in water temperature. While the water temperature model considerably the natural processes in water heating, anthropogenic thermal emissions are not accounted for. Domestic and Industrial effluent release often causes thermal pollution in rivers. Thermal power plants are principal contributors to this anthropogenic thermal pollution.

Water is needed for thermal power plants to cool down steam. The amount of water needed depends on the water temperature, environmental policies, and other thermal power plants' characteristics. Policies and water availability, however, may restrict the actual water withdrawal by the power plants. As the dry-warm periods elongate in the future, the power plants would be impacted acutely during this period. The next chapter discusses the impacts of climate change on power plants' power production efficiency. The impacts of thermal pollution of river temperature have been incorporated into the HEAT-LINK and discussed in the next chapter.

Chapter 4: Impact of climate change on Thermal Power Production and Anthropogenic Heat Emission

4.1 Background and Introduction

4.1.1 Water Availability

Although we live on a blue planet, with 70% surface covered with water, more than 97% of this water is saline (USGS). Although rivers and lakes consist of less than 0.01% of global water at any given instance, the riverine flow from land to the ocean is about 45,500 km³/year². This can be credited to the recharging by the hydrological cycle. However, the distribution of this bulk of water in time and space creates challenges to water availability. Additionally, some amount of water is to be left for the environmental flow. FAO defines the environmental flow as “The quantity and timing of freshwater flows required to sustain ecosystems and the human livelihoods and well-being that depend on them.” The remaining water can be used for domestic, agricultural, and industrial sectors. This leads to competition among these sectors when water availability is insufficient; the water insecurity for each sector intensifies with increasing population and development.

4.1.2 Electricity generation and demand

In the modern economy, the power demand has been growing. Today electricity is need for most operations, starting from machines running in industries to household appliances. It would not be wrong to say that electricity has become a basic amenity. The power production has risen by about five times from 1974 to 2018 (Figure 4.1) and is expected to rocket due to expanding digitalization, industrial growth, increasing air conditioning, electric heating, and electric vehicles¹⁰⁹. The growth rate is nominal in the OECD countries, while in non-OECD countries, the rate is much higher. This difference can be credited to growing industrialization, improvement in lifestyle, and expanding digitalization in developing economies. This is aided by immense population growth. China and India together account for most of the world's humans and contribute to maximum power production in the world.

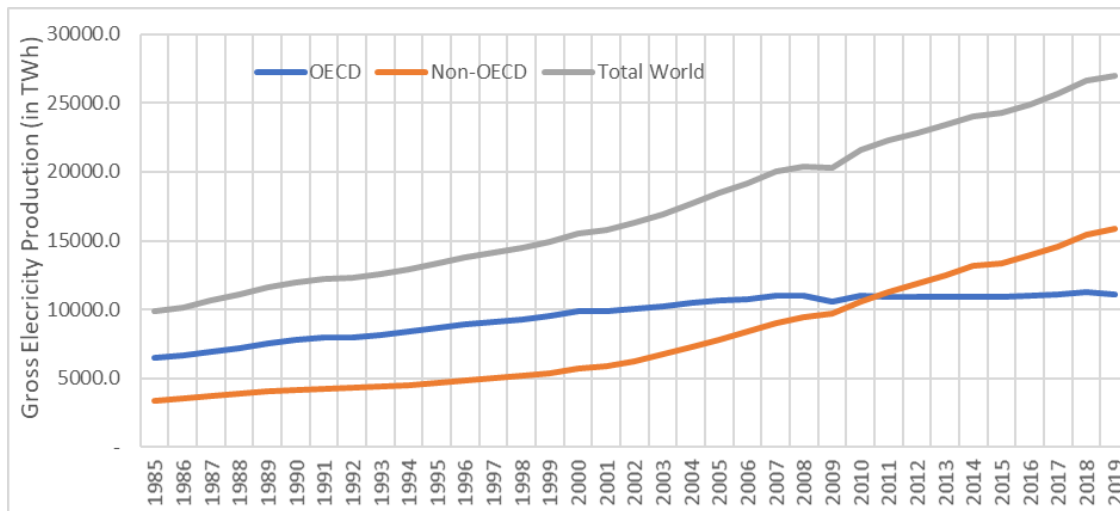


Figure 4.1: Gross electricity production for OECD countries, non-OECD countries, and the world total
The Data source: *IEA. World Energy Outlook 2019* ¹¹⁰

4.1.3 Classification of Power Plants by Fuel Type

Power plants convert some form of energy into electrical energy and can be classified as renewable and non-renewable energy sourced plants based on the fuel source they use. Renewable sources include hydropower, Solar thermal, solar PV, wind power, geothermal and tidal energy. The proportion of each of these sources for the world's gross electricity production in 2018 is represented in figure 4.2. Non-renewable fossil fuels (coal and natural gas) contribute more than 60% to electricity production.

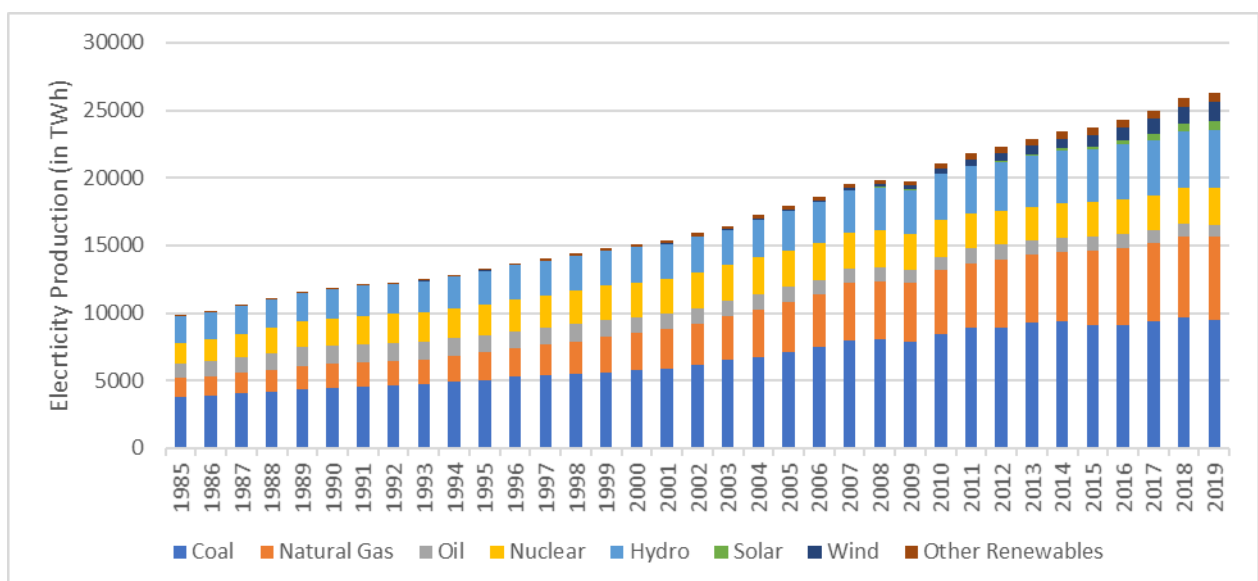


Figure 4.2: Gross electricity production at the global scale for different fuel types Data source: *IEA. World Energy Outlook 2019* ¹¹⁰

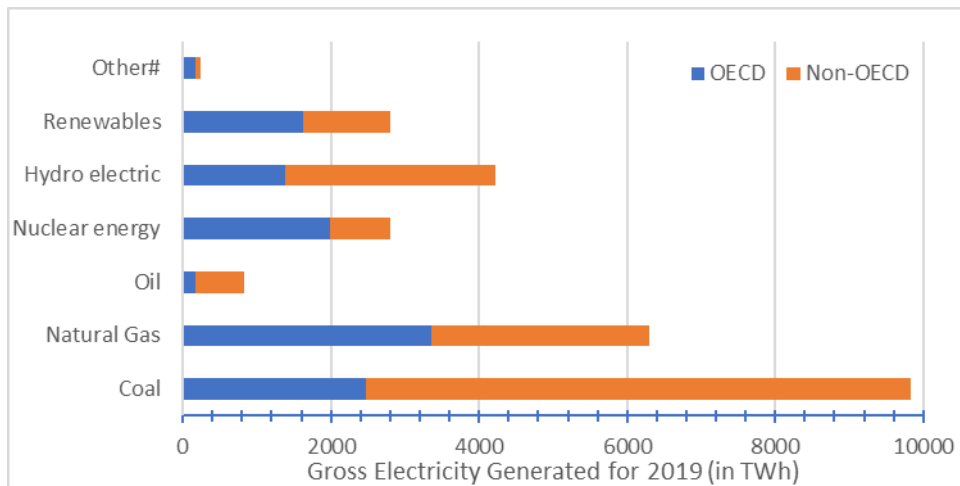


Figure 4.3: Gross electricity production for different fuel types for OECD and Non-OECD countries in 2019 # Includes sources not specified elsewhere, e.g., pumped hydro, non-renewable waste, and statistical discrepancies (which can be positive or negative). Data source: IEA. *World Energy Outlook 2019* ¹¹⁰

4.1.4 Thermal Power plants: Working Principle and Water Demand

All power plants that convert heat energy into electrical energy are termed thermal power plants. These include power plants that utilize fossil fuels (oil, gas, coal), combustible waste, controlled nuclear fission, geothermal energy, and solar energy (solar thermal plants). Most of these thermal power plants use water as their working fluid. Water is heated up inside a chamber, called a boiler, to produce steam at high temperature and high pressure that rotates the turbine of an electric generator to produce electricity. The water used for this purpose is called feed water. Feed water is a highly purified form of water to avoid scaling and corrosion of the boiler, turbine, and other equipment. This water is hardly replaced as achieving such a level of purification is an expensive and energy-demanding process. Instead, the feed water is cooled down (this also helps maintain a pressure difference for the hot steam to flow) and heated again to produce a stream. The thermal power plants generally use water to cool down the stream, known as cooling water. Thermal power plants can be further classified based on the type of cooling system they use. There are primarily three types of cooling systems in operation.

1. Air Cooled systems: As the name suggests, these cooling systems use air to cool the steam. Large fans or radiators are installed, and the difference in temperature between the air and feed water is utilized for cooling. Sometimes, these cooling systems use water

sprinklers to increase the efficiency of cooling. Nevertheless, the water consumption is very insignificant in comparison to other types of cooling systems. However, this type of cooling system consumes a sizable amount of generated electricity (~2%) and has hefty installation costs, reducing the power plants' efficiency in terms of both production and economics. Hence these are generally avoided when water is available for cooling. However, in the case of decentralized power plants, these are often used by pumping ground water.

2. Once-through cooling system: These are the most commonly used cooling systems. They continuously withdraw a large amount of water from some water source, cool the steam, and return the hot water to the same source. Thus, increasing the water temperature of rivers, lakes, and reservoirs, these power plants are the leading thermal polluters.
3. Recirculating Tower cooling system: The cooling water absorbs heat from steam and is recirculated after cooling it down in a cooling tower. Water spins in the cooling towers, and heat is lost by evaporation. The water lost by evaporation is withdrawn from a water source and added to the cooling system, called make-up water. This kind of cooling system has the highest water consumption.

The fourth type of cooling system, called the combined cooling system, integrates once through and recirculating cooling system. The power plants with a combined cooling system (CB) normally behave as a power plant with a once-through cooling system (OT). But during warmer periods and water shortages, they use a cooling tower that cools down the water before releasing it back to the water body. There is generally no recirculation in this type of cooling system. Such dynamic allocation of cooling towers (DACT) is a distinctive feature of CB.

4.1.5 Water-Energy Nexus

A tremendous amount of water is required for generating electricity, as discussed in section 4.1.4. Additionally, water is needed to obtain fuel for electricity generation¹¹¹. However, the water supply also needs electricity. Electric power is required for water withdrawal at the intake point, for water treatment (including desalination), and for pumping it for domestic and industrial use. About 7% of global electricity production is used for water pumping¹¹¹. Usage of water in domestic and industry also needs energy. For instance, a washing machine uses electricity for its operation, and electric stoves consume electricity for heating water. The wastewater treatment also requires electricity. Hence, there is a co-dependence of water and electricity: electricity production needs water, and water supply and usage needs electricity. This forms the water-energy nexus. In fact, the food production, processing, and supply also need both electricity and water, giving rise to an even complicated water-food-energy nexus. However, this study focuses only on the water-energy nexus.

4.1.6 Impact of Climate Change on Thermal Power Plants and water-energy nexus

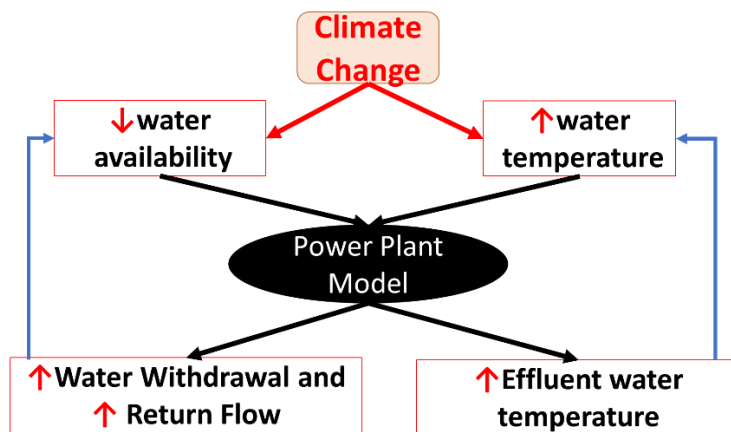


Figure 4.4: Climate change impact on thermal power plants and thermal emissions

Climate change also has some impacts on electric power demand. For example, with an increase in hot days, the usage of electrical appliances like fans, air-conditioners, air coolers, and refrigerators increases. Similarly, for colder days, the demand for electric heaters and water heaters increases. But also in the future, technological advance¹¹²ments in energy-efficient devices may neutralize such an increase in power demands. But this is possible for developed economies; however, for developing economies, with increased purchasing capacity, improvement in lifestyle, and industrial growth, the electricity demand would shoot up. The IEA (2019) attributes 90% of global energy demand to developing economies by 2040. However, the per capita demand may still be lower by 60%.

4.1.7 Ecological Integrity of water bodies

Ecological integrity is the essence of a healthy water body. Physical, chemical, and biological integrity together builds ecological integrity. Sunlight penetration, water temperature, flow, slope, morphology, ground water flow, and other physical attributes are encompassed under physical integrity. Chemical integrity covers the chemical components and most water quality parameters like turbidity, hardness, pH, nutrient and organic matter content, sediments, and dissolved oxygen. On the other hand, biological integrity comprises life forms, biological processes, and their interactions ¹¹². Water temperature is a key component of ecological integrity as it substantially affects physical, chemical, and biological integrities. Water temperature changes majorly influence the dissolved oxygen, the reactivity of chemical components, and aquatic life (as discussed in section 3.1).

4.1.8 Role of Power plants in Thermal Pollution and Influence of climate change

Power plants with once-through and combined cooling systems are predominant culprits of thermal pollution in most thermally polluted water bodies. They withdraw large volumes of cooler water and return the water with increased water temperature. Even though the water consumption is negligible, the withdrawal volume is enormous, so is the impact on water temperature.

As the water temperature rises with global warming, more water will be needed to cool the same amount of steam that drives the turbines of the electric generator. There are two significant reasons for this. Firstly, the withdrawal cooling water itself would have a higher temperature, reducing the temperature difference between water and steam. Secondly, in the case of combined cooling, as the air temperature would also be higher, more water would be lost to evaporation inside the cooling tower, and hence more makeup water is needed. Hence water consumption would increase for power plants with combined cooling and tower cooling systems.

4.1.9 Water Temperature rise due to Thermal Power plants

Gingerich and Mauter (2015) estimated that the thermal (coal, natural gas, and nuclear) power plants in the USA discharged some 18.9 billion GJ of waste heat in 2012, 4% (803 million GJ) of which was discharged at temperatures greater than 90°C. The rest (96%) is condenser heat discharged to the environment at temperatures below 42°C. Further implementation of FGD technologies at coal-fired power plants (with their higher temperature exhaust gases) and the higher quality heat generated in the exhaust of natural gas fuel cycles could increase the availability of waste heat generated by 10.6% in 2040.

4.1.10 Previous Studies and Research Gaps

Van Vliet et al. (2016)⁵² provided the equations for calculations of cooling water required and the thermal power production, following constraints on water withdrawal and thermal pollution, as shown in equations below:

$$q = \frac{KW \cdot \frac{1 - \eta_{total}}{\eta_{elec}} \cdot (1 - \alpha) \cdot (1 - \beta) \cdot \omega \cdot EZ}{\rho_w \cdot C_p \cdot \max(\min(Tl_{max} - T_w), \Delta Tl_{max}), 0)} \quad \text{Equation 4 – 1}$$

$$P_{thermo} = \frac{\min((\gamma \cdot Q), q) \cdot \rho_w \cdot C_p \cdot \max(\min(Tl_{max} - T_w), \Delta Tl_{max}), 0)}{\frac{1 - \eta_{total}}{\eta_{elec}} \cdot \lambda \cdot (1 - \alpha) \cdot (1 - \beta) \cdot \omega \cdot EZ} \quad \text{Equation 4 – 2}$$

where: q = daily cooling water demand [m^3s^{-1}]; P_{thermo} = usable capacity of thermoelectric power plant [MW]; KW = installed capacity of thermoelectric power plant [MW]; η_{total} = total efficiency [%]; η_{elec} = electric efficiency [%]; α = share of waste heat not discharged by cooling water [%]; β = share of waste heat released into the air; ω : correction factor accounting for effects of changes in air temperature and humidity within a year; EZ = densification factor accounting for replacement of water in cooling towers to avoid high salinity levels; λ = correction factor accounting for the effects of reductions in efficiencies when power plants are operating at low capacities; ρ_w = density fresh water [kg m^{-3}]; C_p = heat capacity of water [$\text{J kg}^{-1} \text{ } ^\circ\text{C}^{-1}$]; $T_{\text{I}_{\text{max}}}$ = maximum permissible temperature of the cooling water [$^\circ\text{C}$]; $\Delta T_{\text{I}_{\text{max}}}$ = maximum permissible temperature increase of the cooling water [$^\circ\text{C}$]; γ = maximum fraction of streamflow to be withdrawn for cooling of thermoelectric power plants [%]; T_w = daily mean river temperature [$^\circ\text{C}$]; Q = daily streamflow [m^3s^{-1}].

For the once-through cooling system, as there is no tower cooling, $\beta = 0$; $\omega=1$; $EZ=1$. Hence, a once-through cooling system can be considered a special case of the recirculating cooling system with a cooling tower. A combined cooling system can also be considered as a case where β is greater than 0 but less than TC . Further, the parameters ω range between 0.7 and 1.25, and EZ ranges between 1 and 4^{113} . However, there is no specific range for α and β that could be found in the previous works although, both these values must be between 0 and 1.

Most studies in the past use expensive power plant data^{50,52} that limit the applicability of the power plants without specific cooling system information and efficiencies. Some use open-sourced data for calculating only the thermal pollution but use constant annual rates of thermal emissions^{44,114,115}, limiting their applicability under climate change. This stud attempts to determine these values by parameter estimation based on previous studies and use it for open-sourced data to represent the power plants realistically. This would enable the applicability of the model for data-scarce power plants. Also, the DACT has not been sufficiently discussed. This study hypothesizes that the DACT might be helpful in building climate resilience in the CB. The thermal emissions might also be smaller for CB due to the usage of cooling towers, which can substantially reduce the temperature of effluent water. Further, due to the DACT, OT and CB may have completely different behavior in future climates. This study investigates the above-stated issues in detail and can be helpful in proposing policies for better cooling efficiency and reduced thermal pollution to freshwater bodies.

4.2 Data

4.2.1 Hydro-meteorological Data

The same hydroclimatic and land-surface data as mentioned in section 3.2 is used as input data for the newly developed power plant model.

4.2.2 Power plant Data

No single database is present to date with all the required data for the modeling power plant production and thermal pollution.

Table 4.1: Open-sourced data available for power plants. Raptis: Raptis et al., 2016; GEOPP: Global Energy Observatory Power plant; WRI: World Resource Institute; CARMA: Carbon Monitoring for Action.

Database	Capacity	Location	Cooling System	Fuel	Commence -ment date	Decom -mission date	PP Units	Cycle Efficiency	Rankine Cycle
Raptis	✗	✓	✓	✓	✓ (Decade)	✓	✓	✓	✓
GEOPP	✓	✓	○	✓	✓	○	✓	○	○
WRI	✓	✓	✗	✓	○ (Year)	✗	✗	✗	✗
CARMA	✓	○	✗	✗	✗	✗	✗	✗	✗

4.3 Methods

4.3.1 Power plant matching

The four power plant datasets are combined and matched to get necessary parameters such as cooling system type, location, capacity, fuel type, and date of initiation. The data, however, is not available in an organized manner. Levenshtein Distance is used to calculate the differences between sequences of letters in the string to attribute the power plant to a particular cooling system type and source of cooling water in certain databases like GEOPP. For instance, Patnow Coal Power Plant Poland with 800MW capacity in the GEOPP dataset describes the source of cooling water as an “open-loop cooling system based on the five lakes of the Konin region combined system of canals.” The extracted features are cooling system type, i.e., “open-loop” and water source, i.e., ‘Lake.’ Sometimes manual correction is also applied to classify power plants, and google maps are also used to determine the water source and type of cooling system.

Certain datasets like GEOPP and Raptis dataset provide the information of each power plant unit separately rather than the power plant itself. The list of units for each power plant was prepared that provided all the provided information. Once features are assigned for all the available power plants in

each dataset were sorted, power plants were matched. The key parameter used for this purpose is the distance between power plants across different datasets.

The major determinant of the water withdrawal and consumption in a power plant is its cooling system type, even though other factors like fuel type and type of Rankine cycle play a role in determining the cooling efficiency. As the Raptis dataset provides the cooling system type for all power plant units, this data is used as the reference. The distance between the location of the power plants in the Raptis dataset was found for all the power plants in the GEOPP dataset. The top ten power plants with the least distance in each dataset are found for each power plant in the Raptis dataset, and the rest are discarded. For these 30 distances, other available features such as cooling system type, source of cooling water, and fuel type are also matched and based on a matching score when multiple power plants are within a small distance range (within 1 km). When no other features are available, the power plant with the least distance is considered a match.

This study uses power plants that have a 100% match of the location (i.e., distance is 0) and other classifications such as water source and cooling system type (if available) with the GEOPP dataset only (Fig. 4.4). A matrix of power plant efficiency (based on fuel type and Rankine cycle) and power plant capacity (for each GEOPP unit) is prepared for the power plants at a daily scale (considering the date of commencement) at a 0.25° resolution grid (please note the word “grid” in this dissertation refers to the spatial grid and not electrical grid unless until specified). The GEOPP plant’s location, capacity, and information are used with the Rankine cycle, electrical efficiency (cycle efficiency), fuel type, water source, and cooling-system type information from the Raptis dataset. The total efficiency (the product of mean cycle efficiency, the electric generator, and mechanical turbine efficiencies) is calculated from previous studies based on fuel type and Rankine cycle. A distinction of the cooling system is adopted for both power plant efficiency and power plant capacity. When two or more power plants with the same cooling system are in the exact grid location, the average of their efficiencies and sum of capacities is considered for that grid.

Table 4.2: The electrical efficiency as given in Raptis et al., 2016.

Fuel Group	Simple Rankine Cycle	Reheat reg/n	Double reheat reg/n
Biofuel	32.4		
Coal	33.8	40.3	43.7
Gas	33.9	40.4	
Geothermal	22		
Nuclear	26.5	29.3	
Oil	34.2	40.6	
Waste	30.7		

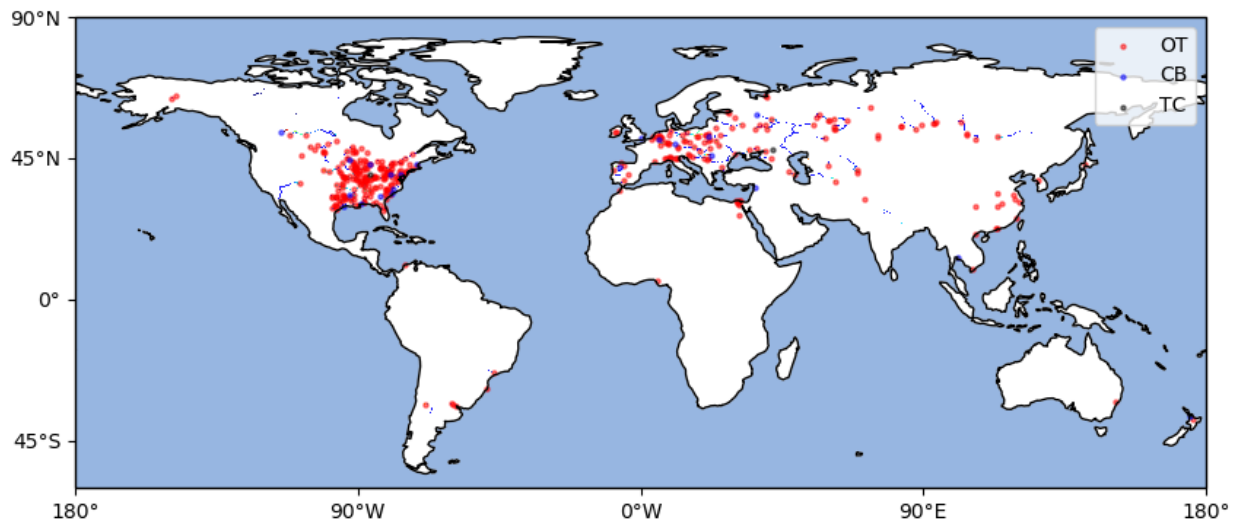


Figure 4.5: Location of matched power plants with once-through (OT), combined (CB), and tower cooling (TC) systems

4.3.2 Model Development for power plant water withdrawal, power production, and return flow

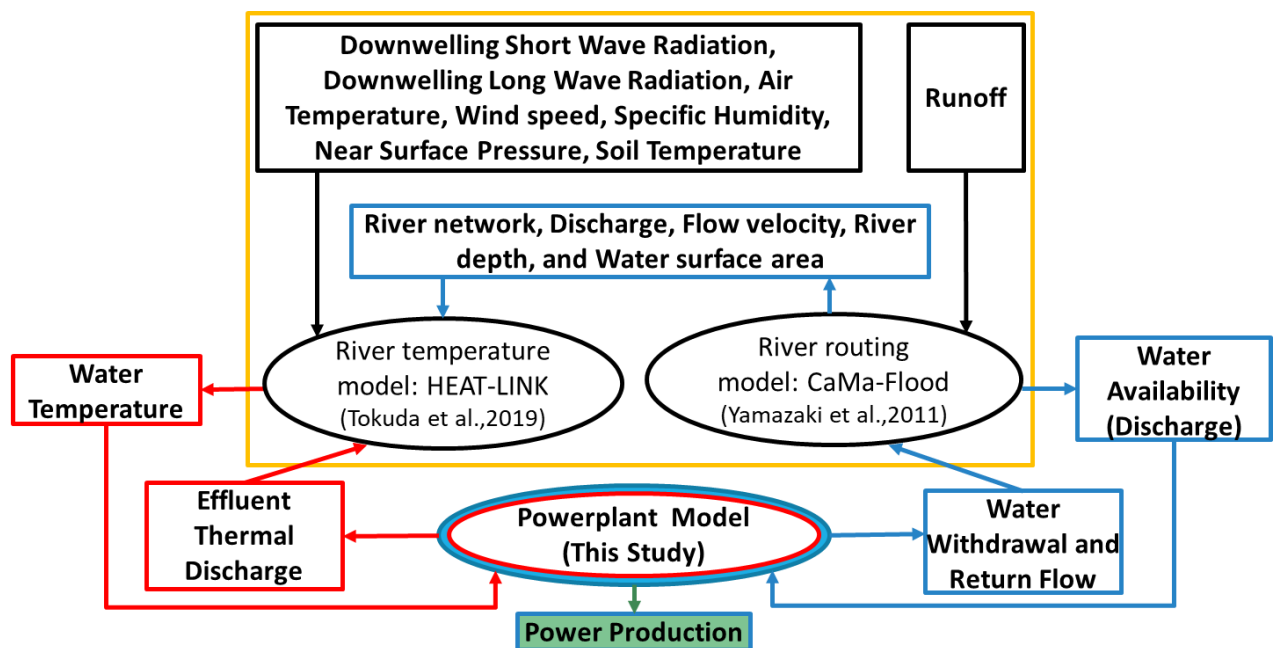


Figure 4.6: Schematic Representation of Power plant Model coupled with the existing HEAT-LINK and CaMa coupled model (inside the yellow box)

The HEAT-LINK model is modified to accommodate the power plants in the water temperature simulation. The power plant water withdrawal and thermal power production are calculated using Equations 4-1 and 4-2. HEAT-LINK and CaMa-FLOOD are tightly coupled with the power plant model (Fig. 4.5). At each time step, the discharge computed by CaMa flood and water Temperature simulated

by the HEAT-LINK serves as input for the Power plant model. The efficiency matrix, the power plant capacity, and temperature limits are used to calculate the water required (eq. 4.1). Based on available water, water withdrawal and power production are computed. The 80% of discharge ($\gamma=0.8$) is set to be available for withdrawal and a 3°C rise in water temperature ($\Delta T_{l_{max}} = 3^{\circ}\text{C}$) is allowed, with a maximum river water temperature of 33°C ($T_{l_{max}} = 33^{\circ}\text{C}$). When withdrawal water temperature exceeds 33°C, an additional temperature rise of 1.5°C ($\Delta T_{l_{max}} = 1.5^{\circ}\text{C}$) is allowed. This is based on the extra thermal discharge allowance during warm months. If there are no power plants in a grid, the power plant model gets skips in the calculation flow (Fig. 4.6). Additionally, the water is allocated preferentially to TC, followed by CB and OT at the end when they are in the same grid. Based on previous studies, the return flow for the once-through system is set to be 99% and combined cooling to 90%. There is no return flow for tower cooling.

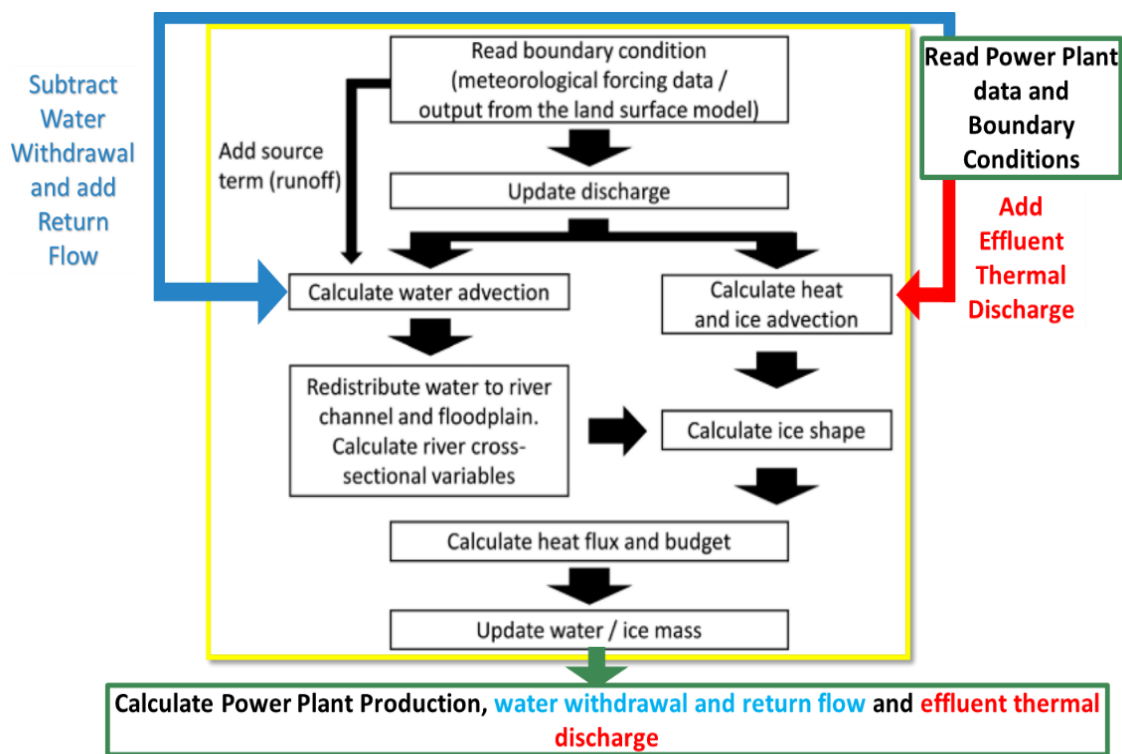


Figure 4.7: Calculation Flow for Each Timestep. The Yellow box represents the existing HEAT-LINK coupled with CaMa-FLOOD.

The cooling parameters are estimated based on theoretical values of minimum and maximum water withdrawals and thermal emission ratio based on the previous studies^{50,116}, where

$$\text{Thermal emission ratio} = \frac{\text{Emission in this study}}{\text{Emission in Raptis et al.}}$$

A dynamic allocation of cooling tower (DACT) is incorporated into the power plant model, which enables the power plants with combined cooling system (CB) to utilize the cooling tower only when necessary; otherwise, the CB behaves as a power plant with a once-through cooling system (OT). The CB uses a cooling tower when the water temperature rises above 23°C, or water demand is higher than the water available after considering an environmental flow of 40%. The thresholds for environmental flow and water temperature are considered as problems to arise for power plants when the water temperature rises above the 23°C threshold¹¹⁷, and the freshwater ecosystems can sustain under the acceptable ecological condition at 40% flow¹¹⁸.

To control the thermal emission from the power plants, a maximum of 3°C rise in temperature or a maximum water temperature of 32°C at the point of thermal effluent discharge is considered based on fish conservation laws¹¹⁷. These temperature thresholds vary for different regions in practice, but for the simplicity of the model, these are considered constant globally. An additional allowance of 1.5 °C is provided to account for the allowance that the thermal power plants get when the inflow water temperature itself is higher than the emission standards.

4.4 Power plant capacity and sensitivity analysis for cooling parameters

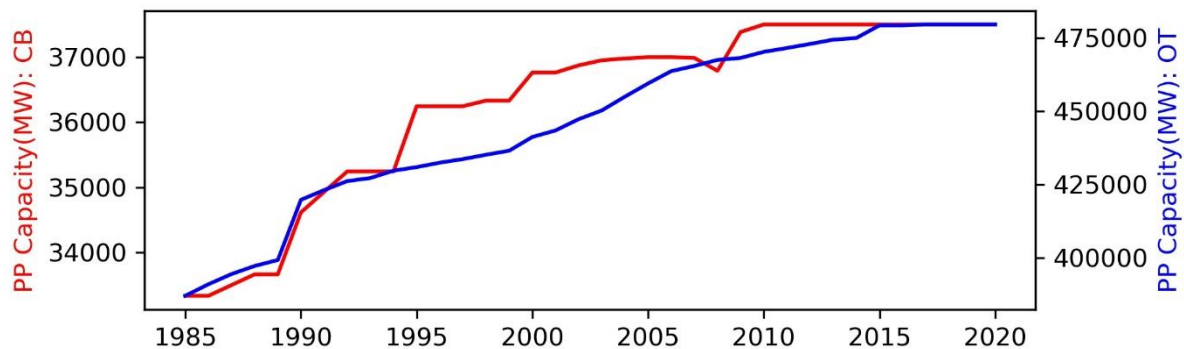


Figure 4.8: Progression of power plant label capacities (PP Capacity) for power plants with once-through (OT) and combined (CB) cooling systems

Table 4.3: Number of power plants with once-through (OT) and combined (CB) cooling systems till 2014 and in future

No. of Power plants	Till 2014	2071-2100
OT	407	410
CB	29	29

The optimal value of the cooling parameter α is found to be 0.55. This value is reasonable as only 40% heat energy of water is retained and 60% is lost [Ian C Kemp, in Pinch Analysis and Process Integration (Second Edition), 2007]. The heat is retained so that less amount of energy will be needed to convert the water to steam in the boiler. The value of β is calculated for tower cooling as 0.97, based on the

previous estimates of cooling water requirements¹¹⁶. The value of β is assumed to be 0.7 for combined cooling. Hence, the cooling parameters for the power plants with once-through system: $\alpha = 0.55$, $\beta = 0$, $\omega = 1$, $EZ = 1$,

combined cooling system: $\alpha = 0.55$, $\beta = 0.7$, $\omega = 1$, $EZ = 1$, and

tower cooling system: $\alpha = 0.55$, $\beta = 0.97$, $\omega = 1$, $EZ = 1$.

The above parameters are assumed to be consistent for all the power plants with a particular type of cooling system.

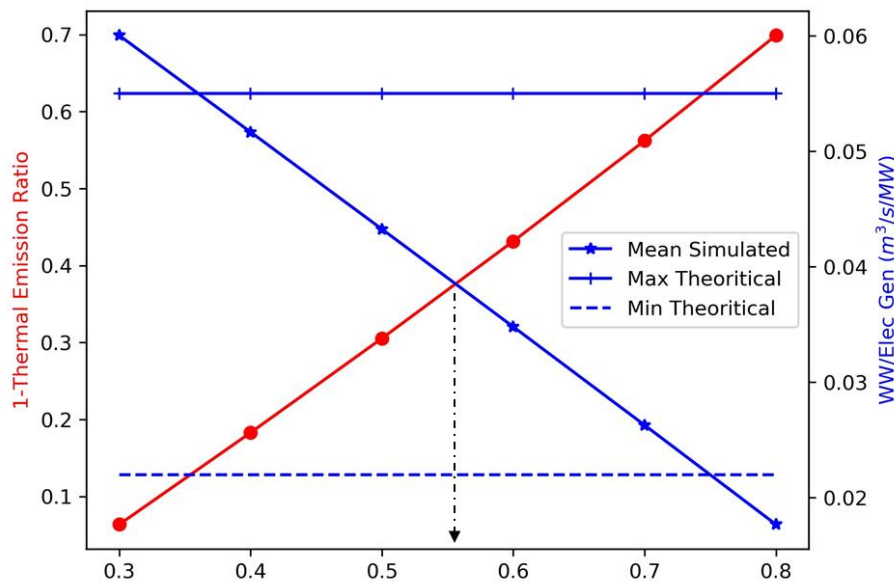


Figure 4.9: Estimation of cooling parameter “ α ” for once-through cooling systems. The two y-axes are normalized to their respective minimum and maximum values

4.5 Results and Discussions

4.5.1 Validations

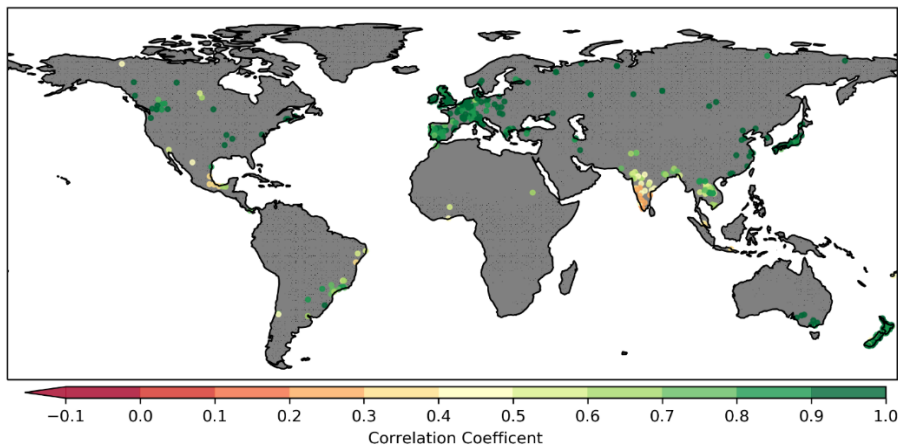


Figure 4.10: Correlation of simulated water temperature with GEMS observation

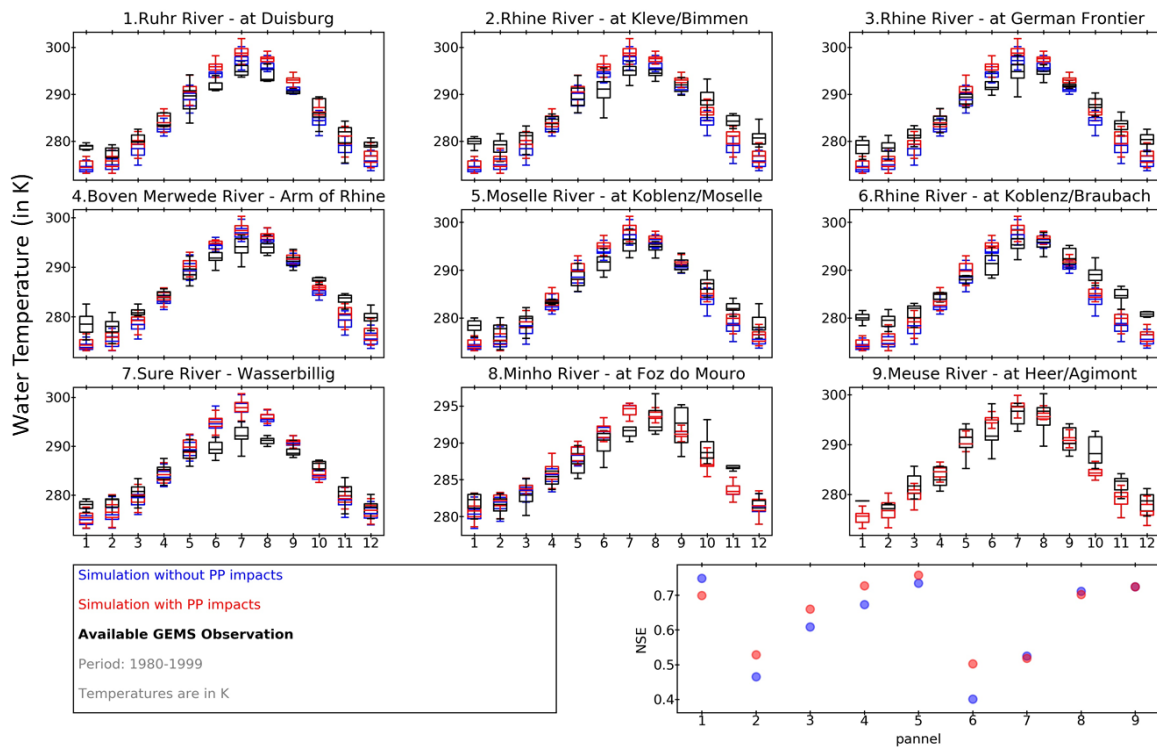


Figure 4.11: Monthly values of observed water temperature (black) and two experiments, with power, plants water withdrawal (red) and return flow and without (blue) for various river catchments in the Rhine-Meuse River basin for available data during 1980-1999. For panel 9, there is no upstream power plant.

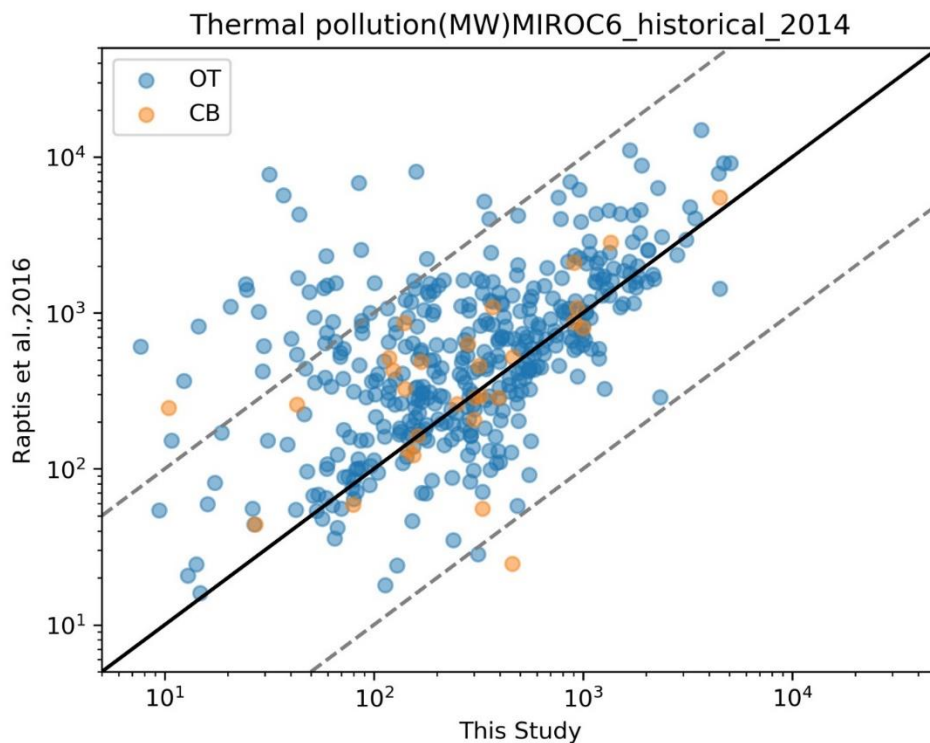


Figure 4.12: Thermal discharge in MW in the current (x-axis) and a previous study (y-axis).

The newly developed power plant model is used to simulate water temperature with anthropogenic impacts and power plant production with different cooling systems. The inclusion of power plant

thermal effluents and water consumption improves the simulation of water temperature, particularly for thermally polluted river basins like Rhine (Fig. 4.11)

The mean annual thermal emissions from each power plant location for OT and CB have been computed and compared against the Raptis et al. dataset (Fig 4.12). The current study tends to underestimate the thermal pollution caused by power plants. This is because the reference data is also modeled data and has errors of its own. Additionally, it doesn't consider the policy regulations for thermal emission standards.

4.5.2 Changes in power production

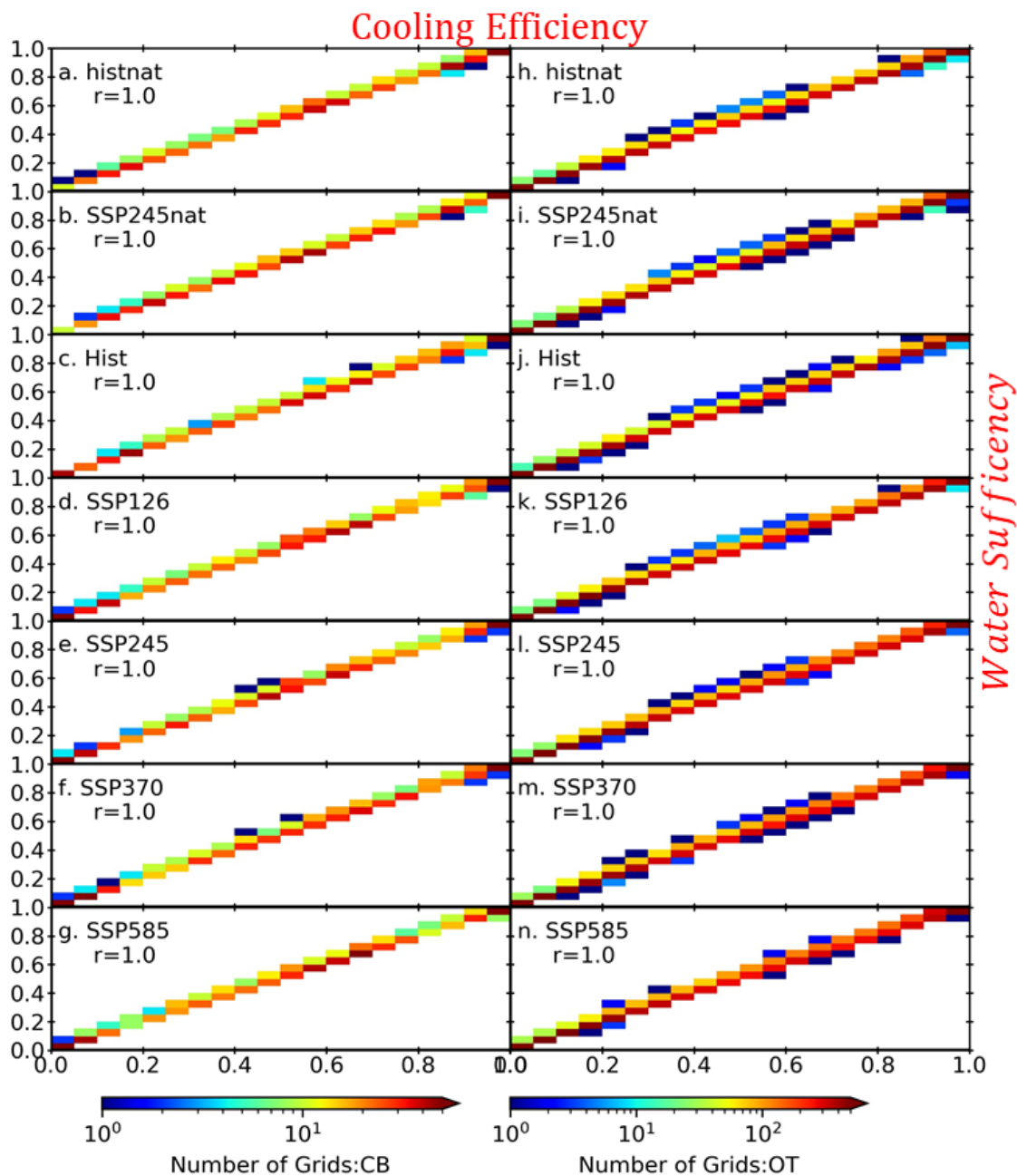


Figure 4.13: Cooling efficiency and water sufficiency of Power plants.

The cooling efficiency of the power plants defines as $\frac{\text{Power Production}}{\text{Generation capacity}}$, is strongly related to the water sufficiency, defined as $\frac{\text{Water Withdrawal}}{\text{Water Demand}}$. There is a perfect correlation between these values. This is mainly because of the nature of the equations used to calculate water demand and power production. Equation 4-2 can be simplified as

$$P_{\text{thermo}} = \frac{\min((\gamma \cdot Q), q) \cdot \rho_w \cdot C_p \cdot \max(\min(Tl_{\text{max}} - T_w), \Delta Tl_{\text{max}}), 0)}{\frac{1 - \eta_{\text{total}}}{\eta_{\text{elec}}} \cdot \lambda \cdot (1 - \alpha) \cdot (1 - \beta) \cdot \omega \cdot EZ}$$

$$= \frac{\min((\gamma \cdot Q), q) \cdot KW}{\lambda \cdot q}$$

As $\lambda = 1$,

$$\frac{P_{\text{thermo}}}{KW} = \frac{\min((\gamma \cdot Q), q)}{q} \quad \text{Equation 4 – 3}$$

$$\text{Cooling efficiency} = \frac{\text{Power Production}}{\text{Generation capacity}} = \frac{\text{Water Withdrawal}}{\text{Water Demand}} \quad \text{Equation 4 – 4}$$

Further,

$$\frac{\text{Water Demand}}{\text{Generation capacity}} = \frac{\text{Water Withdrawal}}{\text{Power Production}} \quad \text{Equation 4 – 5}$$

At a global scale, the total water available for OT is higher in the historical scenario and lower in the natural scenario and higher warming scenario, except for SSP126 (Fig 4.14). In contrast, for CB, the discharge tends to decline in comparison to the historical scenario. It can be noted that OT are located at regions with higher discharge and much lower for CB. Like most places in the world, the inflow water temperature (Inf Temp) for both OT and CB increases with increasing radiative forcing under anthropogenic warming. Also, the inflow temperature is higher for CB than OT. The usage of the cooling towers(%CT use), in the case of CB, that increases with increased radiative forcing, declining the water withdrawal per unit power production(WW/prod) for these locations. In contrast, for OT, WW/Prod increases with increased radiative forcing. Nonetheless, the cooling efficiency (PP Efficiency) of both cooling systems tends to decline in all the future scenarios, with an overall efficiency being higher for OT than CB. Interestingly, for both OT and CB, the average cooling efficiency is higher under SSP370, despite being a higher warming scenario than SSP245 as the water availability increases in SSP370 at the location of the power plants

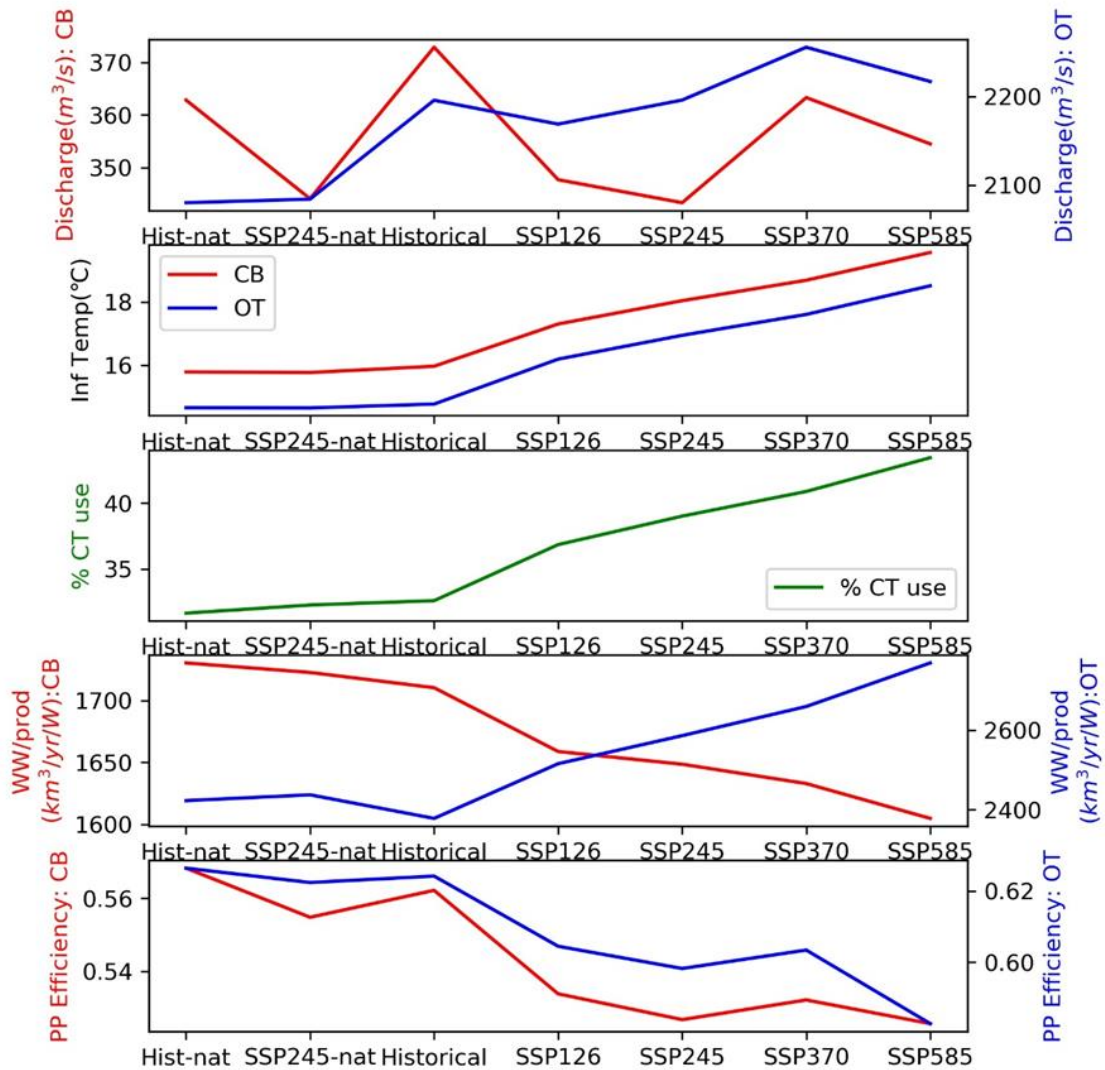


Figure 4.14: Power production under climate change

The results at regional scale differ for certain regions, such as Alaska (OT), Western North America (CB), Tibet (OT), Central Asia (OT), and Southern Asia (CB and OT), where thermal power plants demonstrate an overall improvement in cooling efficiency in warmer future conditions. For Central Europe, the efficiency of OT lowers down to nearly 30% in SSP585 from 50% in the historical scenario on an average. Interestingly, even without anthropogenic greenhouse gas emissions, power production would have declined for Central Europe. Similar trends can be noticed for OT and CB in other regions like Alaska, Northern Europe, and Western Asia, as well as at the global scale.

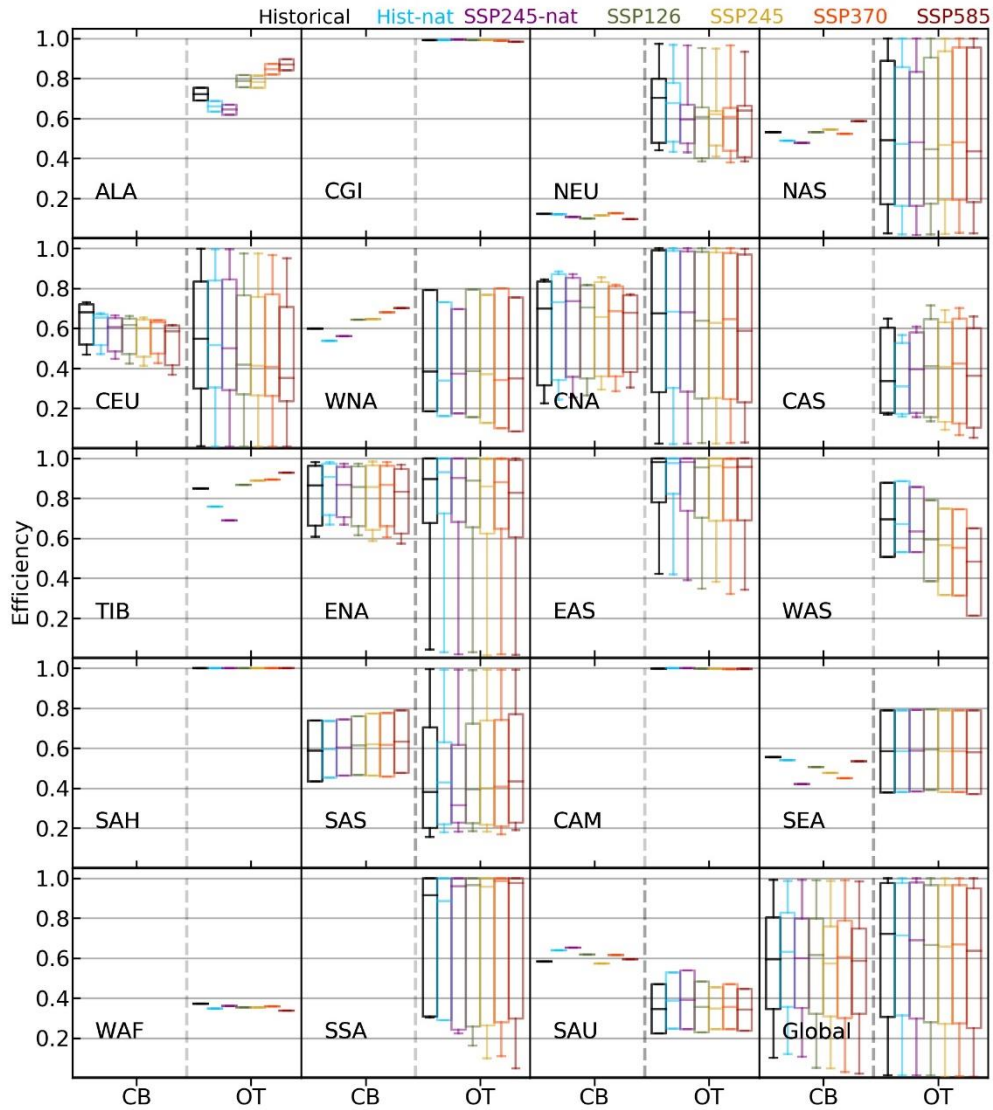


Figure 4.15: Power plant cooling efficiency in different SREX regions.

4.5.3 Power plants under adverse conditions

The adverse conditions such as dry period and combined dry-warm periods tend to increase in the future (Fig 4.16) at most power plant locations. However, for all power plants, the warm period increases with increased radiative forcing for all anthropogenically forced future scenarios. Even under natural climate, the dry period is higher for most of the OT. Figure 4.17 represents the power plant cooling efficiency under such adverse conditions. It can be noted that the efficiency of both OT and CB declines during the dry and dry-warm periods. Additionally, such a decline in efficiency also intensifies in the warmer future, with increased radiative forcing. In the case of warm conditions, OT demonstrates an increase in cooling deficiency, while CB demonstrates an increase in cooling

efficiency compared to their average values. The percentage of cooling tower usage days in a year (%CT use) increases consistently with an increase in radiative forcings.

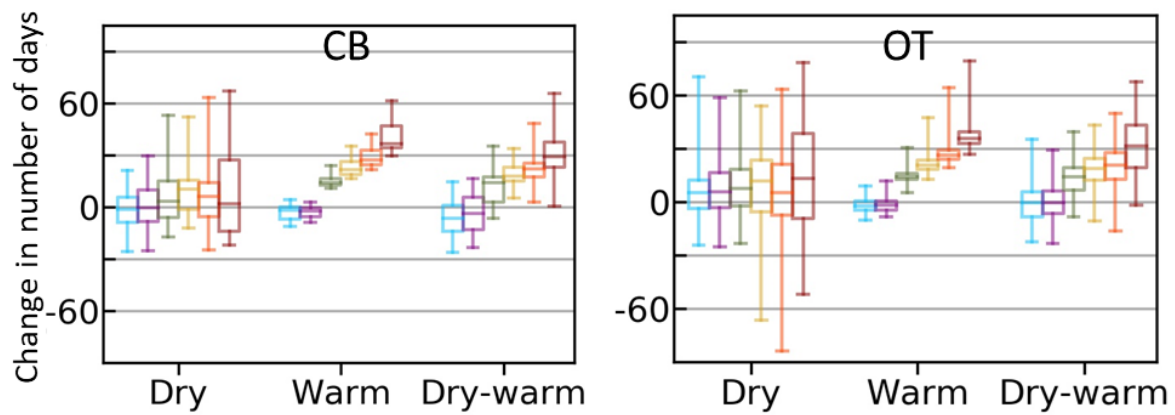


Figure 4.16: Change in frequency of adverse conditions at power plant location.

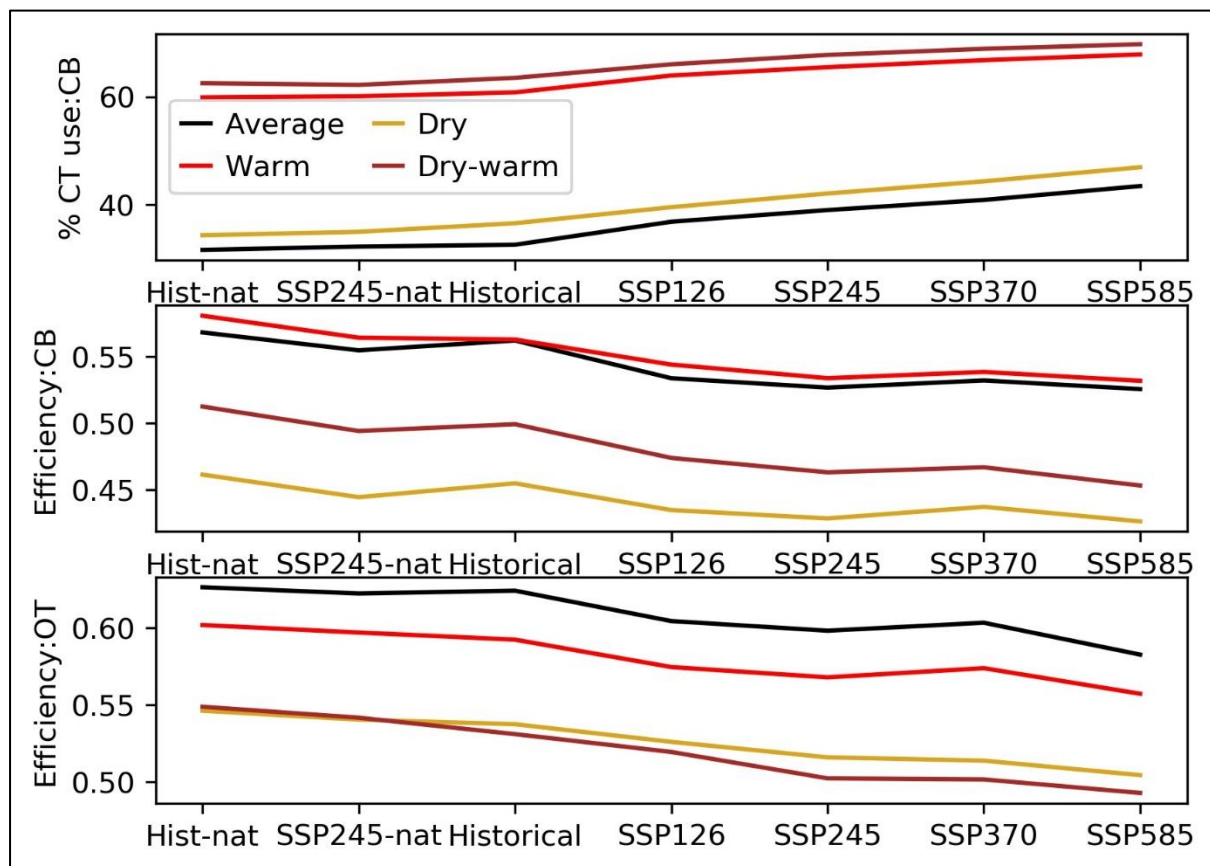


Figure 4.17: Cooling efficiency under adverse conditions

4.5.4 Attribution of reduction in cooling efficiency to HIW

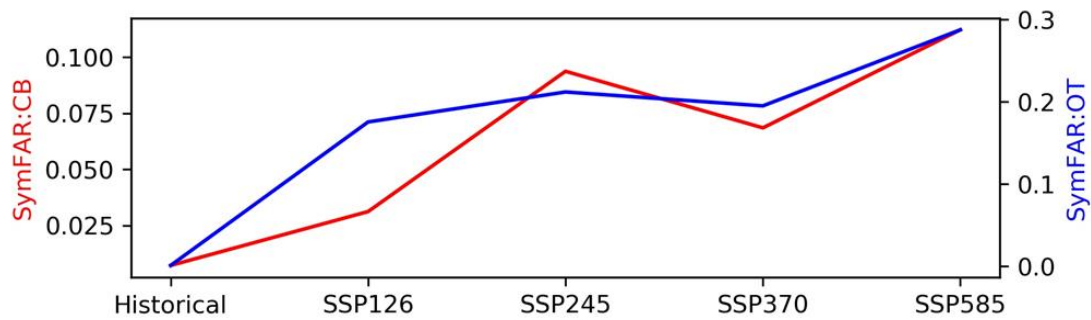


Figure 4.18: The attribution of reduction in cooling efficiency to HIW

The HIW responsible for the reduction in cooling efficiency of OT escalates from nearly zero in the historical period to about 30% under SSP585. Even for CB, this attributed risk increases with radiative forcing, but the risk is very small. It should be noted that the attributed risk is lower in SSP370 compared to SSP245 for OT and CB, which is essentially because of increased water availability in SSP370.

4.5.5 Thermal emissions and thermal pollution caused by power plants

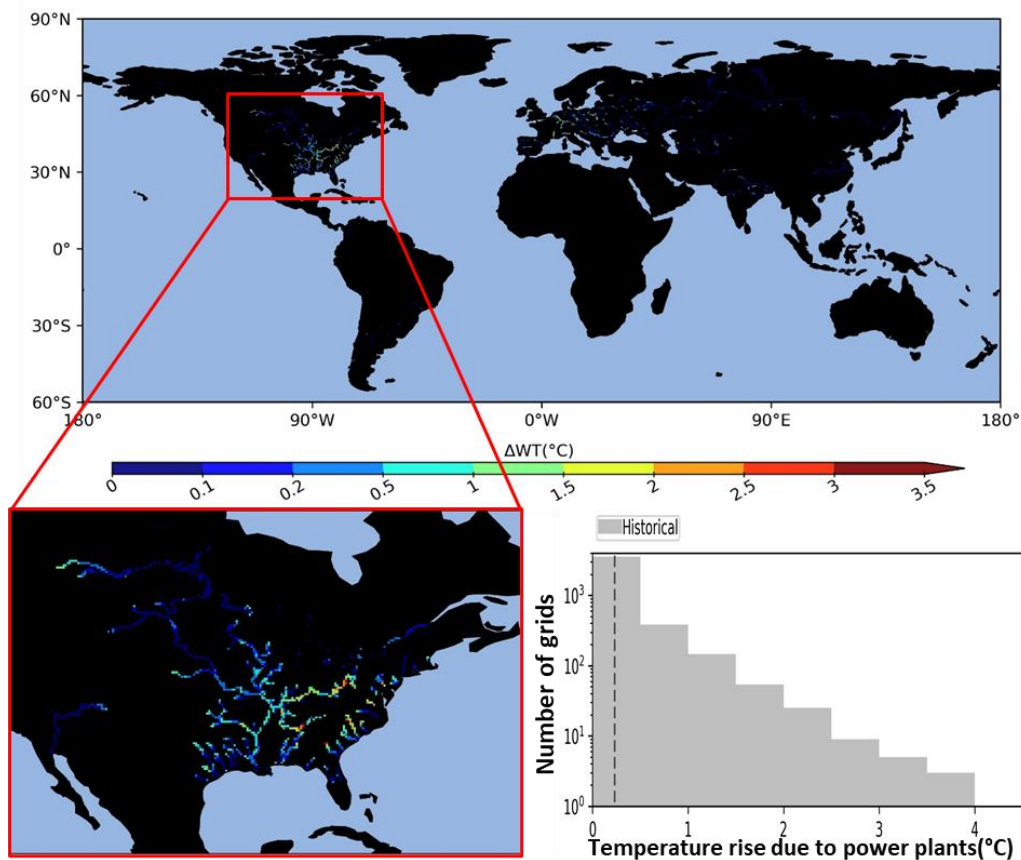


Figure 4.19: Rise in water temperature due to power plant thermal emissions in the historical scenario

The water temperature rises at the point of thermal discharge from power plants, reaching an average value greater than 3.5°C at some grids (Fig. 4.19). However, the impact of such temperature rise declines as the water flows downstream. The annual emission from OT increases with warming but declines in highly warmed SSP585 (Fig. 4.20). In contrast, for CB, the thermal emission declines with increased warming as the usage of cooling towers increases. The total thermal emission from OT is much higher than CB. However, the emission per unit power production remains constant for OT while declines for CB. Despite the differences in OT and CB emission patterns, the water temperature tends to increase for both these locations, compared with the historical scenario. It can be noted that the temperature rise at CB is higher than OT. This is because the flow itself is generally small at the location of CB.

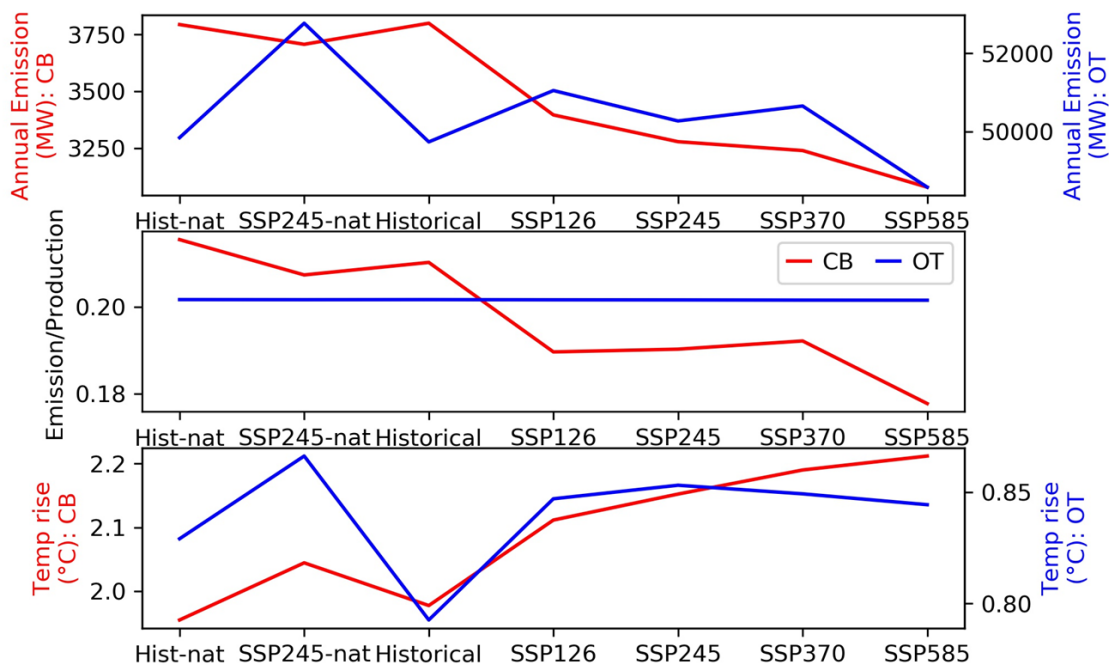


Figure 4.20: Thermal emission and temperature rise at power plant location

Further, the water temperature rise caused by power plants (ΔWT) at any given location to the downstream of power plants may increase or decrease in the future (Fig. 4.21). The number of grids that demonstrate an intensification of ΔWT is higher than that of ones showing a decline in ΔWT , particularly in the higher warming scenario, compared to the historical scenario (Fig. 4.22). This shift in ΔWT (Δ Temperature rise) seems to be related to the fluctuations in discharge changes (caused by power plant water consumption) compared to the historical period (ΔQ_{diff}), as can be seen in figure 4.21. Figure 4.23 depicts the relationship between Δ Temperature rise and ΔQ_{diff} for the grids that are affected by power plant activities. The Δ Temperature rise has a significant negative correlation (p-value of correlation >0.95) with the ΔQ_{diff} . Even though the correlation is not very strong, most grids exhibit an inverse relationship (Fig. 4.23). Additionally, most grid cells show a positive Δ Temperature

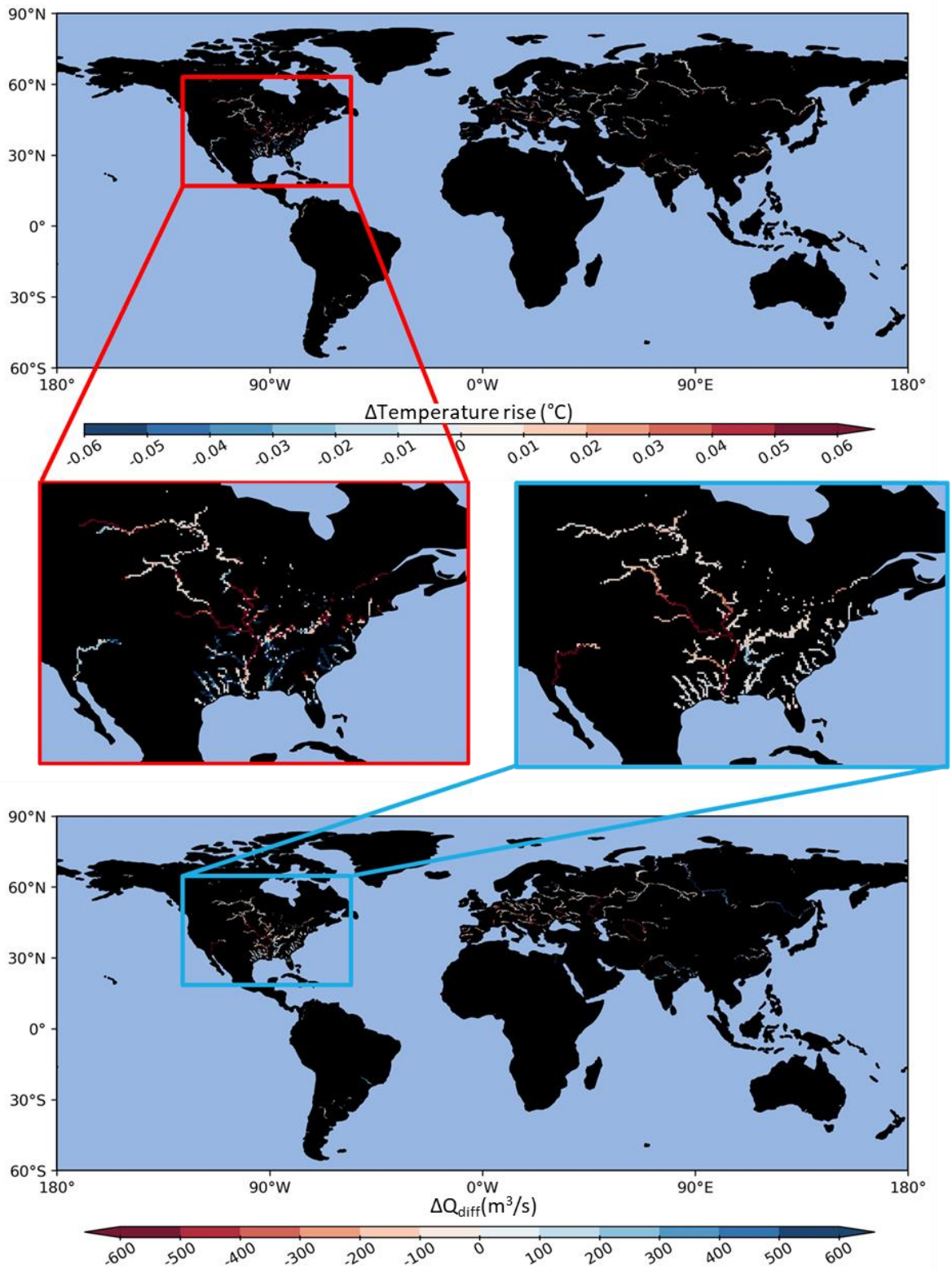


Figure 4.21: Rise in water temperature due to power plants compared to the historical scenario

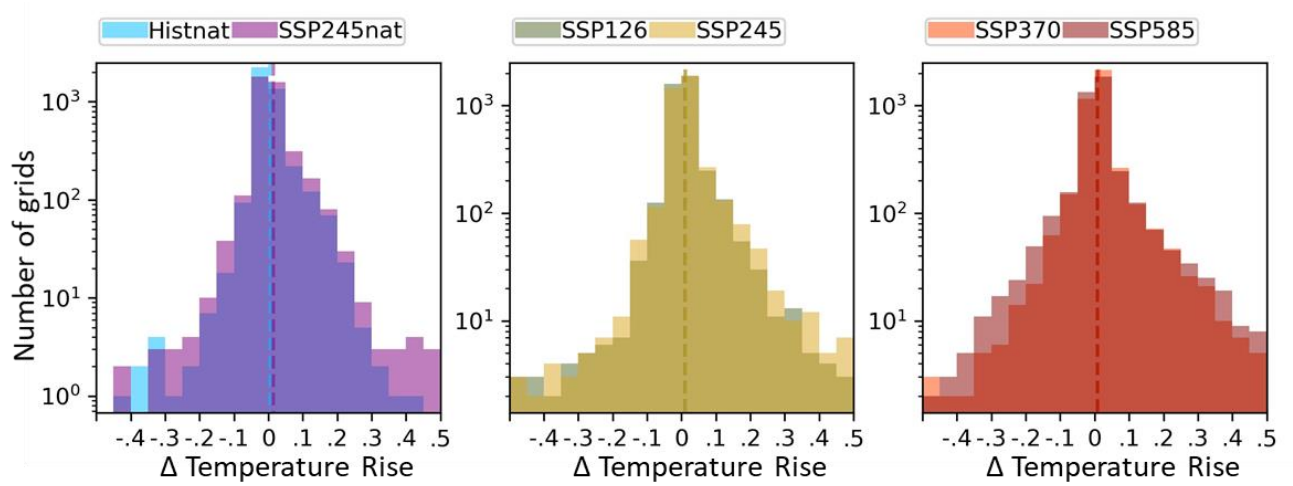


Figure 4.22: Change in water temperature rise caused by power plants (Δ Temperature Rise) at each grid cell when compared against the historical scenario

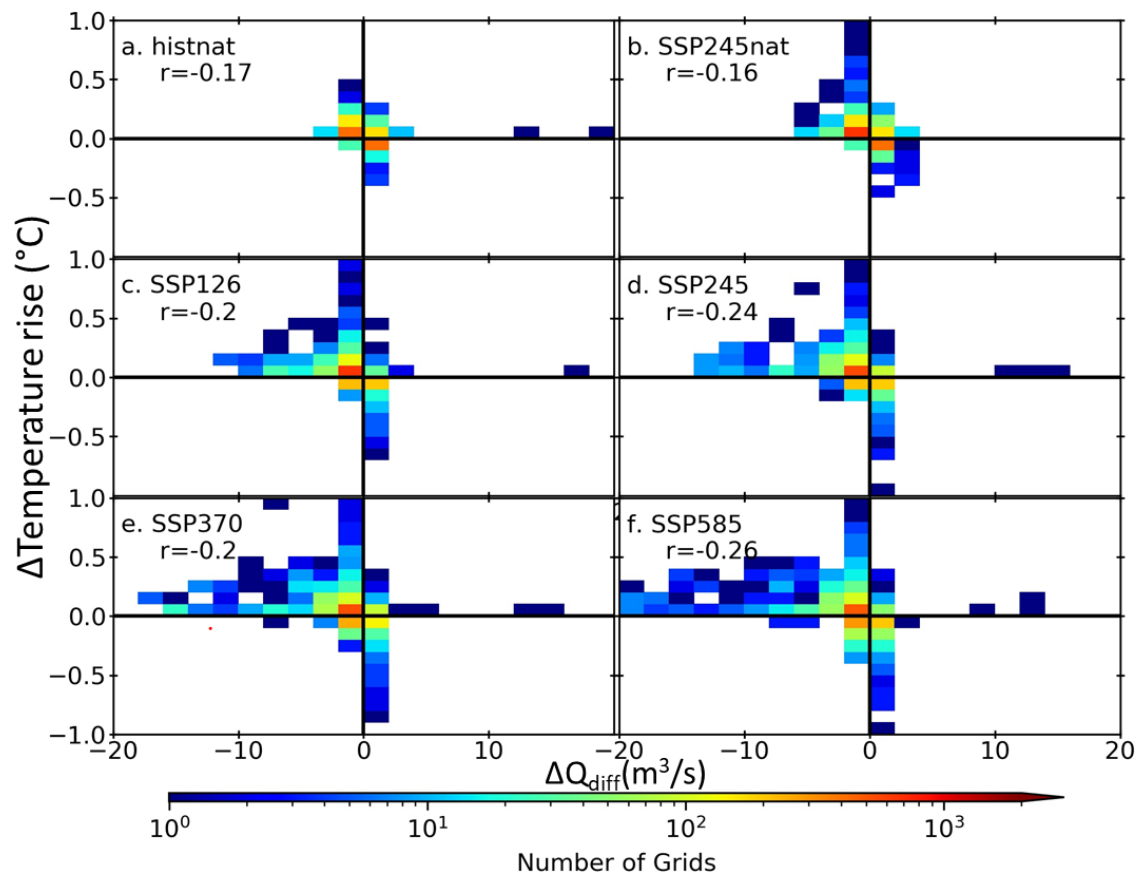


Figure 4.23: Change in temperature rise due to power plants

rise and a negative ΔQ_{diff} , which tends to intensify with increased radiative forcing. Most surprisingly, the temperature rises and decline in discharge are also higher for many grids in the scenarios with natural forcings when compared with the historical period.

4.6 Discussions

The power plant model developed in this study realistically represents the power plant production and thermal emissions even with limited open-source data. It could be possible because of the cooling parameter estimation. Although model calibration provides the short-term benefit of simulation accuracy⁴⁴, parameter estimation enables model application even for power plants with information on just cooling system type¹¹⁹, which can be compared to an ungauged catchment in typical hydrology. This advantage can be utilized in predicting the fate of a proposed power plant at any given location. On the hind side, the accuracy may not be very high as actual cooling parameters are missing, which vary for each power plant. If the cooling parameters are known, the accuracy of both cooling efficiency and thermal emission might improve significantly. Better policy implementations such as dynamic allocation of cooling tower (DACT) in the case of the combined cooling system and an extra allowance of effluent temperature during water shortages and warmer conditions have been incorporated into the model that has been missing in the previous works^{44,51,52,114}. As the model also segregates the power plants based on cooling system types, the impact of DACT can easily be deduced, particularly during the warmer period and water shortages. It should be noted that the usage of a cooling tower also demands a share of electricity production and results in a reduction in the net efficiency of the power production; such operational power costs have not been considered in this study. Reservoir operation and water consumption by other sectors like domestic and agriculture can impact power plants, particularly in the immediate downstream locations of such reservoirs and the point source of water withdrawal.

One interesting finding in this work is the increased power production in SSP370 than SSP245, which is supported by the higher water availability in SSP370. One may argue that water availability is also higher in SSP245, SSP370, and SSP585 for OT compared to the historical scenario, but the power production is still lower. As the radiative forcing increases, both discharge and water temperature increase. An increase in water temperature increases the water demand in the power plants, but as the discharge for some of the power plants, meeting the increased water demand becomes relatively easier than power plants where water availability decreases. If the ratio of water withdrawal to demand (equivalent to cooling efficiency) had superseded its value in the historical scenario, the power production would have increased in SSP245, SSP370, and SSP585, which do not happen. However, the ratio of water withdrawal to demand in SSP370 surpasses that in SSP245, resulting in

such increased efficiency. The risk attribution to HIW also decreases for the reduction in power plant efficiency for SSP370 compared to SSP245 for the same reason. Such phenomenon has not been reported in previous studies as such a large number of future scenarios have never been considered before.

4.7 Conclusions

The power plant model improves the water temperature simulation, particularly in thermally polluted rivers like the Rhine. The separation of analysis for different cooling systems at grid-scale provides new insights into power plant production and thermal emissions in different climatic scenarios. The DACT also proves to make the CB more climate-resilient.

The water temperature rises due to thermal power plants declines as we move downstream of the power plants, as the flow increases. Thus, the acute impacts of temperature rise on the aquatic ecosystem are short-lived on the spatial scale. But it should also be noted that the spatial scale of this analysis is not so small for disregarding such impacts completely.

Both water and energy sectors need investment in mitigation efforts to combat climate change. Installation of cooling tower for DACT in OT is just the beginning of this. Desalination plants need to be installed in coastal areas, advanced wastewater treatment can be adopted to boost the reuse of water, and more efficient cooling systems can be developed to improve the power production and stabilize the water-energy nexus, and at the same time conserve the environment.

4.8 Future Scope

Seasonal scale analysis of the results can provide new insights, such as increased flow in the summer season due to the early melting of river ice. The power plant datasets like CARMA and GEOPP have a wide range of information for thermal power plants and hydro-power plants. Thus, the inclusion of reservoir operation in the power plant model can open gates for hydropower to be included. Also, lakes and reservoirs can be separated from rivers. As the static water availability is much higher in such water bodies, the fluctuations in the power production for power plants using water from these sources can be much smaller. Also, thermal pollution can be more critical in terminal lakes, increasing the water temperature and evaporative losses. Using the lake temperature model alongside the water temperature model (T-CHOIR) can incorporate such research prospects. Last but not least, salmonoid and cyprinoid water considerations and variable environmental flow requirements can improve the implementation of policy frameworks and simulate power plant activities more realistically.

Chapter 5: Conclusion and Future Works

5.1 Synthesis of results and derived conclusions

In the future, as the dry events get elongated (Fig. 2.15), water scarcity would increase, leading to a decline in cooling efficiency for more extended periods in most regions of the world. The cooling efficiency is found to be generally declining during dry periods due to water scarcity, and this decline in efficiency intensifies with warming in future scenarios (Fig. 4.17). This may happen under all anthropogenically warmed future scenarios, at least for the power plants considered in this study, as the number of dry days in a year also increases (Fig. 4.16). In certain regions (Fig. 3.23) like Central Europe and Western Asia, even unplanned power plants may face water scarcity. This would also depend on the capacity of the thermal power plants and the water temperature. The average water temperature (Fig. 3.6) and the number of warm days (Fig. 3.23) increased worldwide at all locations, increasing the demand for cooling water. This rise in water demand would possibly occur in all seasons (Fig. 3.13) for all regions of the world (except Southeast Asia, where water temperature declines for a small proportion of some land area likely due to a substantial increase in runoff).

Additionally, the water temperature rise in the anthropogenically forced worlds intensifies particularly in the summer season (Fig. 3.12), when the water is generally scarce, leading to an increased compounding of the dry-warm period. Such compounding of dry-warm days increases for most regions (Fig. 3.23), particularly at the power plant locations (Fig. 4.16). The cooling efficiency of power plants during such adverse conditions (dry phase, warm phase, and compounded dry-warm phase) tends to be much lower than the average value, particularly for OT. However, efficiency may increase in certain regions like Alaska, given the water sufficiency increases despite rising temperature. Although HIW declines the efficiency of both OT and CB, DACT makes combined cooling more climate-resilient to climate change and also declines the thermal emissions.

Another concern is the increased contrast between dry and wet phases (asymmetry), which intensifies with warming (Fig 2.15). Thus, the power plant production would also have sharper contrast during dry and wet periods. Such fluctuations in power output mean immense pressure on the power grid to maintain a stable supply.

The increased water demand in the future will heavily impact the delicate water-food-energy nexus. As the temperature rises, the agricultural demand for irrigation will also increase, owing to the increased evaporation rates. Drinking water shortages have forced the adoption of desalination in many regions, which is an energy-intensive process^{120,121}. Desalinated water is also being used for irrigation, which is generally expensive but necessary for food production¹²². As the water

temperature and population rises, the competition for water between drinking water, food, and energy will increase.

5.2 Policy Implications for sustained power production

5.2.1 DACT to boost climate resilience and decline the thermal emissions

Installation of cooling towers for once-through systems can improve the cooling efficiency, as cooling tower usage reduces the water withdrawal demand per unit capacity of the power plants and the thermal emission per unit of power production. As the adverse conditions for power plants get intensified, the cooling tower usage would also increase, making the power plant resilient against climate change. Advanced cooling towers, such as the Maisotsenko cycle cooling tower, can reduce the water temperature to a value below the wet-bulb air temperature, which traditional cooling towers cannot achieve¹²³. Forming such advanced combined cooling systems will reduce the water required and control the thermal pollution caused by the power plants. OT in locations like Central Europe and Western Asia (Fig. 3.23), where the number of dry days tends to increase, installing cooling towers for sustained power production is highly recommended. Even regions with an increase in water availability may face water scarcity due to increasing temperature should invest in DACT. Economic comparison for OT with and without the cooling tower can further confirm the feasibility of implementing such cooling towers.

5.2.2 Combining solar photovoltaic power plants with thermal power plants

Thermal power plants are most vulnerable during dry and warm periods due to water shortages when solar radiation is high. The increase in solar radiation is advantageous for solar power plants, particularly solar PV plants. The summer-time PV potential has been reported to increase in the future¹²⁴, particularly in regions with prevalent dry and hot conditions, such as Europe and Eastern Asia. Hence, combining thermal power plants with solar PV plants can boost production during dry and warm periods, particularly for OT, and decline the contrast between wet and dry phases. There are certain regions like Western, Central, and Northern Asia, and Alaska where the PV potential decreases¹²⁴ and this recommendation is not applicable. Improvement in battery technology can further improve the stability of the combined Thermal and PV power plant.

5.2.3 Decentralization of new thermal power plants

As the water temperature rise caused by the power plants diminishes downstream to the power plants, new power plants can be proposed to be installed downstream of power plants in order to meet the rising demand. Increasing the capacity of the existing power plant is although a lucrative option as it is economical. But the environmental policies and cooling water insufficiency might

completely eliminate such options, particularly in regions like Europe and Western North America where temperature rise is high and water is scarce.

5.3 Future scope of the research

Humongous water withdrawals from other sectors such as agriculture can adversely impact downstream power plants. As the radiative forcing, water temperature, and air temperature increase in the future, the higher evaporative losses from agricultural land possibly increase the water demand. Such implications have not been considered in this study and have exciting prospects. The economic analysis of the power plants for converting once-through cooling systems to combined cooling systems is also a possible research area that needs attention. Another critical opportunity is to combine thermal power plants and solar PV plants for stable power production and hydro-economic benefits. The probable location of new power plants can also be determined based on solar potential, cooling efficiency, wind speed, and possible dam height. Under various climatic scenarios, environmental impacts on aquatic ecosystems caused by thermal emissions and water consumption must be examined. The change in river ice mass due to thermal discharge from power plants is also a prospective scope in the future.

5.4 Final Note

Non-renewable power sourced power plants may not be able to sustain in the power market due to increasing water demands, increasing prices for fuel¹²⁵, and decreasing revenues. Renewable energy attracts more incentives from the Govt.^{126–128} and is likely to be a major source of electricity production. However, TPP cannot be eliminated completely due to the limitations of renewable energy in sustained power production.

Sometimes environmental policies may become a burden on the water-energy nexus¹¹¹. It is an established fact that the environment is given the least preference in case of water shortages. There is more political pressure to reduce the supply for industries and domestic purposes, and sacrificing the environment is the path of least resistance¹¹¹. However, the long-term consequences of losing ecological integrity are more detrimental. Optimization of policy, economy, resources, and environmental conservation is necessary to sustain in the future.

Appendix

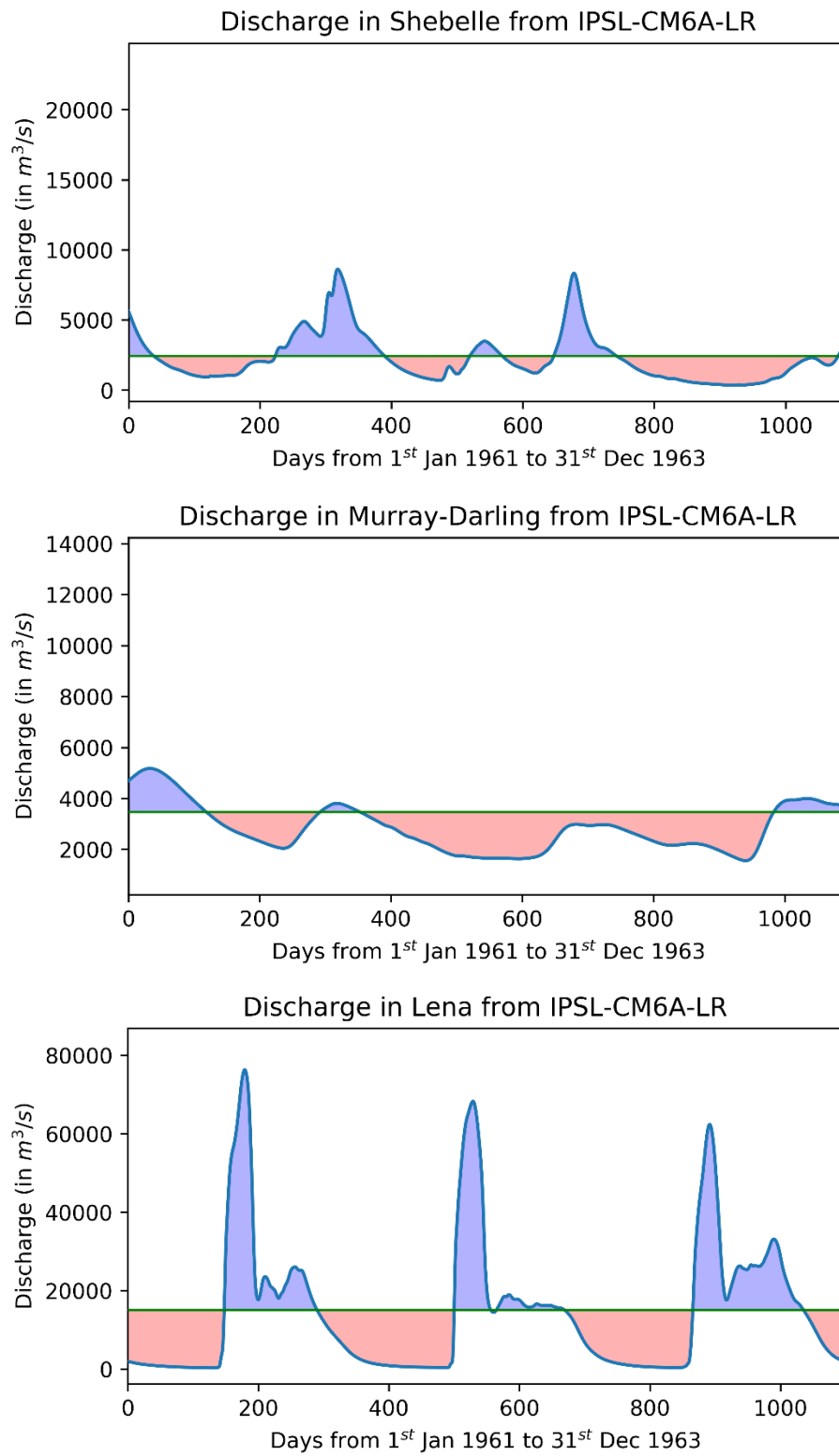


Figure A 1: Wet(blue) and dry(red) phases of river discharge at the outlet, like in fig. 2.2, for Shebelle (small basin), Murray-Darling (Dry basin), and Lena (cold basin).

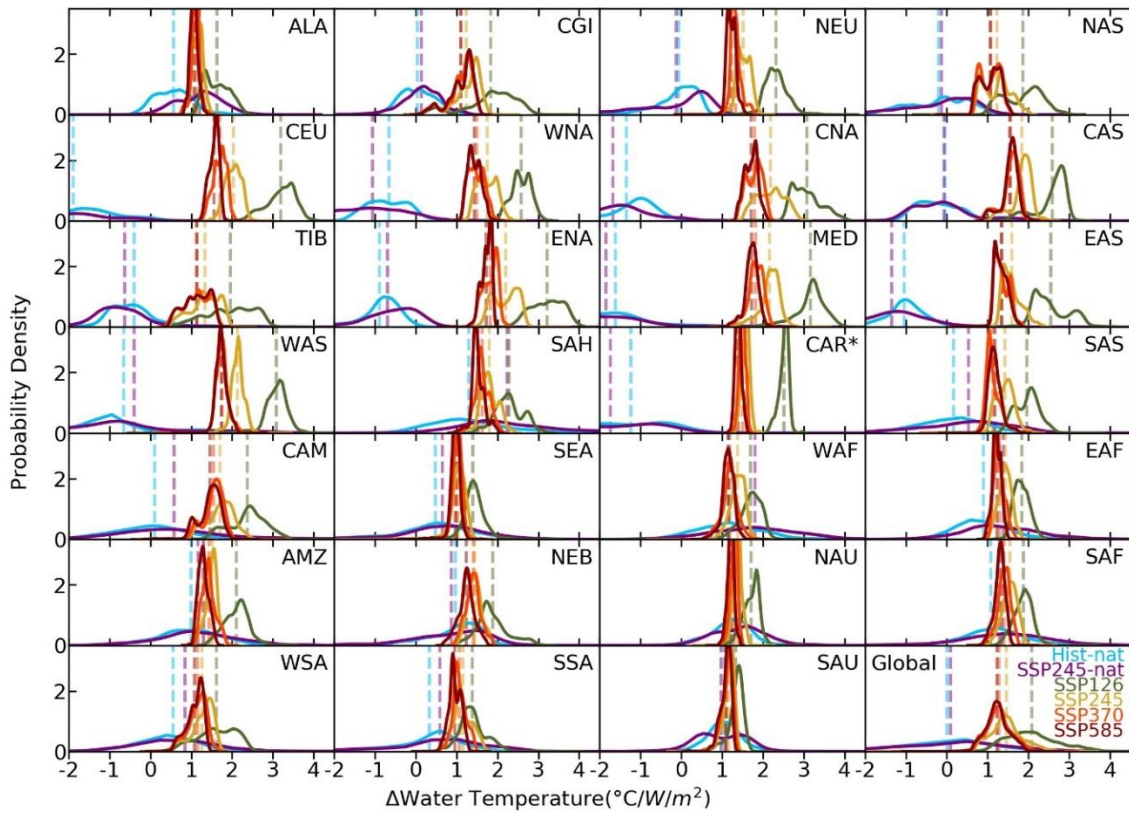


Figure A 2: The spatial variability of sensitivity in the shift in water temperature for different SREX regions

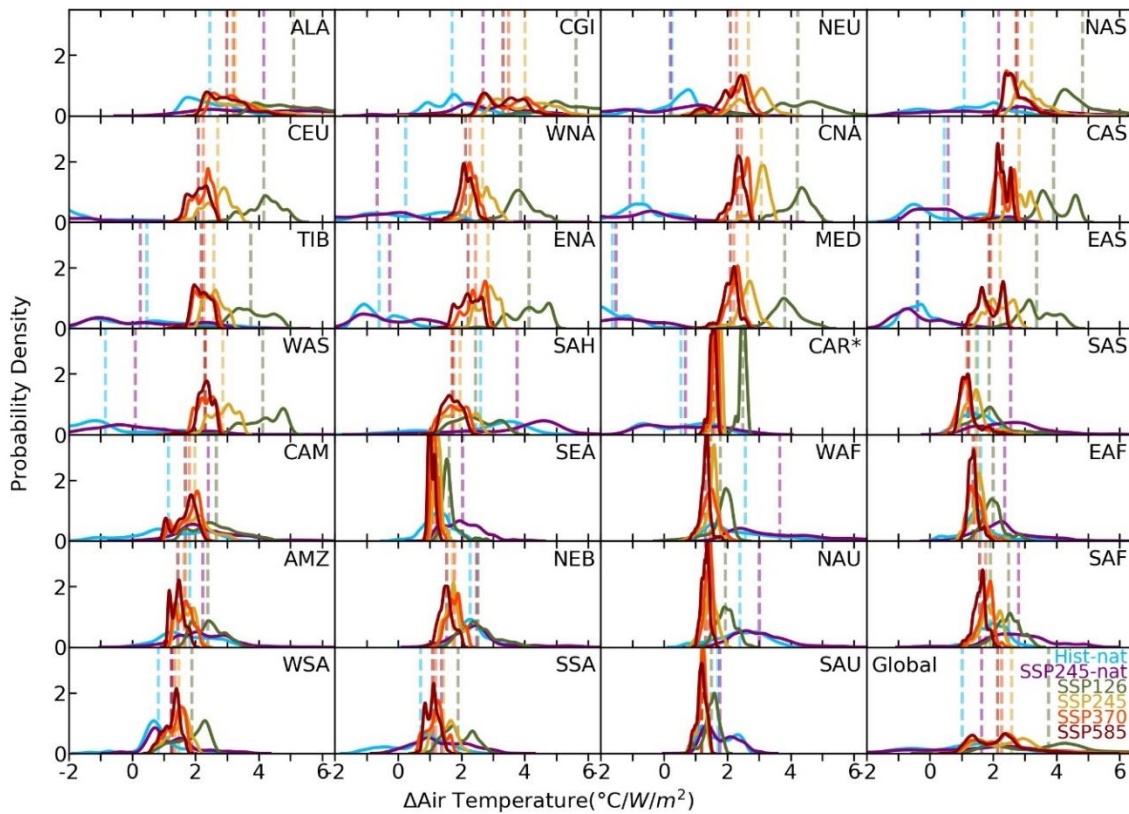


Figure A 3: The spatial variability of sensitivity in the shift in air temperature for different SREX regions

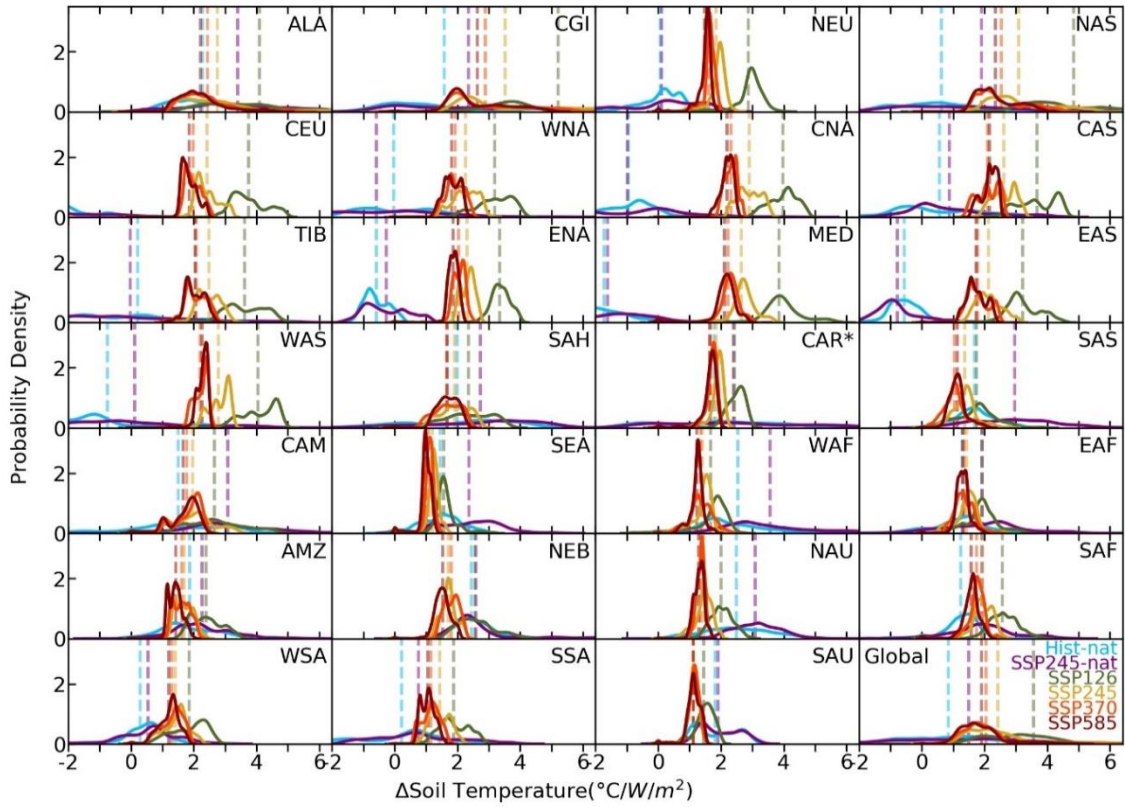


Figure A 4: The spatial variability of sensitivity in the shift in soil temperature for different SREX regions.

Thermal discharge and its decomposition

The daily discharge(Q) and water temperature(WT) for all experiments are used for computing the thermal discharge(TD). Thermal discharge is computed as the amount of heat energy that flows in the water. It is calculated as

$$TD = c_w \cdot \rho_w \cdot Q \cdot WT \quad \text{Equation A1}$$

The changes in thermal discharge are further decomposed into discharge term, water temperature term, and the covariance term as shown below:

$$TD_{\text{expt}} - TD_{\text{hist}} = c_w \cdot \rho_w \cdot \left\{ \begin{aligned} &WT_{\text{hist}} \times (Q_{\text{expt}} - Q_{\text{hist}}) \\ &+ Q_{\text{hist}} \times (WT_{\text{expt}} - WT_{\text{hist}}) \\ &+ (Q_{\text{expt}} - Q_{\text{hist}}) \times (WT_{\text{expt}} - WT_{\text{hist}}) \end{aligned} \right\} \quad \text{Equation A2}$$

The global water temperature rises from 13.9°C in the pre-industrial (1961-1990) era to 14.22°C in the present time (1985-2014) and is expected to rise by another 1.1°C and 3.11°C (compared to present) at the end of the century (2071-2100) for ssp126 and ssp585 future world.

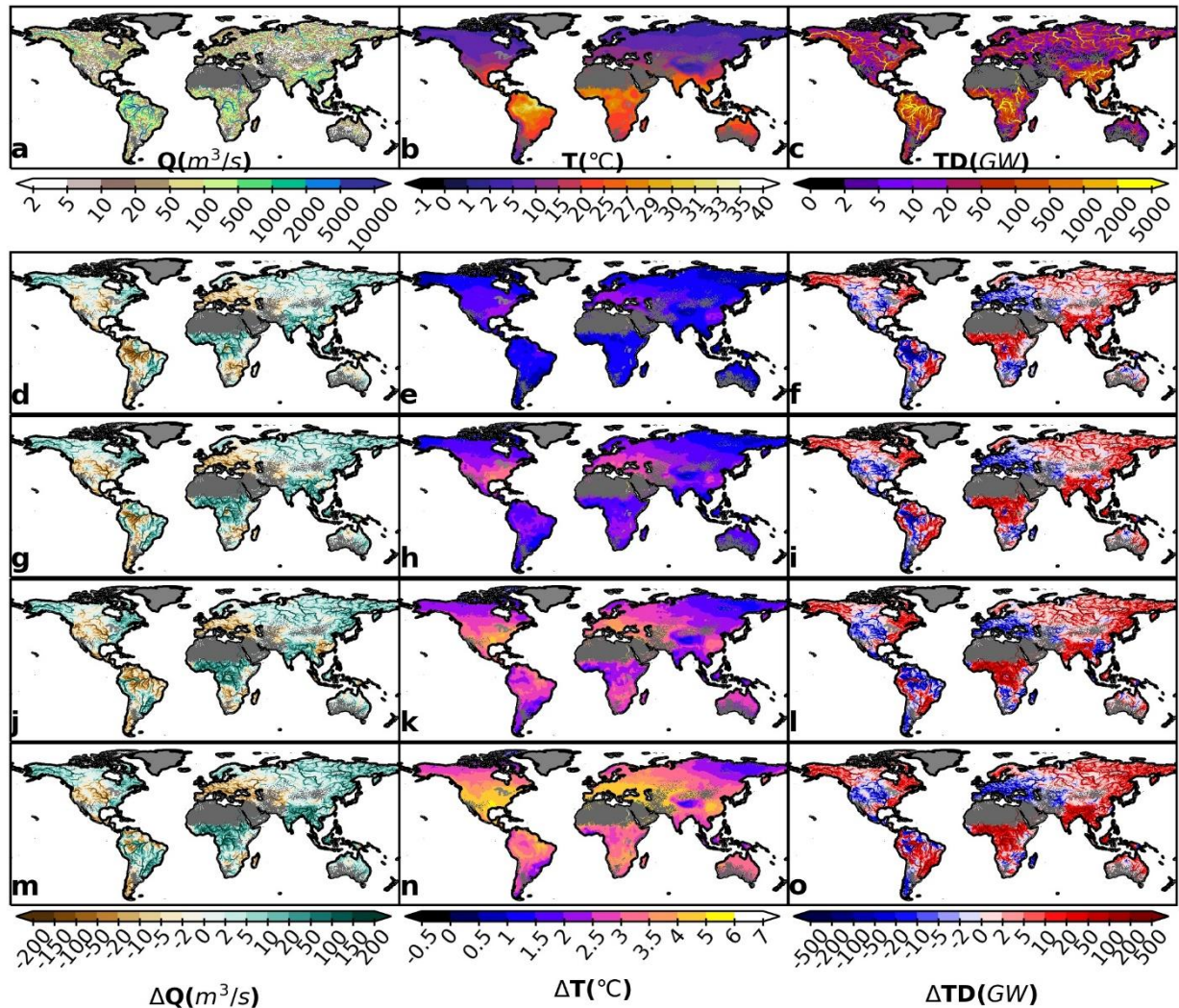


Figure A 5: Discharge (Q), Temperature (T), and Thermal Discharge (TD) for global freshwater flow in the historical scenario are shown in panel a-c. Panels d-f, g-i, j-l, and m-o show the shifts in values in SSP126, SSP245, SSP370, and SSP585 future worlds, respectively compared to historical values for discharge (d, g, j, m), water temperature (e, h, k, l) and thermal discharge (f, i, l, o).

The thermal discharge change when decomposed into discharge term, water temperature term, and covariance term reveal that most increase or decrease in thermal discharge is due to change in discharge. However, the temperature change remains mostly positive. The covariance term, although very small, reflects the regions where discharge changes are consistent with water temperature changes (red regions) and regions of opposite tendencies (blue region).

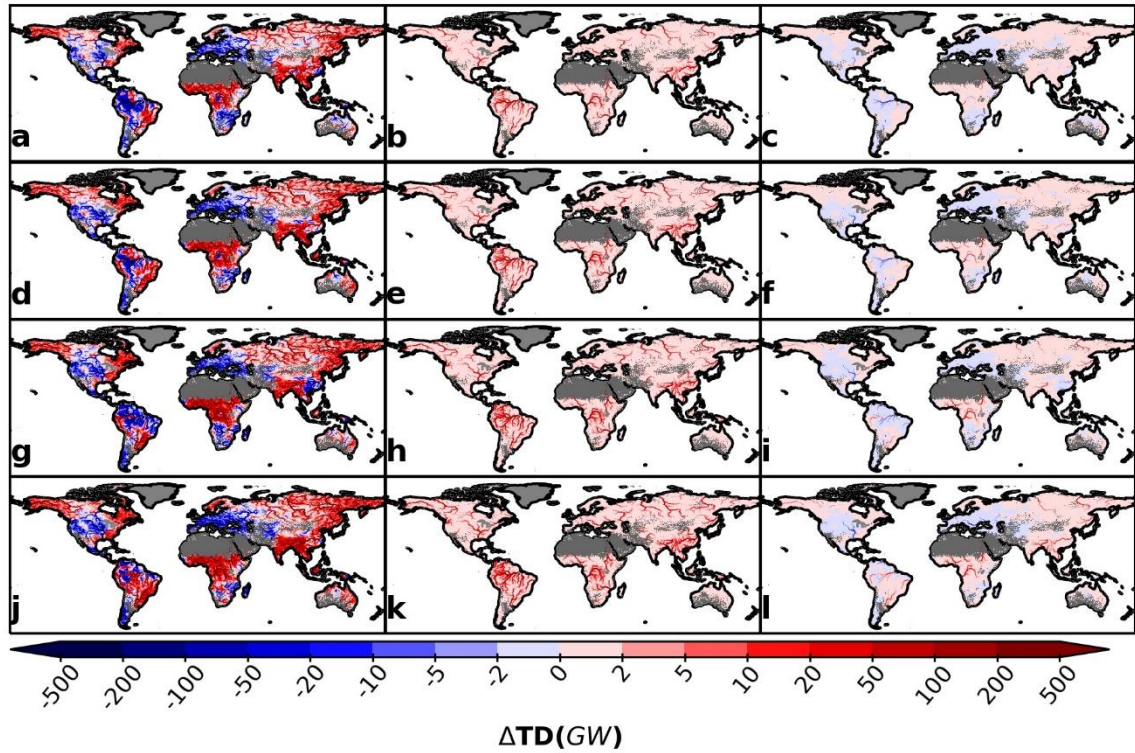


Figure A 6: Changes in thermal discharge are decomposed into three components: change due to change in discharge, change due to change in temperature, and covariance term. Panels a-c, d-f, g-l, and j-l show the decomposed values of change in thermal discharge for SSP126, SSP245, SSP370, and SSP585 future worlds, respectively, for discharge change (a, d, g, j), water temperature change (b, e, h, k) and the co-variance term (c, f, i, l).

Flow from Land to Ocean

The Atlantic Ocean is easily the highest freshwater receiving water body in the form of flow from land. The Pacific Ocean follows the Atlantic Ocean, and the Indian Ocean and Arctic ocean receive a similar amount of flow. However, the Indian Ocean gets the hottest water, and the Arctic Ocean receives the coldest water. The Southern Ocean has a very small flow from the land and is not considered in further analysis. Further, it can be seen that the relative change in discharge and thermal discharge are highest for the Arctic Ocean, while the rise in temperature is highest for the Atlantic Ocean. The Arctic Ocean shows a consistent intensification of changes on the future worlds, while the changes for other oceans show signs of non-intensification, especially for discharge and thermal discharge.

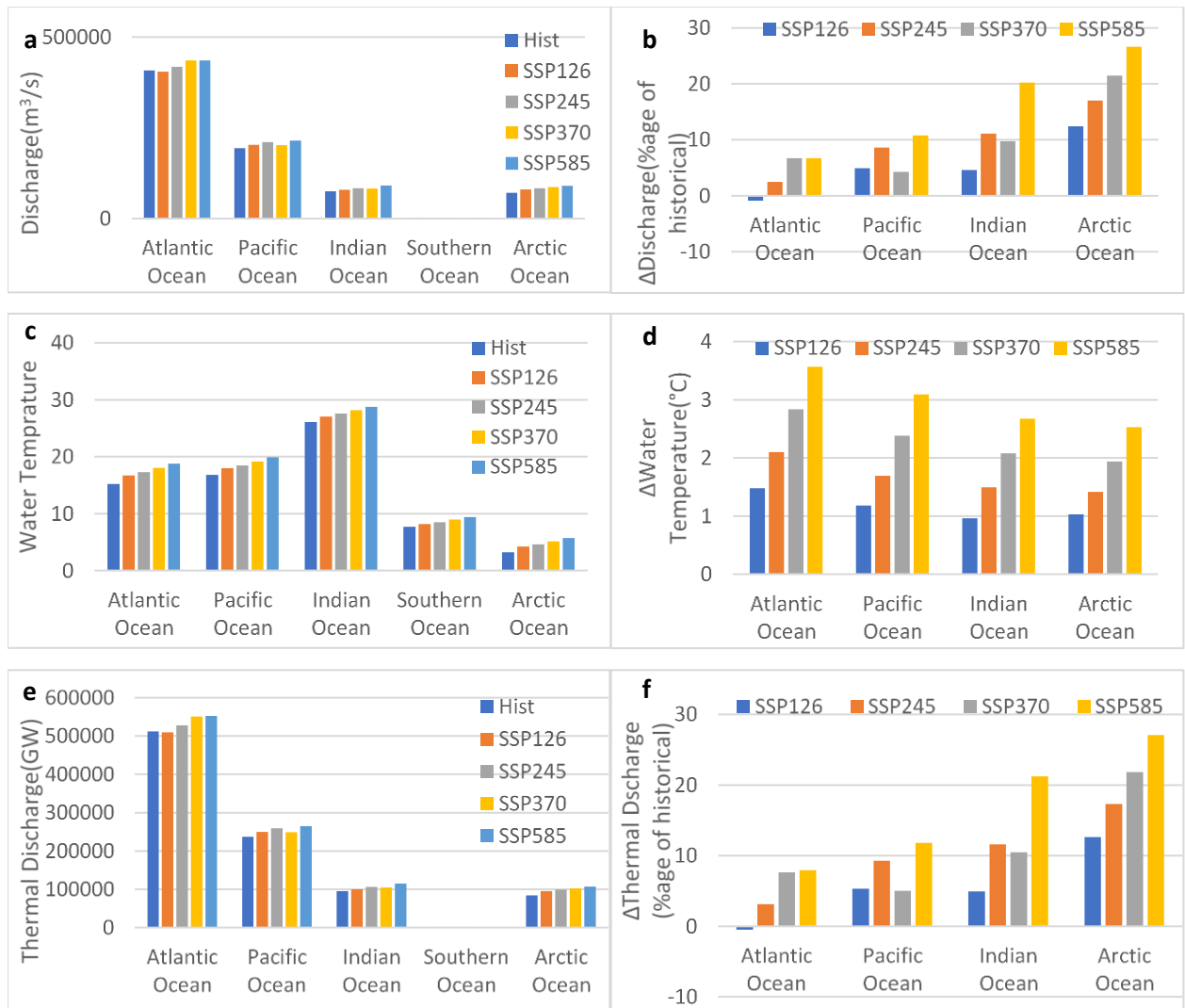


Figure A 7: Flow from land to ocean. The sum of all discharge (a), average water temperature (c), and thermal discharge (e) for all five oceans in the world are shown in the form of a bar chart. The adjacent figures (b, d, and f) show the respective relative change of future scenarios with respect to the historical scenario.

References

1. Jiménez Cisneros, B. E. *et al.* Freshwater resources. *Clim. Chang. 2014 Impacts, Adapt. Vulnerability Part A Glob. Sect. Asp.* 229–270 (2015) doi:10.1017/CBO9781107415379.008.
2. Oki, T. & Kanae, S. Global Hydrological Cycles and World Water Resources. *Science (80-.).* **313**, 1068–1072 (2006).
3. Madakumbura, G. D. *et al.* Event-to-event intensification of the hydrologic cycle from 1.5 °C to a 2 °C warmer world. *Sci. Rep.* **9**, 3483 (2019).
4. Swain, D. L., Langenbrunner, B., Neelin, J. D. & Hall, A. Increasing precipitation volatility in twenty-first-century California. *Nat. Clim. Chang.* **8**, 427–433 (2018).
5. Zhisheng, A. *et al.* Global Monsoon Dynamics and Climate Change. *Annu. Rev. Earth Planet. Sci.* **43**, 29–77 (2015).
6. Trenberth, K. E., Dai, A., Rasmussen, R. M. & Parsons, D. B. The changing character of precipitation. *Bull. Am. Meteorol. Soc.* **84**, 1205–1217+1161 (2003).
7. Trenberth, K. E. Changes in precipitation with climate change. *Clim. Res.* **47**, 123–138 (2011).
8. Nijssen, B., O'donnell, G. M., Hamlet, A. F. & Lettenmaier, D. P. Hydrologic sensitivity of global rivers to climate change. *Clim. Change* **50**, 143–175 (2001).
9. Li, B., Biswas, A., Wang, Y. & Li, Z. Identifying the dominant effects of climate and land use change on soil water balance in deep loessial vadose zone. *Agric. Water Manag.* 106637 (2020) doi:10.1016/j.agwat.2020.106637.
10. Zhang, H. *et al.* Calculation of evapotranspiration in different climatic zones combining the long-term monitoring data with bootstrap method. *Environ. Res.* **191**, 110200 (2020).
11. Arnell, N. W. & Gosling, S. N. The impacts of climate change on river flow regimes at the global scale. *J. Hydrol.* **486**, 351–364 (2013).
12. Nohara, D., Kitoh, A., Hosaka, M. & Oki, T. Impact of climate change on river discharge projected by multimodel ensemble. *J. Hydrometeorol.* **7**, 1076–1089 (2006).

13. Tucker, G. E. & Slingerland, R. Drainage basin responses to climate change. *Water Resour. Res.* **33**, 2031–2047 (1997).
14. Jacob, T., Wahr, J., Pfeffer, W. T. & Swenson, S. Recent contributions of glaciers and ice caps to sea level rise. *Nature* **482**, 514–518 (2012).
15. Martini, M. A., Strelin, J. A., Flores, E., Astini, R. A. & Kaplan, M. R. Recent climate warming and the Varas rock glacier activity, Cordillera Oriental, Central Andes of Argentina. *GeoResJ* **14**, 67–79 (2017).
16. Tagliaferro, M., Miserendino, M. L., Liberoff, A., Quiroga, A. & Pascual, M. Dams in the last large free-flowing rivers of Patagonia, the Santa Cruz River, environmental features, and macroinvertebrate community. *Limnologica* **43**, 500–509 (2013).
17. Koutsoyiannis, D. Revisiting the global hydrological cycle: Is it intensifying? *Hydrol. Earth Syst. Sci.* **24**, 3899–3932 (2020).
18. Vermeer, M. & Rahmstorf, S. Global sea level linked to global temperature. *Proc. Natl. Acad. Sci.* **106**, 21527–21532 (2009).
19. Cazenave, A. & Nerem, R. S. Present day sea level change: observations and causes. *Rev. Geophys.* **42**, 1–20 (2004).
20. Meehl, G. A. *et al.* How much more global warming and sea level rise? *Science (80-.)*. **307**, 1769–1772 (2005).
21. DeConto, R. M. & Pollard, D. Contribution of Antarctica to past and future sea-level rise. *Nature* **531**, 591–597 (2016).
22. Schuerch, M. *et al.* Future response of global coastal wetlands to sea-level rise. *Nature* **561**, 231–234 (2018).
23. Stuart-Smith, J. *et al.* Conservation challenges for the most threatened family of marine bony fishes (handfishes: Brachionichthyidae). *Biol. Conserv.* **252**, 108831 (2020).
24. Trubovitz, S., Lazarus, D., Renaudie, J. & Noble, P. J. Marine plankton show threshold extinction response to Neogene climate change. *Nat. Commun.* **11**, 5069 (2020).
25. Trisos, C. H., Merow, C. & Pigot, A. L. The projected timing of abrupt ecological disruption

- from climate change. *Nature* **580**, 496–501 (2020).
26. Hirabayashi, Y. *et al.* Global flood risk under climate change. *Nat. Clim. Chang.* **3**, 816–821 (2013).
 27. Hirabayashi, Y., Kanae, S., Emori, S., Oki, T. & Kimoto, M. Global projections of changing risks of floods and droughts in a changing climate Global projections of changing risks of floods and droughts in a changing climate. *Atmos. Environ.* 37–41 (2010).
 28. Scussolini, P. *et al.* Global River Discharge and Floods in the Warmer Climate of the Last Interglacial. *Geophys. Res. Lett.* **47**, 1–12 (2020).
 29. Wang, L., Yuan, X., Xie, Z., Wu, P. & Li, Y. Increasing flash droughts over China during the recent global warming hiatus. *Sci. Rep.* **6**, 1–8 (2016).
 30. Yuan, X. *et al.* Anthropogenic shift towards higher risk of flash drought over China. *Nat. Commun.* **10**, 1–8 (2019).
 31. Osman, M. *et al.* Flash drought onset over the Contiguous United States: Sensitivity of inventories and trends to quantitative definitions. *Hydrol. Earth Syst. Sci. Discuss.* 1–21 (2020) doi:10.5194/hess-2020-385.
 32. Pendergrass, A. G. *et al.* Flash droughts present a new challenge for subseasonal-to-seasonal prediction. *Nat. Clim. Chang.* **10**, 191–199 (2020).
 33. Zscheischler, J. *et al.* Future climate risk from compound events. *Nat. Clim. Chang.* **8**, 469–477 (2018).
 34. Otto, F. E. L. *et al.* Towards an inventory of the impacts of human-induced climate change. *Bull. Am. Meteorol. Soc.* 1–17 (2020) doi:10.1175/bams-d-20-0027.1.
 35. Running, S. W. Is global warming causing more, larger wildfires? *Science (80-.)*. **313**, 927–928 (2006).
 36. Westerling, A. L., Hidalgo, H. G., Cayan, D. R. & Swetnam, T. W. Warming and earlier spring increase Western U.S. forest wildfire activity. *Science (80-.)*. **313**, 940–943 (2006).
 37. Montzka, S. A., Dlugokencky, E. J. & Butler, J. H. Non-CO₂ greenhouse gases and climate change. *Nature* **476**, 43–50 (2011).

38. Doll, Julie E. and Barański, M. Greenhouse gas basics. 6–7 (2011).
39. Booij, M. J., Schipper, T. C. & Marhaento, H. Attributing changes in streamflow to land use and climate change for 472 catchments in australia and the United States. *Water (Switzerland)* **11**, (2019).
40. Stocker, T. F. *et al.* Climate change 2013 the physical science basis: Working Group I contribution to the fifth assessment report of the intergovernmental panel on climate change. *Clim. Chang. 2013 Phys. Sci. Basis Work. Gr. I Contrib. to Fifth Assess. Rep. Intergov. Panel Clim. Chang.* **9781107057**, 1–1535 (2013).
41. Wang, Z., Jiang, Y., Wan, H., Yan, J. & Zhang, X. Toward Optimal Fingerprinting in Detection and Attribution of Changes in Climate Extremes. *J. Am. Stat. Assoc.* **0**, 1–23 (2020).
42. Stott, P. A. *et al.* Detection and attribution of climate change: A regional perspective. *Wiley Interdiscip. Rev. Clim. Chang.* **1**, 192–211 (2010).
43. Mirle, K. *et al.* Detection and attribution of climate change: From global to regional. *Clim. Chang. 2013 Phys. Sci. Basis Work. Gr. I Contrib. to Fifth Assess. Rep. Intergov. Panel Clim. Chang.* **9781107057**, 867–952 (2013).
44. Liu, S. *et al.* Global river water warming due to climate change and anthropogenic heat emission. *Glob. Planet. Change* **193**, 103289 (2020).
45. Van Vliet, M. T. H., Ludwig, F., Zwolsman, J. J. G., Weedon, G. P. & Kabat, P. Global river temperatures and sensitivity to atmospheric warming and changes in river flow. *Water Resour. Res.* **47**, (2011).
46. Van Vliet, M. T. H. *et al.* Global river discharge and water temperature under climate change. *Glob. Environ. Chang.* **23**, 450–464 (2013).
47. Carpenter, S. R., Fisher, S. G., Grimm, N. B. & Kitchell, J. F. Global Change and Freshwater Ecosystems. *Annu. Rev. Ecol. Syst.* **23**, 119–139 (1992).
48. Martin, B. T. *et al.* The biophysical basis of thermal tolerance in fish eggs: Thermal tolerance in fish eggs. *Proc. R. Soc. B Biol. Sci.* **287**, (2020).
49. Caissie, D. The thermal regime of rivers: A review. *Freshw. Biol.* **51**, 1389–1406 (2006).

50. Raptis, C. E. & Pfister, S. Global freshwater thermal emissions from steam-electric power plants with once-through cooling systems. *Energy* **97**, 46–57 (2016).
51. Gjorgiev, B. & Sansavini, G. Electrical power generation under policy constrained water-energy nexus. *Appl. Energy* **210**, 568–579 (2018).
52. Van Vliet, M. T. H., Wiberg, D., Leduc, S. & Riahi, K. Power-generation system vulnerability and adaptation to changes in climate and water resources. *Nat. Clim. Chang.* **6**, 375–380 (2016).
53. Raptis, C. E., Van Vliet, M. T. H. & Pfister, S. Global thermal pollution of rivers from thermoelectric power plants. *Environ. Res. Lett.* **11**, 2–4 (2016).
54. Gjorgiev, B. & Sansavini, G. Water-energy nexus: Impact on electrical energy conversion and mitigation by smart water resources management. *Energy Convers. Manag.* **148**, 1114–1126 (2017).
55. Langenbrunner, B. Power plants warm rivers. *Nat. Clim. Chang.* **10**, 888 (2020).
56. Tavakolifar, H., Shahghasemi, E. & Nazif, S. Evaluation of climate change impacts on extreme rainfall events characteristics using a synoptic weather typing-based daily precipitation downscaling model. *J. Water Clim. Chang.* **8**, 441–455 (2017).
57. Eyring, V. *et al.* Overview of the Coupled Model Intercomparison Project Phase 6 (CMIP6) experimental design and organization. *Geosci. Model Dev.* **9**, 1937–1958 (2016).
58. Moss, R. H. *et al.* The next generation of scenarios for climate change research and assessment. *Nature* **463**, 747–756 (2010).
59. O'Neill, B. C. *et al.* The roads ahead: Narratives for shared socioeconomic pathways describing world futures in the 21st century. *Glob. Environ. Chang.* **42**, 169–180 (2017).
60. Meinshausen, M. *et al.* The SSP greenhouse gas concentrations and their extensions to 2500. *Geosci. Model Dev. Discuss.* 1–77 (2019) doi:10.5194/gmd-2019-222.
61. Fanchiotti, M., Dash, J., Tompkins, E. L. & Hutton, C. W. The 1999 super cyclone in Odisha, India: A systematic review of documented losses. *Int. J. Disaster Risk Reduct.* **51**, 101790 (2020).

62. Das, S. & DSouza, N. M. Identifying the local factors of resilience during cyclone Hudhud and Phailin on the east coast of India. *Ambio* **49**, 950–961 (2020).
63. Bala, S. K. & Pattanayak, S. K. Very Severe Cyclonic Storm “Titli”: Impact on Indian Power System. *2019 IEEE 1st Int. Conf. Energy, Syst. Inf. Process. ICESIP 2019* 4–9 (2019) doi:10.1109/ICESIP46348.2019.8938249.
64. Nandi, S. Tracking Cyclone the Fani & Tackling the Aftermath. *Sci. Report.* 43–44 (2019).
65. Patel, S. K. Community-level assessment of floods and cyclones in coastal Odisha, India: Impact, resilience, and implications. (2018).
66. Walch, C. Adaptive governance in the developing world: disaster risk reduction in the State of Odisha, India. *Clim. Dev.* **11**, 238–252 (2019).
67. Mohanty, S. K., Chatterjee, R. & Shaw, R. Building resilience of critical infrastructure: A case of impacts of cyclones on the power sector in Odisha. *Climate* **8**, (2020).
68. Mommen, B., Roy, D. & Sethi, J. Resilient against the elements : the preparedness and response to cyclone ‘ Phailin ’ by the state of Odisha , India. *Sustain. water Sanit. Serv. all a fast Chang. world 37th WEDC Int. Conf.* 1–6 (2014).
69. Hornborg, A. Beyond the image of covid-19 as nature’s revenge: Understanding globalized capitalism through an epidemiology of money. *Sustain.* **13**, (2021).
70. Access to Energy is at the Heart of Development.
<https://www.worldbank.org/en/news/feature/2018/04/18/access-energy-sustainable-development-goal-7>.
71. Li, J., Wang, Z., Wu, X., Guo, S. & Chen, X. Flash droughts in the Pearl River Basin, China: Observed characteristics and future changes. *Sci. Total Environ.* **707**, 136074 (2020).
72. Christian, J. I. *et al.* A methodology for flash drought identification: Application of flash drought frequency across the United States. *J. Hydrometeorol.* **20**, 833–846 (2019).
73. Christian, J. I., Basara, J. B., Hunt, E. D., Otkin, J. A. & Xiao, X. Flash drought development and cascading impacts associated with the 2010 Russian heatwave. *Environ. Res. Lett.* **15**, (2020).
74. Jin, C. *et al.* The 2012 Flash Drought Threatened US Midwest Agroecosystems. *Chinese Geogr.*

- Sci.* **29**, 768–783 (2019).
75. Nguyen, H. *et al.* Using the evaporative stress index to monitor flash drought in Australia. *Environ. Res. Lett.* **14**, (2019).
 76. Sun, Q., Miao, C. & Duan, Q. Projected changes in temperature and precipitation in ten river basins over China in 21st century. *Int. J. Climatol.* **35**, 1125–1141 (2015).
 77. Yamazaki, D., Kanae, S., Kim, H. & Oki, T. A physically based description of floodplain inundation dynamics in a global river routing model. *Water Resour. Res.* **47**, 1–21 (2011).
 78. Tokuda, D., Kim, H., Yamazaki, D. & Oki, T. Development of a Global River Water Temperature Model Considering Fluvial Dynamics and Seasonal Freeze-Thaw Cycle. *Water Resour. Res.* 1366–1383 (2019) doi:10.1029/2018WR023083.
 79. Oki, T. & Kim, H. Macroscale Hydrological Modeling and Global Water Balance. *Terr. Water Cycle Clim. Chang. Nat. Human-Induced Impacts* 1–16 (2016) doi:10.1002/9781118971772.ch1.
 80. Dai, A., Qian, T., Trenberth, K. E. & Milliman, J. D. Changes in continental freshwater discharge from 1948 to 2004. *J. Clim.* **22**, 2773–2792 (2009).
 81. Gerten, D., Rost, S., von Bloh, W. & Lucht, W. Causes of change in 20th century global river discharge. *Geophys. Res. Lett.* **35**, 1–5 (2008).
 82. Trenberth, K. E. Conceptual framework for changes of extremes of the hydrological cycle with climate change. *Climatic Change* vol. 42 327–339 (1999).
 83. Allen, M. R. & Ingram, W. J. Constraints on future changes in climate and the hydrologic cycle. *Nature* **419**, (2002).
 84. Giorgi, F. *et al.* Higher hydroclimatic intensity with global warming. *J. Clim.* **24**, 5309–5324 (2011).
 85. Padrón, R. S. *et al.* Observed changes in dry-season water availability attributed to human-induced climate change. *Nat. Geosci.* **13**, 477–481 (2020).
 86. Zhang, X., Tang, Q., Liu, X., Leng, G. & Di, C. Nonlinearity of Runoff Response to Global Mean Temperature Change Over Major Global River Basins. *Geophys. Res. Lett.* **45**, 6109–6116

- (2018).
87. Déry, S. J. & Wood, E. F. Decreasing river discharge in northern Canada. *Geophys. Res. Lett.* **32**, 1–4 (2005).
 88. Gudmundsson, L. & et al. Globally observed trends in mean and extreme river flow attributed to man-made climate change. *Science (80-.)*. **1162**, 1159–1162 (2019).
 89. Konapala, G., Mishra, A. K., Wada, Y. & Mann, M. E. Climate change will affect global water availability through compounding changes in seasonal precipitation and evaporation. *Nat. Commun.* **11**, 1–10 (2020).
 90. Christidis, N. & Stott, P. A. The influence of anthropogenic climate change on wet and dry summers in Europe. *Sci. Bull.* **66**, 813–823 (2021).
 91. Changes in Flood Risk in Europe. *Changes in Flood Risk in Europe* (2019) doi:10.1201/b12348.
 92. Easterling, D. R., Kunkel, K. E., Wehner, M. F. & Sun, L. Detection and attribution of climate extremes in the observed record. *Weather Clim. Extrem.* **11**, 17–27 (2016).
 93. Funahashi, S. Chronicle of the Causes of Famine in the World during 1840 – 2019 and their Risks. 1–13 (2019) doi:<https://doi.org/10.21203/rs.3.rs-105823/v1> License:
 94. Takeshima, A. *et al.* Global aridity changes due to differences in surface energy and water balance between 1.5 C and 2 C warming. *Environ. Res. Lett.* **15**, (2020).
 95. Betts, R. A. *et al.* Climate and land use change impacts on global terrestrial ecosystems and river flows in the HadGEM2-ES Earth system model using the representative concentration pathways. *Biogeosciences* **12**, 1317–1338 (2015).
 96. Huntington, T. G. Evidence for intensification of the global water cycle: Review and synthesis. *J. Hydrol.* **319**, 83–95 (2006).
 97. Gosling, S. N. *et al.* A comparison of changes in river runoff from multiple global and catchment-scale hydrological models under global warming scenarios of 1 °C, 2 °C and 3 °C. *Clim. Change* **141**, 577–595 (2017).
 98. Fischer, E. M., Beyerle, U. & Knutti, R. Robust spatially aggregated projections of climate extremes. *Nat. Clim. Chang.* **3**, 1033–1038 (2013).

99. Patra, R. W., Chapman, J. C., Lim, R. P., Gehrke, P. C. & Sunderam, R. M. Interactions between water temperature and contaminant toxicity to freshwater fish. *Environ. Toxicol. Chem.* **34**, 1809–1817 (2015).
100. Tsang, Y., Infante, D. M., Wang, L., Krueger, D. & Wieferich, D. Conserving stream fishes with changing climate: Assessing fish responses to changes in habitat over a large region. *Sci. Total Environ.* **755**, 142503 (2021).
101. Comte, L. & Olden, J. D. Climatic vulnerability of the world's freshwater and marine fishes. *Nat. Clim. Chang.* **7**, 718–722 (2017).
102. Kelly, S. *et al.* Warming winters threaten peripheral Arctic charr populations of Europe. *Clim. Change* 599–618 (2020) doi:10.1007/s10584-020-02887-z.
103. Sunday, J. M. The pace of biodiversity change in a warming climate. *Nature* **580**, 460–461 (2020).
104. Iglesias, I. *et al.* Linking contaminant distribution to hydrodynamic patterns in an urban estuary: The Douro estuary test case. *Sci. Total Environ.* **707**, 135792 (2020).
105. Macaulay, S. J., Buchwalter, D. B. & Matthaei, C. D. Water temperature interacts with the insecticide imidacloprid to alter acute lethal and sublethal toxicity to mayfly larvae. *New Zeal. J. Mar. Freshw. Res.* **54**, 115–130 (2020).
106. van Vliet, M. T. H. *et al.* Multi-model assessment of global hydropower and cooling water discharge potential under climate change. *Glob. Environ. Chang.* **40**, 156–170 (2016).
107. Daly, G. L. & Wania, F. Organic contaminants in mountains. *Environ. Sci. Technol.* **39**, 385–398 (2005).
108. Van Vliet, M. T. H. *et al.* Coupled daily streamflow and water temperature modelling in large river basins. *Hydrol. Earth Syst. Sci.* **16**, 4303–4321 (2012).
109. IEA. World Energy Outlook 2019. *World Energy Outlook 2019* 1
<https://www.iea.org/reports/world-energy-outlook-2019>
<https://www.iea.org/reports/world-energy-outlook-2019>
<https://webstore.iea.org/download/summary/2467?fileName=Japanese-Summary-WEO2019.pdf> (2019).

110. British Petrol. *Statistical Review of World Energy 2020 | 69th edition*.
<https://www.bp.com/content/dam/bp/business-sites/en/global/corporate/pdfs/energy-economics/statistical-review/bp-stats-review-2020-full-report.pdf> (2020).
111. Hamiche, A. M., Stambouli, A. B. & Flazi, S. A review of the water-energy nexus. *Renew. Sustain. Energy Rev.* **65**, 319–331 (2016).
112. Information, O. of E. Guidelines for Ensuring and Maximizing the Quality, Objectivity, Utility, and Integrity of Information Disseminated by the Environmental Protection Agency. **515**, 1–61 (2003).
113. Koch, H. & Vögele, S. Dynamic modelling of water demand, water availability and adaptation strategies for power plants to global change. *Ecol. Econ.* **68**, 2031–2039 (2009).
114. Raptis, C. E., Van Vliet, M. T. H. & Pfister, S. Global thermal pollution of rivers from thermoelectric power plants. *Environ. Res. Lett.* **11**, (2016).
115. Raptis, C. E., Boucher, J. M. & Pfister, S. Assessing the environmental impacts of freshwater thermal pollution from global power generation in LCA. *Sci. Total Environ.* **580**, 1014–1026 (2017).
116. Myhre, R. Water & Sustainability (Volume 3): U.S. Water Consumption for Power Production - The Next Half Century. *Epri* **3**, 57 (2002).
117. Van Vliet, M. T. H. H., Wiberg, D., Leduc, S. & Riahi, K. Power-generation system vulnerability and adaptation to changes in climate and water resources. *Nat. Clim. Chang.* **6**, 375–380 (2016).
118. Pastor, A. V., Ludwig, F., Biemans, H., Hoff, H. & Kabat, P. Accounting for environmental flow requirements in global water assessments. *Hydrol. Earth Syst. Sci.* **18**, 5041–5059 (2014).
119. Hrachowitz, M. *et al.* A decade of Predictions in Ungauged Basins (PUB)-a review. *Hydrol. Sci. J.* **58**, 1198–1255 (2013).
120. Shahzad, M. W., Burhan, M., Ang, L. & Ng, K. C. Energy-water-environment nexus underpinning future desalination sustainability. *Desalination* **413**, 52–64 (2017).
121. Manju, S. & Sagar, N. Renewable energy integrated desalination: A sustainable solution to overcome future fresh-water scarcity in India. *Renew. Sustain. Energy Rev.* **73**, 594–609

- (2017).
122. Burn, S. *et al.* Desalination techniques - A review of the opportunities for desalination in agriculture. *Desalination* **364**, 2–16 (2015).
 123. Pandelidis, D., Drag, M., Drag, P., Worek, W. & Cetin, S. Comparative analysis between traditional and M-Cycle based cooling tower. *Int. J. Heat Mass Transf.* **159**, (2020).
 124. Feron, S., Cordero, R. R., Damiani, A. & Jackson, R. B. Climate change extremes and photovoltaic power output. *Nat. Sustain.* **4**, 270–276 (2021).
 125. Pratson, L. F., Haerer, D. & Patiño-Echeverri, D. Fuel prices, emission standards, and generation costs for coal vs natural gas power plants. *Environ. Sci. Technol.* **47**, 4926–4933 (2013).
 126. Eser, P., Singh, A., Chokani, N. & Abhari, R. S. Effect of increased renewables generation on operation of thermal power plants. *Appl. Energy* **164**, 723–732 (2016).
 127. Hymel, M. The United States' Experience with Energy-Based Tax Incentives: The Evidence Supporting Tax Incentives for Renewable Energy. *Loyola Univ. Chicago Law J.* 29 (2006).
 128. Gouchoe, S., Everette, V. & Haynes, R. Case Studies on the Effectiveness of State Financial Incentives for Renewable Energy. 50–55 (2002).